JULIUS-MAXIMILIANS-UNIVERSITÄT WÜRZBURG

MASTER'S THESIS

Multiwavelength Study of One-Off Flaring Events in Blazars

Author:
Jonas SINAPIUS

A thesis submitted in fulfillment of the requirements
for the degree of Master of Science

in the

AG Kadler
Lehrstuhl für Astronomie

October 28, 2020

Declaration of Authorship

I, Jonas SINAPIUS, declare that this thesis titled, "Multiwavelength Study of One-Off Flaring Events in Blazars" and the work presented in it are my own. I confirm that:

- This work was done wholly or mainly while in candidature for a research degree at this University.

- Where any part of this thesis has previously been submitted for a degree or any other qualification at this University or any other institution, this has been clearly stated.

- Where I have consulted the published work of others, this is always clearly attributed.

- Where I have quoted from the work of others, the source is always given. With the exception of such quotations, this thesis is entirely my own work.

- I have acknowledged all main sources of help.

- Where the thesis is based on work done by myself jointly with others, I have made clear exactly what was done by others and what I have contributed myself.

Signed: *Jonas Sinapius*

Date: *München, 28.10.2020*

JULIUS-MAXIMILIANS-UNIVERSITÄT WÜRZBURG

Abstract

Fakultät für Physik und Astronomie
Lehrstuhl für Astronomie

Master of Science

Multiwavelength Study of One-Off Flaring Events in Blazars

by Jonas SINAPIUS

The *Fermi* Large Area Telescope (LAT), a space-based γ-ray observatory optimized for energies between 100 MeV and 300 GeV, has detected and observed thousands of active galactic nuclei since the advent of its mission, the majority of them blazars. Short periods of highly elevated flux in blazars, referred to as flares, are frequently detected by the telescope and subsequently reported by the instrument collaboration via an Astronomer's Telegram. In many cases, this leads to follow-up observations of the flaring source with other telescopes, for example with the Neil Gehrels *Swift* telescope. However, as thousands of blazars are known, sources that are historically active and showed multiple bright flares tend to receive more attention than their less-active counterparts. Thus, flares from sources that only flared once and remained in a low-state for most of the *Fermi* mission ("loner flares") are less likely to result in a dedicated study (Moraitis and Thompson, 2019). It is crucial to overcome this bias, as limiting research to a small subset of blazars can hinder progress on a number of fundamental questions. For instance, it is not known what triggers blazar flares, nor is it understood why some blazars flare much more frequently than others.

In this work, a sample of 23 LAT-detected blazars that have shown *exactly one* bright flare over the *Fermi*-mission is constructed. Studying the behavior of the sources during their respective flares using LAT-data and where available synchronous *Swift* X-ray Telescope (XRT) data reveals that the observed flares can show different shapes. While some sources show a clear rise-and-fall, others exhibit a more complicated flaring pattern with multiple smaller sub-flares. Yet, the amplitudes of the flares in this sample follow a narrower distribution than the flare amplitudes of all LAT blazars that have shown *at least* one period of increased flux. Investigating the composition of the sample and comparing it to all LAT-detected blazars (4LAC catalog, The Fermi-LAT collaboration, 2019) reveals a number of interesting characteristics: The sources in this sample show much lower synchrotron peaks and higher luminosities than the average of the population. This finding is consistent with the *blazar sequence* (see e.g. Ghisellini et al., 2017). Furthermore, Flat Spectrum Radio Quasars (FSRQs) are vastly over-represented in the sample, making up 16 out of the 23 total sources. These findings are numerically supported by Monte Carlo simulations, which show that a randomly selected 23-source sample is very unlikely to reproduce these characteristics. The results obtained in this study indicate that loner flares are hardly defined by the appearance of the flare itself and rather by the type of source they are most likely to arise in: Very luminous, low synchrotron peak blazars, that are primarily but not only FSRQs.

JULIUS-MAXIMILIANS-UNIVERSITÄT WÜRZBURG

Abstract

Fakultät für Physik und Astronomie
Lehrstuhl für Astronomie

Master of Science

Multiwavelength Study of One-Off Flaring Events in Blazars

by Jonas SINAPIUS

Seit Beginn seiner Mission hat das für Energien zwischen 100 MeV und 300 GeV optimierte weltraumbasierte γ-Teleskop *Fermi*-LAT tausende aktive Galaxienkerne entdeckt und beobachtet, zum Großteil Blazare. Kurzzeitige Helligkeitsanstiege in Blazaren, Flares genannt, werden häufig mit dem Teleskop detektiert und anschließend in einem Astronomer's Telegram veröffentlicht. In vielen Fällen werden daraufhin mit anderen Instrumenten, wie dem Neil Gehrels *Swift* Teleskop, Nachfolgebeobachtungen der betreffenden Quelle durchgeführt. Aufgrund der großen Anzahl an bekannten Blazaren werden jedoch historisch aktive Quellen, Quellen die mehrere helle Flares gezeigt haben, im Gegensatz zu ihren weniger aktiven Gegenstücken bevorzugt untersucht. Flares von Quellen, die nur einen einzigen, hellen Flare gezeigt haben und über den Rest der *Fermi* Mission unauffällig waren ("loner flares"), führen seltener zu dedizierten Untersuchungen (Moraitis and Thompson, 2019). Um zu verhindern, dass ein zu einseitiger Fokus auf einige wenige Blazare die Suche nach Antworten auf fundamentale Fragen behindert, ist es unerlässlich solche Voreingenommenheiten zu beseitigen. Bisher ist zum Beispiel nicht bekannt was Flares in Blazaren auslöst, ebensowenig wieso manche Blazare häufiger Flares zeigen als andere. Im Rahmen dieser Arbeit wird ein Sample von 23 LAT-detektierten Blazaren zusammengestellt, die im Laufe der *Fermi* Mission *genau einen* sehr hellen Flare gezeigt haben. Das Verhalten der Quellen wird mit LAT-Daten und, wo verfügbar, parallelen *Swift*-XRT-Daten untersucht. Dabei zeigt sich, dass die beobachteten Flares unterschiedliche Zeitverläufe aufweisen. Bei einigen Quellen sind steigende und fallende Flanke klar zu erkennen, während andere Lichtkurven komplexeres Verhalten mit mehreren sub-flares aufweisen. Dennoch sind die Flare-Amplituden im Sample über einen schmaleren Bereich verteilt, als die Amplituden aller LAT-Blazare die *mindestens eine* Phase erhöhten Flusses gezeigt haben. Die Zusammensetzung des Samples weist im Vergleich zur Grundgesamtheit der LAT-Blazare (4LAC Katalog, The Fermi-LAT collaboration, 2019) einige interessante Eigenschaften auf. Einerseits neigen die Quellen im Sample zu deutlich niedrigeren Synchrotronpeaks und größeren Leuchtkräften als der Durchschnitt, was qualitativ mit der *blazar sequence* übereinstimmt (siehe z.B. Ghisellini et al., 2017). Zum Anderen sind FSRQ Quellen mit 16 von 23 im Sample deutlich überrepräsentiert. Die Außergewöhnlichkeit dieser Eigenschaften wird durch Monte Carlo Simulationen gestützt, die zeigen, dass ein zufällig selektiertes Sample mit 23 Quellen nur mit geringer Wahrscheinlichkeit diese Eigenschaften reproduziert. In dieser Arbeit wird gezeigt, dass loner flares weniger durch den Flare selbst charakterisiert werden, als durch die Art von Quelle in der sie bevorzugt auftreten: Leuchtkräftige Blazare mit niedrigen Synchrotronpeaks, die vor allem, aber nicht ausschließlich, FSRQs sind.

Acknowledgements

I would like to thank:

Contents

List of Figures

List of Tables

List of Abbreviations

AGN	**A**ctive **G**alactic **N**ucleus
BAT	**B**urst **A**lert **T**elescope
BCU	**B**lazar **C**andidate of **U**ncertain type
BLR	**B**road **L**ine **R**egion
CCD	**C**harge-**C**oupled **D**evice
FSRQ	**F**lat **S**pectrum **R**adio **Q**uasar
GBM	**G**amma-ray **B**urst **M**onitor
LAT	**L**arge **A**rea **T**elescope
LSP/ISP/HSP	**L**ow/**I**ntermediate/**H**igh **S**ynchrotron **P**eaked object
MSL	**M**onitored **S**ources **L**ist
NLR	**N**arrow **L**ine **R**egion
QSO	**Q**uasi **S**tellar **O**bject
RDG	**R**a**d**io **G**alaxy
ROI	**R**egion **O**f **I**nterest
SED	**S**pectral **E**nergy **D**istribution
SMBH	**S**uper **M**assive **B**lack Hole
ToO	**T**arget **o**f **O**pportunity
TS	**T**est **S**tatistic
VLBI	**V**ery Long **B**aseline **I**nterferometry
XRT	**X**-**R**ay **T**elescope

Chapter 1

Introduction

Black holes are perhaps the most peculiar known objects found in the universe. With matter packed so densely that the escape velocity exceeds the speed of light, these gravitational singularities have so far been detected in two flavors. Stellar black holes form when a sufficiently massive star collapses and can have masses between a few solar masses $M_\odot$ and tens of $M_\odot$. While the origin of stellar black holes is quite well understood, the formation of their heavier counterparts, supermassive black holes (SMBH) with millions or billions of solar masses, remains elusive. Even more puzzling is their existence shortly after the Big Bang (redshift $z > 6$, around 12 Gyr light travel time, e.g. Fan (2006)).

Although black holes emit no light themselves, their gravitational influence strongly affects their surroundings which leads to observable effects. To date, a number of different phenomena have been observed that are linked to black holes. For example, in a binary system of two stellar black holes, the final merger produces gravitational waves. These signals have been observed a number of times since the first detection in 2016 (Abbott et al., 2016; Miller and Yunes, 2019). Alternatively, when a stellar black hole forms a binary system with a companion star, gas from the star can be continuously accreted onto the black hole, leading to observable X-ray radiation - X-ray binaries (see e.g. Remillard and McClintock, 2006). On the other hand, when a star wanders too close to a supermassive black hole, instead of being slowly accreted, the star can be spaghettified and rapidly shred into pieces. In these so called tidal disruption events (TDE), a small fraction of the disrupted star's matter is accreted, which leads to an intense short-term increase in optical and X-ray emission with a long-term afterglow (see e.g. Komossa, 2015). Most prominent however are SMBHs that are not only sporadically fed by stars falling into them, but have a constant supply of gas or dust so they can support a long-term high accretion state. These systems form the brightest persistent sources in the universe: active galactic nuclei (AGN).

As AGN can be observed over the whole electromagnetic spectrum and up to large redshifts due to their intense luminosities, they are very popular objects of study. A subset of AGN, blazars, make up the majority of known γ-ray sources between 100 MeV and 300 GeV. Blazars are known for their intense flux variability with short periods in highly elevated flux states, known as flares. While flares are regularly observed and studied thanks to all-sky surveys such as the *Fermi* mission, how these flares come to be remains unexplained. Tracking a blazar's flux and spectrum at different wavelengths during such a flare or investigating the fact that not all blazars flare equally frequently can potentially grant insight into this fundamental question. This work will give an overview on AGN with a focus on blazars in Chapter 2 and provide an introduction to the *Fermi*-LAT and *Swift*-XRT telescopes respectively in Chapter 3. In Chapter 4, criteria for selecting a sample of blazars that showed exactly one bright flare during the *Fermi*-mission are defined, and subsequently a sample of

23 such blazars is selected. The basic concepts of model fitting are discussed in Chapter 5, along with other computations and methods applied within this work. Chapter 6 provides detailed information about the multi-wavelength data analysis. The results of this analysis are presented in Chapter 7, together with findings on the composition of the sample and computations of the flare amplitudes. The synchrotron-peak positions and luminosities of the sample sources are compared to the 4LAC catalog (see 3.1.3), and the amplitudes of the flares are compared to amplitudes from a larger sample of flares. The limits of the methods applied in this work are assessed in Chapter 8, where the results and their implications are discussed and summarized.

Chapter 2

Active Galactic Nuclei

The centers of all but the smallest galaxies host a supermassive black hole. In galaxies with large amounts of gas and dust in the central region, this matter is pulled inwards to eventually be swallowed by the black hole. In this accretion process, large amounts of energy are radiated away at a high efficiency. About one in five galaxies show permanent accretion. Such systems are collectively referred to as active galactic nuclei (AGN), even though two given AGN can be very different in appearance.

2.1 Properties

One common property among all AGN is their luminous broadband emission, which can outshine the thermal emission produced by the stars in their host galaxy. This broadband emission covers the full electromagnetic spectrum from radio to γ-ray energies. AGN typically show bolometric luminosities between 10^{42} erg s^{-1} and 10^{49} erg s^{-1} (within this work, the *cgs* unit system is used, as is common in astronomy). Only gamma-ray bursts have a higher energy output per second, but these are only short lived transient phenomena (Deng et al., 2016).

In addition to the high luminosities which allow astronomers to study AGN even at large distances, their spectra and fluxes are subject to intense variability across the whole electromagnetic spectrum on all timescales. A fraction of AGN show relativistic outflows of matter, collimated into two jets perpendicular to the accretion disk. Depending on a jet's orientation towards the line of sight, it can appear brighter or fainter due to Doppler boosting.

2.2 Classification

AGN can be divided into different types, depending on certain criteria like morphology and spectral properties. For instance, AGN are classified as radio-loud or radio-quiet, and typically only the former show relativistic jets. The radio-loudness is defined as the ratio between the 5 GHz radio flux and the optical B-band flux according to Kellermann et al. (1989):

$$R = L_\nu(5\,\text{GHz})/L_\nu(B) \tag{2.1}$$

where an AGN is considered radio-loud if $R \geq 10$. AGN are also often classified by the width of specific optical emission lines. While narrow lines occur in all systems, an AGN is considered Type 1 if it also shows broad optical lines, and Type 2 if it lacks these broad lines. The different widths are attributed to different velocities of the line-emitting regions with higher-velocity environments leading to broader

lines. Furthermore, the narrow lines are often 'forbidden' lines, produced by state transitions that have much longer half-lives than the ones responsible for the broad lines. This indicates that the narrow lines are emitted from a lower-density region so that the improbable state transitions are not disturbed by other interactions. Additionally, different names have been coined for a number of sub-types of AGN. The most common of them are:

- Quasars (Quasi Stellar Radio Sources) or QSOs (Quasi Stellar Objects) are usually found at high redshifts and therefore it is often not possible to spatially resolve their host galaxy. Around 90% of QSOs are radio-quiet, and their radio-loud counterparts are referred to as Flat Spectrum Radio Quasars (FSRQs). Depending on the optical emission lines, QSOs can be divided into types 1 and 2.

- Radio galaxies are subdivided into Broad Line Radio Galaxies (BLRG) and Narrow Line Radio Galaxies (NLRG) and are typically found in elliptical galaxies, even though exceptions exist (Véron-Cetty and Véron, 2001). Alternatively, radio galaxies can be classified morphologically, into Fanaroff-Riley (FR) Type 1 and 2 (Fanaroff and Riley, 1974). While FR1 are core-dominated AGN and show two symmetric jets ending in plumes, FR2 are more luminous jet-lobe dominated systems with the jets ending in radio lobes.

- Seyfert galaxies (Seyfert, 1943) of types 1 and 2 are observed in spiral galaxies. They are typically radio-quiet, with the X-ray emission often exceeding its radio flux by more than 2 orders of magnitude.

- Blazars are highly variable radio-loud sources, that are among the most luminous AGN. Most notably, their jets are closely aligned to the line of sight. They are further classified in FSRQ, the most luminous type with QSO-like optical lines, and BL Lac Objects, which are distinguished by the absence of lines in the optical band. Blazars are mostly observed in the γ-band. This type of AGN is more thoroughly discussed in Sec. 2.4.

Fig. 2.1 shows a radio image of the Quasar 3C 175 taken with the Very Large Array (VLA). This source shows FR 2 morphology with only one jet fully visible and intense emission from the jet lobes.

2.3 Unification Model

To be able to describe AGN and compare them with one another, it is useful to build a simplified model to unify the sub-types. The AGN standard model (see e.g. Antonucci, 1993, Urry and Padovani, 1995) describes these systems as follows. At the center of a galaxy, a supermassive black hole with a mass between 10^7 and 10^{10} Solar masses $M_\odot$ (Vestergaard and Peterson, 2006) accretes matter via a rapidly rotating accretion disk. The process of accretion produces a thermal spectrum with a large enough energy output to explain the luminosities observed in AGN. Processes like absorption, re-emission and reflection reshape the the spectrum to its final non-thermal form. Emission and absorption lines can be used to determine a source's redshift and their widths yield information about the rotational velocity of the surrounding material. A schematic visualization of a standard-model AGN is shown in Fig. 2.2, and the individual components are more thoroughly described in the following:
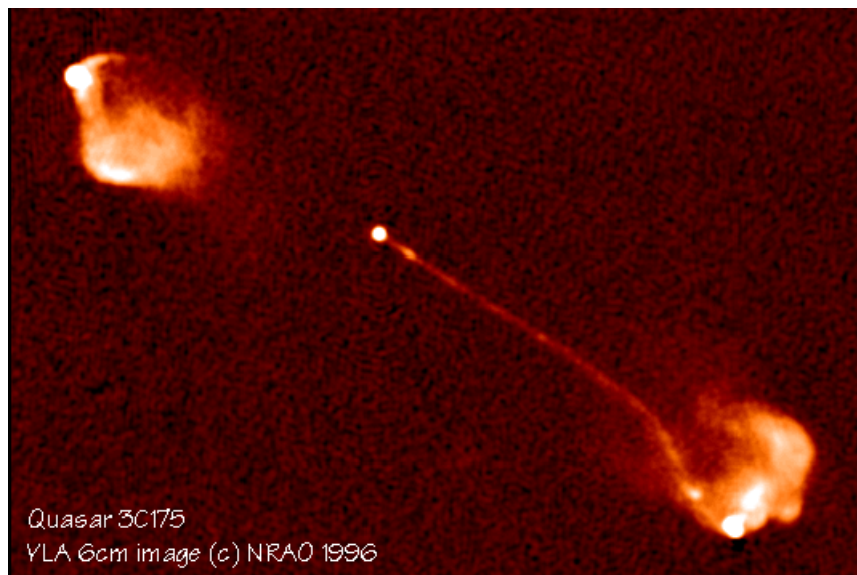
FIGURE 2.1: VLA image of Quasar 3C 175. Image courtesy of NRAO/AUI.
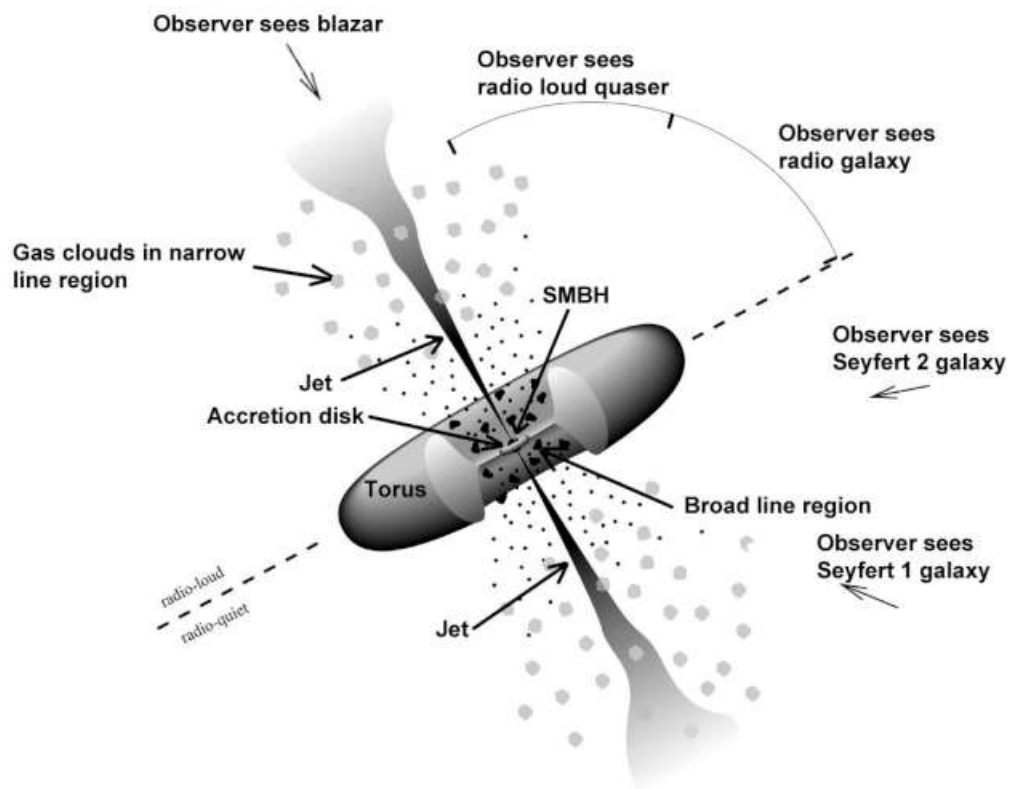
FIGURE 2.2: Unification model according to Urry and Padovani (1995). Note the divide into radio-loud and radio-quiet populations even though jets are shown on both sides of the AGN. This has been done in order to include all types in one image. Image credit https://fermi.gsfc.nasa.gov/science/eteu/agn/

- At subparsec scale around the SMBH, an accretion disk is formed from the infalling matter. Due to the high density in the disk, the material heats up and cools via thermal emission.

- A subset of AGN produces pairs of jets of highly collimated matter along the rotational axis of the disk. These jets extend up to hundreds of kiloparsec and are luminous in the radio-band.

- Close to the accretion disk, clouds of gas move in Keplerian orbits. Due to the high rotational velocities, broad emission lines are emitted from these clouds, and thus this region around the black hole, about a parsec in size, is referred to as the broad line region (BLR).

- Around the central region, a clumpy dust torus is found, with a size between 0.01 and 10 parsec.

- Farther out from the center, clouds of lower-density ionized gas rotating at smaller velocities emit narrower lines when compared to the BLR. Therefore these clouds, reaching up to thousands of parsec out from the central black hole, are called the narrow line region (NLR).

Simply by taking into account the orientation of each system with respect to the observer, this model offers an explanation for the different types of AGN observed. This model, described by Antonucci (1993), claims that the different types of AGN (see Sec. 2.2) are all the same type of object merely observed from different angles. AGN that are distinguished by the width of their emission lines (Types 1 and 2) are viewed from different angles, and in Type 2 AGN the dust torus obscures the accretion disk and the BLR with only the NLR remaining visible. At larger angles between the line of sight and the disk, the BLR comes into view, leading to a different optical spectrum. The idea that the observing angle affects the classification in types 1 and 2 was first mentioned by Rowan-Robinson (1977). While the Type 1/Type 2 classification can be explained by the viewing angle, the morphological difference between radio-loud and radio-quiet populations is intrinsic. Yet, the classification of radio-loud AGN into BLRG, NLRG and blazars can also be explained by orientation only. BLRG and NLRG can be considered as the radio-loud counterparts of Seyfert 1 and 2 galaxies, but blazars form an extreme case, where the line of sight is so closely aligned with the jet axis that strong Doppler boosting occurs for the observer.
While the Unification model offers a practical way to simultaneously explain different phenomena quite well, it is an oversimplification. The divide between radio-loud and radio-quiet populations is somewhat arbitrary, as radio-quiet systems still show some radio emission, and there is evidence of weak radio jets in these sources as well (see e.g. Falcke et al., 2000; Ulvestad and Ho, 2001; Ulvestad et al., 2005). Furthermore, a clear distinction between FSRQs and BL Lacs is often difficult and strongly depends on the intensity of the lines in comparison to the overall source brightness.

2.4 Blazars

As the goal of this thesis is to study multiwavelength properties of blazars during flaring states, this subclass of radio-loud AGN will be discussed more thoroughly here. The relativistic bulk motion of particles in the jet leads to relativistic effects. From the bulk Lorentz factor $\Gamma = (1 - \beta^2)^{-1/2}$ with $\beta = \frac{v}{c}$ and the viewing angle

θ, taking into account the relativistic transformation, the Doppler factor can be expressed as $\delta = [\Gamma (1 - \beta \cos(\Theta))]^{-1}$ (see e.g. Ghisellini, 2013). By integrating over the frequency ν, the observed flux is obtained: $F = \delta^4 F'$, where F' is the flux in the rest frame of the source. This strong dependency of the observed characteristics on the viewing angle is the main reason for the differences between blazars and radio galaxies. Notably, the Doppler factor is energy dependent, with the highest values occurring in radio- and γ bands (Zhang, Fan, and Cheng, 2002).

A blazar's spectral energy distribution (SED) typically shows two humps that are associated with different processes. The low-energy hump, which peaks between IR and X-ray frequencies, is attributed to synchrotron emission, while the high-energy hump, which peaks between X-ray and γ-ray frequencies, is usually attributed to inverse Compton processes (Donato et al., 2001). Furthermore, blazars are generally divided into FSRQs, which show strong emission lines, and the typically fainter BL Lac objects, whose optical spectra are mostly featureless. As blazars are abundant and often emit bright γ-ray emission, these objects make up the largest fraction of all sources observed by the *Fermi Gamma-ray Space Telescope* Large Area Telescope (LAT) as reported in the Fourth *Fermi*-LAT source catalog (4FGL; Abdollahi et al., 2020). Observing blazars in the radio band making use of very-long-baseline interferometry (VLBI) allows for sub-milliarcsecond resolved imaging of the emission region. This has revealed that blazar jets usually show a very luminous but unresolved core and a fainter, large-scale jet that can contain multiple regions of enhanced luminosity (jet components). For a review on the VLBI properties of blazars see e.g. Lobanov (2010). Furthermore, the γ- and radio emissions of blazars are highly correlated (see e.g. Ghirlanda et al., 2010; Ghirlanda et al., 2011; Fan and Wu, 2018), with the radio flux often lagging behind the high-energy emission by a few months (Pushkarev, Kovalev, and Lister, 2010). This correlation strongly depends on the radio wavelength, with longer wavelengths showing smaller correlations. This implies that higher frequencies are dominated by core emission while the low frequency radio emission is partially extended emission. A number of known VLBI blazars still lack a γ-counterpart (Arsioli and Chang, 2017), and this correlation can be used to approximate the contribution of blazars to the diffuse γ-ray background.

2.4.1 The blazar sequence

Another way to differentiate between blazars is by considering the position of the synchrotron peak $\nu_{\rm syn}$ in their SED. Blazars with a synchrotron peak at radio/IR frequencies are called low-synchrotron-peaked blazars (LSP). Accordingly, blazars with synchrotron peaks in the optical/soft UV band are called intermediate-synchrotron-peaked blazars (ISP) and blazars where the peak lies in the hard UV or soft X-ray range are referred to as high-synchrotron-peaked blazars (HSP). It has been found that LSP sources make up the more luminous blazar population, whereas HSP sources usually coincide with lower luminosities. This mostly phenomenological connection has been dubbed the blazar sequence (see e.g. Fossati et al., 1998; Abdo et al., 2010b). More recently, Ghisellini et al. (2017) revisited the blazar sequence, using a vastly expanded sample due to the increased sensitivity of more recent instruments such as the *Fermi*-LAT. Their findings largely coincide with the original sequence even though they correlate the γ-ray luminosity with the peak position while Fossati et al. (1998) used radio luminosities. They find that the the population of FSRQs show only small variations in $\nu_{\rm syn}$ while BL Lac objects cover a much wider range of synchrotron-peak positions. Thus, the division into LSP,
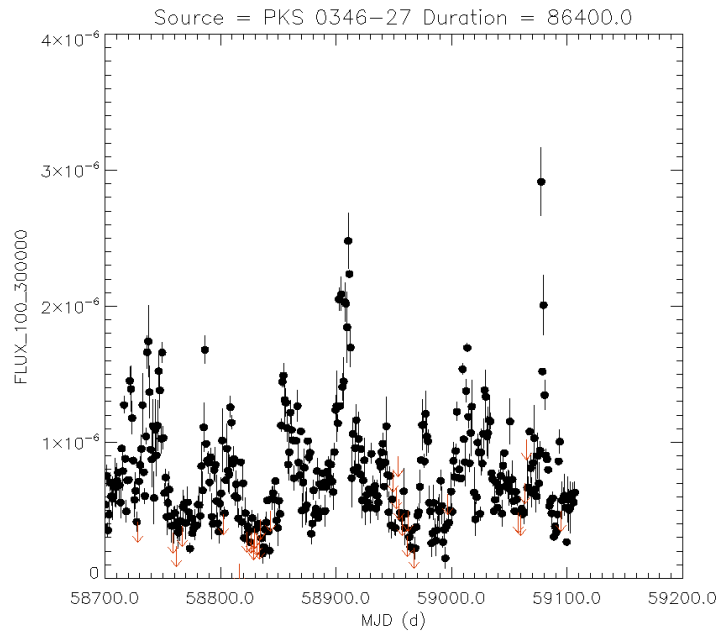
FIGURE 2.3: Exemplary blazar light curve: 1-year *Fermi*-LAT light curve of the FSRQ PKS 0346-27. The y-axis shows the flux between 100 MeV and 300 GeV in photons cm^{-2} s^{-1}. Source: *Fermi* Monitored Sources List (https://fermi.gsfc.nasa.gov/ssc/data/access/lat/msl_lc/, retrieved Sep. 16 2020).

ISP and HSP blazars is mostly employed when discussing BL Lac objects, as FSRQs would largely be classified as LSP sources.

Since the positions of both humps are connected, the high-energy emission from HSP sources often peaks in the TeV range, where Cherenkov telescopes are used to study them. LSP sources on the other hand usually have their high-energy peaks in the MeV/GeV range, allowing space-based γ-ray telescopes such as the *Fermi*-LAT to study this subset more precisely.

2.4.2 Blazar flares

Blazars are known to show intense flux variability, on time scales from seconds up to years. Short-term, intense increases in flux on the order of days up to weeks are referred to as flares. There is an ongoing discussion on how a flare is defined. Due to the stochastic nature of blazar variability(Abdo et al., 2010a), the often high duty cycles (i.e. short intervals between elevated flux states) and the lack of a consistent background level, it is difficult to clearly identify flares. However, Nalewajko (2013) offers a useful definition of a flare as "a contiguous period of time, associated with a given flux peak, during which the flux exceeds half of the peak value, and this lower limit is attained exactly twice – at the beginning and at the end of the flare."
Fig. 2.3 shows the daily binned *Fermi*-LAT light curve of the FSRQ PKS 0346-27 since August 2019. The high variability and rapid changes in flux are typical for blazars.

While blazar flares are frequently observed and among the most violent transients in the universe, the mechanisms triggering these events are not fully understood. The fact that different blazars show flares on different time scales and at different duty cycles (i.e. more, or less often) does not necessarily facilitate the search

for trigger mechanisms. Studying different sub-samples of blazars, selected depending on the characteristics of their flares, could help to understand the underlying mechanisms by finding unifying features.

Chapter 3

Instruments

3.1 The *Fermi* mission

3.1.1 Mission overview

The *Fermi* γ-ray space telescope, which, up to its launch in June 2008 was known as the *Gamma-ray Large Area Space Telescope* (GLAST), is the product of an international collaboration between space agencies from the USA, France, Germany, Italy, Japan and Sweden. The satellite carries 2 instruments: the Gamma-ray Burst Monitor (GBM) and the Large Area Telescope (LAT). The goal of the GBM is to detect gamma-ray bursts (GRBs) in real time. LAT is the main instrument on-board the spacecraft (Atwood et al., 2009). Per default, *Fermi* observes in survey mode, where the pointing constantly changes in order to observe the whole sky. Transitions to different modes can be requested manually from the ground or autonomously on-board the satellite. As only data from the LAT are considered in this work, only this instrument will be discussed in detail.

3.1.2 The LAT

The LAT's main strengths are its large field of view (> 2 sr) and the fact that it covers the full sky once every three hours during normal operations, and therefore regularly observes all known γ-ray sources. This has provided an undisturbed view of the high-energy sky for the last 12 years. Compared to its precursor mission, the Energetic Gamma Ray Experiment Telescope (EGRET) on-board the *Compton Gamma Ray Observatory* (CGRO), the LAT offers a 20-fold increase in sensitivity. Fig. 3.1 shows the source maps produced by LAT and EGRET in comparison. In fact, the 1-year source catalog produced by LAT (1FGL Abdo et al., 2010) already contains about five times the number of sources observed with EGRET (Hartman et al., 1999). Table 3.1 summarizes the Large Area Telescope's technical details.

Detection method

Due to the high energies of the γ-rays in question, telescopes designed to detect such photons cannot use reflection or refraction, but instead make use of the photon's particle character. When an electron and its antiparticle, a positron, collide, the particle pair is annihilated and other particles, typically two photons, are produced while conserving the total momentum and energy. Inversely, in the vicinity of a nucleus so that momentum can be conserved, a photon with sufficient energy ($E \geq 2 \cdot m_{e^-} = 1.022$ MeV with the electron rest mass m_{e^-}) can spontaneously decay into an e^+e^--pair. The cross section of this process increases with photon energy and atomic number (Z) of the nearby nucleus. Thus, making use of the pair conversion process is an efficient way to detect photons with energies in the MeV to GeV range.
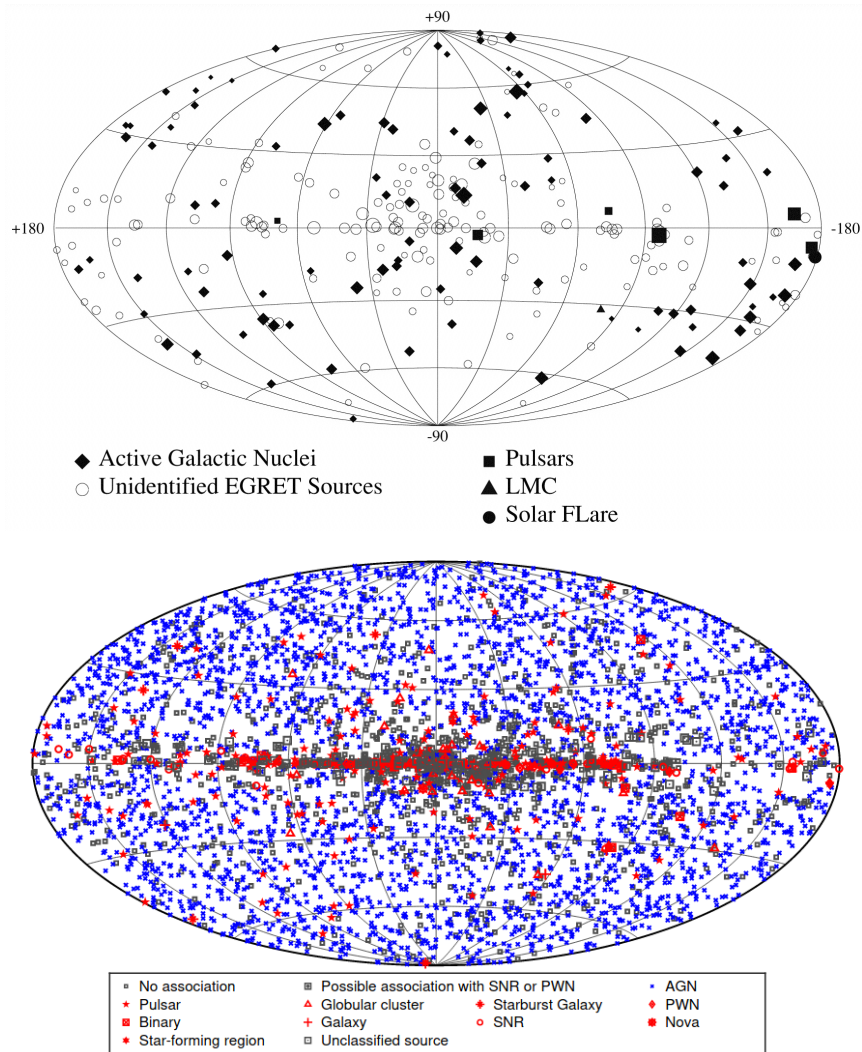
FIGURE 3.1: Top: Source map from *Fermi*'s percursor mission EGRET(Hartman et al., 1999). Bottom: *Fermi*-LAT source map from 4FGL(Abdollahi et al., 2020), excluding solar flares.

TABLE 3.1: Technical data of the *Fermi*-LAT. Table adapted from Table 1 in Atwood et al. (2009).

Property	Description
Size	$1.8 \cdot 1.8 \cdot 0.72$ m^3
Effective area	9500 cm^2 @ normal incidence
Energy range	20 MeV $-$ 300 GeV
Energy resolution (equivalent Gaussian 1σ):	
100 MeV $-$ 1 GeV:	$9\% - 15\%$
1 GeV $-$ 10 GeV:	$8\% - 9\%$
10 GeV $-$ 300 GeV:	$8.5\% - 18\%$
10 GeV ($> 60°$ incidence):	$\leq 6\%$
Single photon angular resolution	
on-axis, 68% containment radius:	
10 GeV	$\leq 0°.15$
1 GeV	$0°.6$
100 MeV	$3°.5$
on-axis, 95% containment radius	$3 \times \theta_{68\%}$
off-axis containment radius at 55%	$< 1.7\times$ on-axis value
Field of View (FoV)	2.4 sr
Timing accuracy	$< 10\ \mu$s
Event readout time (dead time)	26.5 μs
Point source localization	$< 0.5'$
Point source sensitivity, steady source, high Galactic latitude and 1 year of integration	$3 \cdot 10^{-9}$ photons cm^{-2} s^{-1}
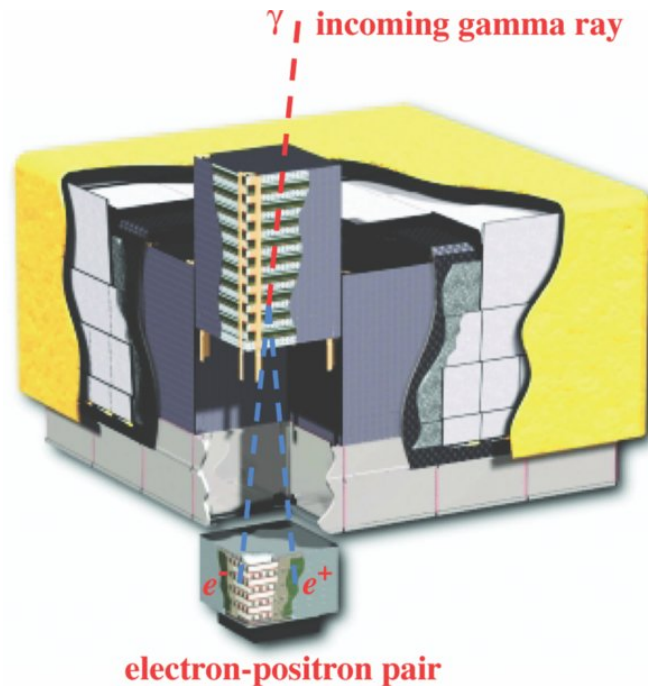
FIGURE 3.2: Diagram of the *Fermi*-LAT γ-ray detector. Image taken
from Fig. 1 in Atwood et al. (2009)

An incident γ-ray photon interacting with a high-Z material has a chance of being converted into an e^+e^--pair. By tracking the pair's path through the detector, the origin of the original photon can be reconstructed. Using on this mechanism, the LAT is able to measure photons with energies between 20 Mev and more than 300 GeV, with the point spread function rapidly increasing below 100 MeV. The LAT consists of a 4 by 4 array of converter-tracker modules. Each of these modules is made of 16 converter planes made from tungsten (Z = 74), alternating with two orthogonal layers of silicon detectors to track the (x, y) position of the pair. At the bottom of each module, two additional tracker layers are installed. Below the modules, a calorimeter measures the pair's energy to reconstruct the incident photon energy. The calorimeter consists of 96 CsI crystals, with 12 crystals forming each of the 8 layers. Each layer is oriented perpendicular to the previous one, allowing 2-D localization. Fig.3.2 shows a schematic representation of the detector structure.

Constraints and background sources

To correct for the large influx of very energetic charged particles (cosmic rays), and the background produced by their interactions with the detector material, the Anti-Coincidence Detector (ACD) surrounds the main instrument to reject such events. This is achieved using a plastic scintillator, which has a high interaction efficiency with cosmic rays. If any event is detected in both the main instrument and the ACD, it will be rejected. Furthermore, no data is taken while transiting the South Atlantic anomaly (SAA) to protect the instrument from the high-density charged particles trapped in the Earth's magnetic field. This decreases the effective observing time of both instruments on-board the *Fermi* satellite by about 15%. In addition to particle induced background, γ-ray background sources need to be taken into account as well. Residual γ-ray photons from the Earth's limb can be excluded by only considering data taken at zenith angles θ_z below a certain threshold. Furthermore, even

though the Sun's emission roughly follows a thermal spectrum peaking in the optical band, interactions of cosmic rays with the solar surface and inverse Compton scattering between cosmic electrons and solar photons in the Heliosphere lead to a detectable MeV component from the Sun. During solar flares, photons with energies in the GeV range have been detected by *Fermi*-LAT (Omodei et al., 2018). The LAT performs best for sources at high Galactic Latitudes, as the density of γ-ray sources increases with decreasing distance to Galactic disk. Many of these sources are unresolved, which leads to a much more prominent diffuse background component for observations close to or within the Galactic disk.

3.1.3 LAT-Catalogs

As the *Fermi*-LAT is an all-sky survey mission, the collaboration regularly releases updated source catalogs with increased integration times. The LAT 8 year source catalog (fourth *Fermi* Large Area Telescope source catalog (4FGL), Abdollahi et al., 2020), includes data taken during the time period August 4, 2008, to August 2, 2016. More recently, data release 2 of the 4FGL was made public (4FGL-DR2), including data up to August 2, 2018. Within LAT catalogs, sources are named in the following way: 4FGL JHHMM.m+DDMM where the 4 refers to the fourth catalog (1FGL was released after 1 year of data taking, 2FGL after 2 years, and 3FGL after 4 years) and FGL represents Fermi Gamma-ray LAT. For each of the roughly 5000 sources in 4FGL, the catalog includes for example information about possible classifications and associations, spectral type and integrated flux. The 2-month fractional variability v_2 given in the catalog offers a measure on how variable a given source should be expected to be by comparing flux fits for 2-month time intervals to the average catalog flux. As a commonly used threshold, sources with $v_2 \geq 72.44$ cannot be assumed to be constant when performing LAT analysis. Furthermore, the 4FGL contains analysis flags for sources where the data is potentially inaccurate (flagged sources), e.g. poor localization. Besides extragalactic sources such as blazars, The FGL catalogs contain a number of Galactic sources, mostly pulsar wind nebulae, supernova remnants and globular clusters. As a complement, the LAT collaboration also releases the Catalog of Active Galactic Nuclei Detected by the Fermi Large Area Telescope, most recently the fourth version (4LAC, The Fermi-LAT collaboration, 2019), which includes 8 years of data just like 4FGL. Due to the high density of sources in the vicinity of the Galactic plane, the 4LAC is subdivided into a catalog of sources at high Galactic latitude b with $|b| \geq 10°$ and low latitude sources, where the latter has larger uncertainties and comes with additional caveats. There are 344 AGN in the low-latitude catalog and 2863 sources above $10°$ latitude. 98% of all 4LAC AGN are blazars and among those, 24% are classified as FSRQs, 38% are BL Lac objects and another 38% are blazar candidates of uncertain type (BCU). In contrast to 4FGL, the 4LAC catalog also contains information on redshift z and synchrotron-peak position ν_{syn}.

3.1.4 The *Fermi* Flare Advocate

The *Fermi* Flare Advocate (also known as Gamma-ray Sky Watcher, FA-GSW) is a service provided by the *Fermi*-LAT collaboration with the goal of keeping the global astrophysical community up to date on potential new γ-ray sources, interesting transients and flares. In voluntary shifts of one week, one or two members of the collaboration inspect each day's data looking for anything out of the ordinary. This is

aided by the FA analysis pipeline, which allows the Flare Advocates to quickly perform preliminary analysis on the current day's data. The daily reports are circulated within the collaboration, and if a source is found in a flaring state, a new source is detected, or if multiple very-high-energy photons ($E \geq 1$ GeV) are observed coming from a source, the collaboration can decide to issue an Astronomer's Telegram (ATel). These short notices are published by astronomers about different kinds of detections, from AGN flares to Galactic novae to potentially hazardous asteroids and serve as a quick way to alert the community about the latest findings. This gives interested research groups and telescope operators the opportunity to point other instruments at the posted coordinates to perform follow-up observations. An example for an ATel can be found in Appendix A, published in February 2020 to alert the community that the blazar PKS 1156-221 was in its highest recorded γ-ray flux state (Sinapius and Ojha, 2020).

Fig. 3.3 shows all sources the LAT collaboration published an ATel on up to 2016. As of September 16, 2020, 517 ATels have been published by the *Fermi*-LAT collaboration[1]. A significant fraction of those has lead to follow-up observations with other instruments and publications, including Tanaka, Buson, and Kocevski (2017), connecting an extremely-high-energy (EHE) neutrino event with increased LAT-band flux from TXS 0506+056 (IceCube Collaboration et al., 2018).
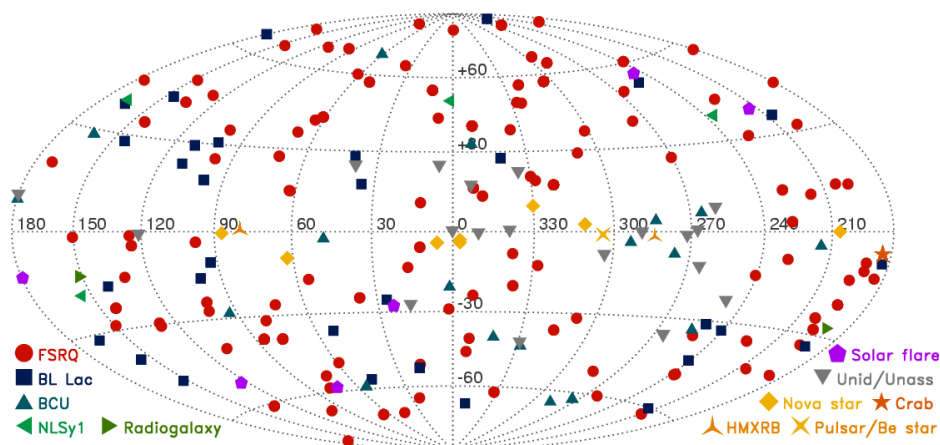
FIGURE 3.3: Map of all sources with a published LAT ATel between 2008 and 2016. Image credit http://www.asdc.asi.it/feratel/.

3.1.5 The *Fermi* Monitored Sources List

Since the beginning of the *Fermi* mission, bright sources and transients have been collected and continuously monitored within the *Fermi* Monitored Sources List (MSL) [2]. This list is a product of the Flare Advocate service and includes all sources that have at one point shown a daily LAT-band flux $F \geq 1 \times 10^{-6}$ cm^{-2} s^{-1}. For each source on the list, a public light curve is available, showing daily flux points starting from when the source first exceeded the flux threshold. Most sources on this list are blazars that were included after a flaring event. The aim of the Monitored Sources List is to allow easy access to LAT data for a number of sources and to "provide useful monitors of past and current activity for these sources" (Thompson, 2018).

---

[1] http://www-glast.stanford.edu/cgi-bin/pub_rapid
[2] https://fermi.gsfc.nasa.gov/ssc/data/access/lat/msl_lc/

However, the fluxes are computed automatically, without an absolute flux calibration and without taking into account systematic uncertainties. Thus, information and values taken from the MSL should be used cautiously.

3.2 The *Swift* mission

3.2.1 Mission overview

The *Swift* mission (Gehrels et al., 2004) was launched by NASA in November 2004, aiming to perform real-time multiwavelength observations of GRBs and their afterglows. Between GRBs, *Swift* follows a schedule of pointed observations, requested by universities and other scientific institutions. Onboard the satellite are the Burst Alert Telescope (BAT) (Barthelmy et al., 2005) to detect and localize GRBs, the X-Ray Telescope (XRT) ("The Swift X-Ray Telescope") to quickly follow up detected GRBs, and the Ultraviolet/Optical Telescope (UVOT) (Roming et al., 2005), which observes the optical afterglow and reaches sub-arcsecond localization precision. The location of a detected GRB is then transmitted to ground-based observatories within seconds to allow for multiwavelength observations of the afterglow. In this thesis only data from the XRT is used, and thus this instrument's technicalities will be discussed in more detail.

3.2.2 The XRT

A schematic diagram of the *Swift*-X-Ray Telescope is shown in Fig. 3.4.
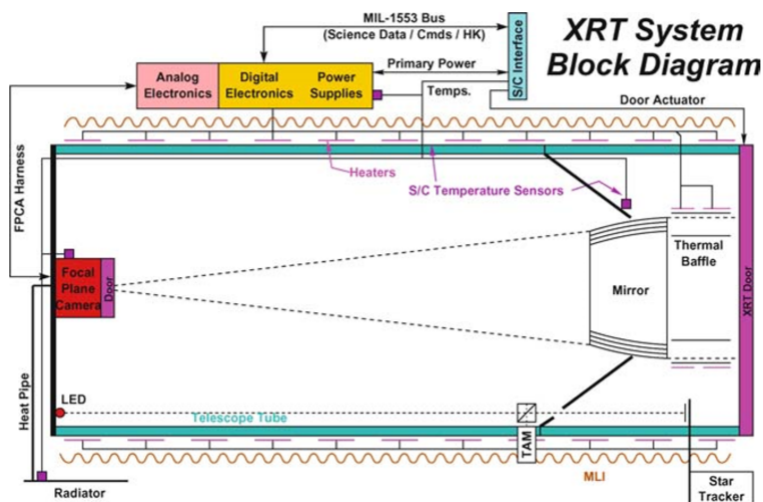
FIGURE 3.4: Diagram of the *Swift*-XRT. Image taken from "The Swift X-Ray Telescope".

Technical properties

In order to achieve precise positioning and to produce light curves with very short time resolutions, the XRT is equipped with a Wolter I X-ray telescope, that uses its 12 mirrors to focus incident X-rays onto a $2.4 \cdot 2.4$ cm^2 MOS CCD chip - the focal plane camera. This gives the telescope a $23.6 \cdot 23.6$ arcmin^2 field of view over an effective area of 110 cm^2 at 15 arcsec resolution. The XRT operates between 0.2 and

TABLE 3.2: Technical data of the *Swift*-XRT. Table adapted from Table 1 "The Swift X-Ray Telescope" and https://swift.gsfc.nasa.gov/about_swift/xrt_desc.html.

Property	Description
Telescope	JET-X Wolter I
Focal Lenght	3.5 m
Effective Area	110 cm^2 @ 1.5 keV
Detector	EEV CCD-22, 600 x 600 pixels
Detector Operation	Imaging, Timing and Photon-counting
Detection Element	40 x 40 micron pixels
Pixel Scale	2.36 arcsec/pixel
Energy Range	0.2 - 10 keV
Sensitivity	4 x 10^{-14}erg cm^{-2}s^{-1} in 10^4 seconds for known sources
	1 x 10^{-13}erg cm^{-2}s^{-1} in 10^4 seconds for blind searches

10 keV, with a 140 eV energy resolution at 6 keV. Based on the photodiode principle, incoming X-rays interact with the silicon atoms in the CCD, producing electron- and hole-currents proportional to the measured photon's energy.

Depending on the observed source's count rate, different data-taking modes are autonomously selected by the XRT. Initially, imaging mode (im) is used to detect and roughly localize sources. The rate measured in imaging mode is then used to determine which of the other modes is the optimal choice for the target source. Windowed timing mode (wt) sacrifices the second spatial dimension for millisecond time resolution and full energy resolution. Only the central 200 columns are read out, corresponding to around 8 arcmin. Photon counting mode (pc) produces 2-D images but only achieves 2.5 s time resolution. Table 3.2 summarizes the instrument's technical properties.

Constraints

Due to the sensitivity of the CCD, the telescope halts operation at angles closer than 30° to the Sun; Below 10°, a shutter (XRT Door in Fig. 3.4) is closed in order to protect the instruments. To shield the CCD from diffuse optical light, a thin filter with a one-sided aluminum coating is used. Figure 3.5 shows the energy resolution against the photon energy. For increasing energies, the resolution deteriorates. At energies below 0.5 keV, charge-trapping effects kick in, leading to a kind of upper limit for the energy resolution with a FWHM of 50 eV.

At sufficiently high count rates, CCDs show an effect called pile-up (Ballet, 1999). When two or more photons arrive at the detector in the same readout cycle, the detector will count them as a single photon with higher energy. In wt-mode, count rates > 100 counts s^{-1} should be checked for pile-up, while due to the longer integration time in pc-mode, observations with rates above 0.5 counts s^{-1} are pile-up candidates (see "The Swift X-Ray Telescope"; Romano et al., 2006).
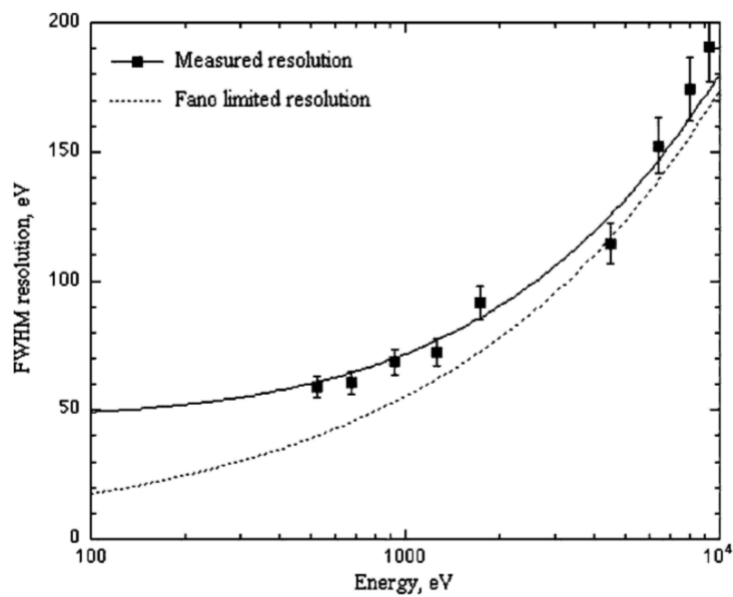
FIGURE 3.5: Energy resolution of the *Swift*-XRT CCD. Image taken from "The Swift X-Ray Telescope".

Chapter 4

The Loner-Flare Sample

Due to the large number of blazars ($\sim$ 3130, Abdollahi et al., 2020), there is a bias towards studying the most active and extreme ones more intensely. To study γ-ray outbursts with additional X-ray data, follow-up campaigns with the Neil Gehrels *Swift* telescope are common, since this observatory was built for fast follow-up observations on transients. Because such *Swift* observations have been requested for more flaring blazars than there are sources with dedicated monitoring campaigns, the bias regarding the activity of each source is less dramatic. Still, most data from the less-active blazars have never been published, or possibly even analyzed. In a previous study, Moraitis and Thompson (2019) looked for a set of criteria that influence whether a LAT-detected blazar flare followed up by *Swift* results in a refereed publication. They find that while exceptionally bright flares (peak flux $F_p > 8 \times 10^{-6}$ ph cm^{-2} s^{-1}) almost always lead to publications, generally, sources known to be very active make up 2/3 of published flares. Most notably, they find that sources with *Swift* Target of Opportunity (ToO) observations that resulted in publications had an average of 2.7 flares in the *Fermi*-LAT data, while those that were not published had an average of 1.7 flares. This shows that while multiwavelength data on sources that only showed one flare are available, typically no publications result from these.

Archival data can be used to overcome the mentioned bias by approaching the blazar population from the other side: Constructing a sample of LAT-detected blazars that only showed one bright flare. Flares in such sources have been coined "loner flares" by Wang et al. (2020), thus the sample constructed in this work will be referred to as the "loner-flare sample". LAT data, and - where available - synchronous XRT data is used to explore the temporal evolution of the SED. As the mechanism behind blazar flares isn't fully understood yet, this sample of low-duty-cycle sources offers an interesting possibility to find properties that play a role in setting off such outbursts.

4.1   Sample selection

The sample was selected from the *Fermi* Monitored Sources List (see Sec. 3.1.5) on Oct. 07 2019 to include all AGN that showed minor activity over the whole mission range, with one particularly bright flare. To include only very bright flares in this sample, only events with a peak flux of at least $2.0 \cdot 10^{-6}$ photons cm^{-2} s^{-1} in daily binning are considered. In the following, $1 \cdot 10^{-6}$ ph cm^{-2} s^{-1} will be abbreviated as 1 Flux Unit or 1 F.U.. As an additional requirement, the source must not have exceeded the 2 F.U. threshold during the rest of the mission and must not have shown fluxes above 1 F.U. more than twice. Fig. 4.1 shows the MSL light curve for GB 1310+487, an exemplary case for the sample selected in this work. In contrast,

Fig. 4.2 shows the light curve of PKS 1633+382. Even though this source meets the first selection criterion, i.e. the 2 F.U. flux threshold, there is a number of periods of high activity (high duty cycle), thus sources like this one are not included in the sample.
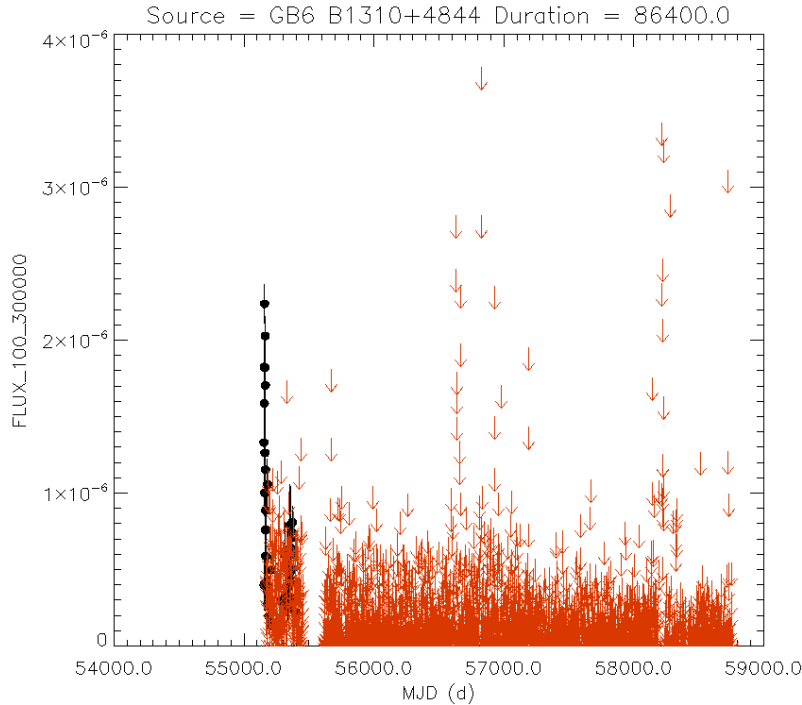
FIGURE 4.1: Monitored-sources-list daily light curve of GB 1310+487,
a typical source in the sample. The y-axis shows the flux between
100 MeV and 300 GeV in photons $cm^{-2}\,s^{-1}$.

    All monitored-sources-list light curves used for the selection of this sample can be found in in Fig. B.1 in Appendix B.
These selection criteria yield a sample of 23 sources in total. A full source list including their coordinates, the analyzed time ranges and the ATel in which the flare was reported is shown in table 4.1.

4.2 Sample properties

Among the sample of 23 4FGL sources, 16 are identified as FSRQs, 3 as BL Lac-type objects and 3 are classified as blazar candidates of uncertain type (BCU). This apparent overrepresentation of FSRQs will be further discussed in Sec. 7.1. Because the selection criteria do not require the source to be a blazar, the radio galaxy 3C 120 is also part of this sample. Due to the high LAT-band peak flux of these flares, 16 out of the 23 targets were followed up with one or multiple Target of Opportunity observations with the *Swift* satellite's on-board telescopes within the time range of the LAT light curves. Table C.1 in Appendix C lists the corresponding *Swift*-XRT observation IDs for each of these sources.
Notably, the source PKS B1150−108 is flagged in 4FGL due to its proximity to an unresolved source. Thus, data from this source should be handled with care. Furthermore, B2 1846+32B is, in spite of its significant detection in the catalog, flagged
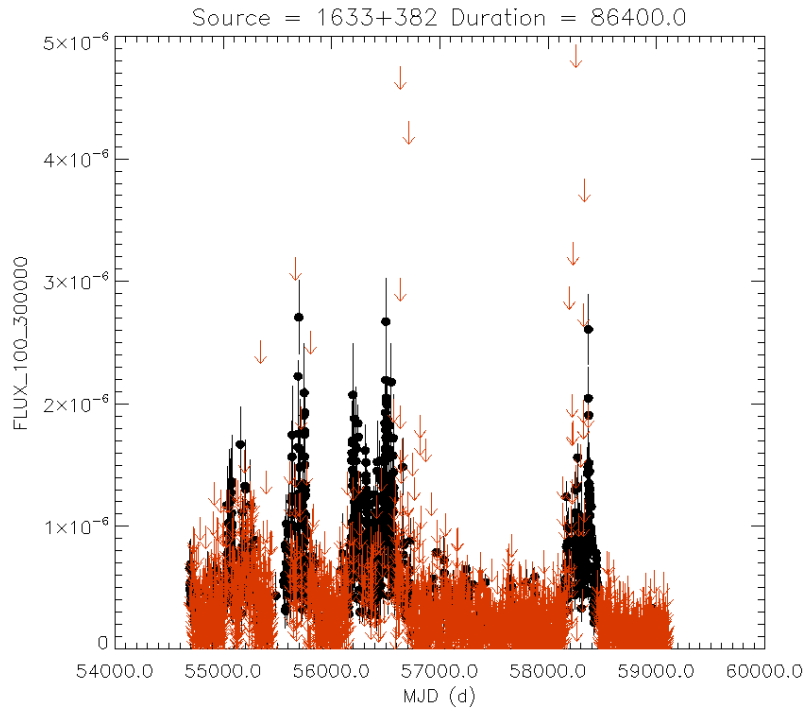
FIGURE 4.2: MSL daily light curve of PKS 1633+382. This source frequently shows high fluxes, making it too active for the loner-flare sample. The y-axis shows the flux between 100 MeV and 300 GeV in photons cm^{-2} s^{-1}.

in 4FGL because of its poor localization fit. Up to date, dedicated studies at various wavelengths have been published only on the following 13 sources from the loner-flare sample: B2 0218+357, 3C 120, PKS 0440−00, B2 0552+39A, S4 0954+65, 4C +49.22, GB 1310+487, PKS 1454−354, B2 1504+37, OT 081, B2 1846+32A, PKS 2149−306 and PKS 2233−148.

TABLE 4.1: Sample overview including coordinates, the analyzed time range and the chosen light-curve binning, as well as the corresponding ATel number.

4FGL name	Source name	RAJ2000	DEJ2000	T_{start}	T_{stop}	ATel#	Light-curve binning
4FGL J0017.5−0514	PMN J0017−0512	4.3949	-5.2347	2013-05-10	2013-06-09	5089	1 d
4FGL J0221.1+3556	B2 0218+357	35.281	35.9359	2012-08-05	2012-10-04	4343	1 d
						4371	
						4411	
4FGL J0433.0+0522	3C 120	68.2618	5.3696	2014-09-09	2014-10-08	6529	1 d
4FGL J0442.6−0017	PKS 0440−00	70.6612	-0.2961	2013-06-06	2013-07-05	5156	1 d
4FGL J0555.6+3947	B2 0552+39A	88.9015	39.7878	2017-12-21	2018-01-20	11137	1 d
4FGL J0648.4−1743	TXS 0646−176	102.111	-17.7231	2018-12-07	2019-01-07	12327	0.5 d
4FGL J0725.2+1425	4C +14.23	111.324	14.4212	2009-09-29	2009-10-28	2243	1 d
4FGL J0904.9−5734	PKS 0903−57	136.2315	-57.5833	2018-05-12	2018-05-25	11644	1 d
4FGL J0909.1+0121	PKS 0906+01	137.2967	1.3557	2010-03-24	2010-04-23	2543	1 d
4FGL J0958.7+6534	S4 0954+65	149.6897	65.5678	2014-10-31	2014-11-29	6709	1 d
4FGL J1153.3−1104	PKS B1150−108	178.3476	-11.075	2018-11-06	2018-11-17	12206	1 d
4FGL J1153.4+4931	4C +49.22	178.3505	49.5169	2011-04-09	2011-05-08	3313	1 d
4FGL J1312.6+4828	GB 1310+487	198.1694	48.4701	2009-11-03	2010-01-02	2306	1 d
4FGL J1457.4−3539	PKS 1454−354	224.3657	-35.6527	2008-08-27	2008-09-10	1701	0.25 d
4FGL J1506.1+3731	B2 1504+37	226.5347	37.5183	2014-11-17	2014-12-01	6760	0.25 d
4FGL J1751.5+0938	OT 081	267.8776	9.6456	2016-07-04	2016-08-03	9231	2 d
4FGL J1848.4+3217	B2 1846+32A	282.105	32.295	2010-10-03	2010-11-02	2954	1 d
4FGL J1848.5+3243	B2 1846+32B	282.1456	32.7309	2015-11-13	2015-11-27	8315	0.5 d
4FGL J1849.2+6705	S4 1849+67	282.3192	67.0909	2011-06-28	2011-07-12	3478	0.5 d
4FGL J2151.8−3027	PKS 2149−306	327.9655	-30.46	2012-12-27	2013-01-26	4706	1 d
4FGL J2201.5−8339	PKS 2155−83	330.3787	-83.6631	2010-01-01	2010-01-15	2373	0.5 d
4FGL J2201.8+5048	NRAO 676	330.4532	50.8053	2012-06-01	2012-07-01	4182	0.5 d
4FGL J2236.5−1433	PKS 2233−148	339.1444	-14.5557	2012-05-28	2012-06-27	4152	1 d

Chapter 5

Methods

5.1 Model fitting

To evaluate a source's spectral properties, certain assumptions are made depending on how the data is modelled. Examining how well a given model fits the experimental data requires the application of statistics. The best model is expected to have the highest probability of yielding the actual data, and thus the spectral parameters are varied until the maximum likelihood is reached.

Sources can be fit using different models. The least complicated model that is commonly used for AGN is a power law:

$$N(E) = N_0 \left(\frac{E}{E_0} \right)^{\gamma} \tag{5.1}$$

To model the characteristic double-hump structure of blazar SEDs better, log-parabola models are employed (see e.g. Massaro et al., 2009):

$$N(E) = N_0 \left(\frac{E}{E_0} \right)^{[\alpha + \beta \ln(E/E_0)]} \tag{5.2}$$

Here, N_0 refers to the normalization calculated at the pivot energy E_0, γ is the spectral index (α in the case of the log-parabola), and β the curvature parameter. When including X-ray data, one has to account for absorption in the interstellar medium. In this work, this is achieved by using the single-parameter model *tbnew_simple* provided within the ISISscripts package, which makes use of the non-relativistic photoionization cross sections for the ground states of different atoms and ions provided by Verner et al. (1996) and the element abundance provided by Wilms, Allen, and McCray (2000). The only parameter in this model is the hydrogen column density n_H.

5.2 *Fermi*-LAT likelihood analysis

This section provides an introduction to *Fermi*-LAT likelihood analysis. For a more thorough discussion, see e.g. Due to the limited angular resolution and the indirect detection via pair production, one needs to take into account photons from a larger region of the sky, the region of interest (ROI). To accomplish this, a model is fit to the whole ROI, taking into account all known point sources and diffuse background components. The ROI has to extend to a few times the PSF size, and is usually set around $10° - 15°$. The best fitting model is computed for the ROI, containing spatial and spectral information about all components. All known sources from the *Fermi*-LAT source catalogs within the ROI are taken into account, in addition to models of

Galactic- and diffuse background components provided by the instrument collaboration.

For each point source, the significance of the detection is expressed as a likelihood ratio. The resulting likelihood statistic L is the probability that the input model yields the observed data. For binned data, if the number of counts per bin is sufficiently small, the probabilities of each bin containing the observed number of counts follow the Poisson distribution. The probability of detecting n_i counts in the i-th bin is thus given as:

$$p(n_i) = \frac{m_i^{n_i}}{n_i!} e^{-m_i} \tag{5.3}$$

where m_i is the number of counts in bin i as predicted by the model. The likelihood L is defined as the product of the these probabilities:

$$L = e^{-N_{\exp}} \prod_i \frac{m_i^{n_i}}{n_i!} \tag{5.4}$$

Here, $N_{exp} = \sum_i m_i$ is the total number of counts the model predicts. Smaller numbers of counts per bin reduce the reliability of the fit, while creating fewer bins with more counts each decreases the effective resolution. In the limiting case where bins contain a maximum number of 1 count, this becomes the unbinned likelihood statistic. Now, the likelihood is:

$$L = e^{-N_{\exp}} \prod_i m_i \tag{5.5}$$

with the index i now referring to individual counts. This approach is more robust as counts are not bunched together, but for large count numbers this requires much more computational power.

The Test Statistic (TS) is defined as (Mattox et al., 1996):

$$TS = 2 \ln \frac{L_{\max,1}}{L_{\max,0}} \tag{5.6}$$

and describes the detection significance for a given source. $L_{\max,1}$ is the maximum likelihood value for a model with the source present at its location and $L_{\max,0}$ the maximum likelihood value for a model with the source not present. For larger numbers of counts, the TS distribution approaches the χ^2 distribution and one can approximate the detection significance as the square root of TS.

5.3 Bayesian blocks

Given the light curve of a source, one usually cannot immediately discern the overall noisy behaviour of source and instrument from actual increases or decreases in source activity. In order to find an objective measure for finding times of statistically constant flux, the Bayesian block algorithm by Scargle et al. (2013) can be used. In contrast to model fitting, this method is nonparametric, trying to find generic representations to divide a given set of data. The algorithm divides the data into segments (blocks), where consecutive data points are grouped into the same block if they satisfy some criterion. By using a Bayesian approach to conditional probabilities, the

optimal change-points are found by taking into account the measurement uncertainty. Assuming Gaussian errors, as is the case for *Fermi*-LAT data, the maximum value of the log-likelihood for block k becomes:

$$\log L_{\max}^{(k)} = -\frac{1}{2} \sum_n \left(\frac{x_n + \frac{b_k}{2a_k}}{\sigma_n} \right)^2 \tag{5.7}$$

Here σ_n is the Gaussian error on data point n, x_n is the measured data at point n, and $a_k = \frac{1}{2} \sum_n \frac{1}{\sigma_n^2}$ and $b_k = \sum_n \frac{x_n}{\sigma_n^2}$ are constants for a given data set.

The algorithm can be controlled by a single prior ncp_{prior}, an assumed distribution of possible block numbers which assigns smaller probabilities to larger total numbers of blocks. Alternatively, one can supply the algorithm a predefined false-positive rate p_0, the rate at which a data point is erroneously determined to be a change-point, which is then converted to the appropriate ncp_{prior}.

5.4 Luminosity calculation

In order to compare the intrinsic brightness of two sources, the luminosity can be computed by considering each source's distance. A cosmologic model has to be assumed to account for the effect of the expanding Universe which shifts the spectrum toward lower energies. In this work, the LAT luminosity L is calculated as follows, assuming a ΛCDM cosmology with $H_0 = 67.4$ km Mpc^{-1} s^{-1}, $\Omega_m = 0.315$ and $\Omega_\Lambda = 0.68$ (Planck Collaboration et al., 2020):

$$L = 4\pi d_L^2 \times F_{\text{LAT}}^{\text{4LAC}} \times \left(\frac{1}{1+z} \right)^{2-\Gamma} \tag{5.8}$$

Here, d_L is the luminosity distance, $F_{\text{LAT}}^{\text{4LAC}}$ is the catalogued energy flux between 100 MeV and 100 GeV from 4LAC, z is the redshift and Γ is the LAT spectral index from 4LAC, assuming a power-law. LAT spectra of blazars are often better described with log-parabolas, but this approximation is a decent estimate to compare the sources with each other.

5.5 Statistical methods

The Kolmogorov-Smirnov-test (KS-test) can be used to test whether a given sample follows a certain probability distribution, or whether two samples are likely to have been drawn from the same parent population (two-sample KS-test). This is expressed via the so-called D-statistic. In the case of the two-sample KS-test (applied in this work), the D-statistic measures the absolute distance between the two samples. D closer to zero means it is more likely both samples are drawn from the same distribution. The D-value can be converted to a p-value, similar to the classical significance p at which the null-hypothesis (both samples stem from the same distribution) can be discarded. However, when sample sizes are small, the statistical power of the KS-test is limited. As a brute-force alternative to the two-sample KS test, instead of statistically comparing the compatibility of two distributions, one can artificially generate a large number of samples from a parent distribution to see whether the generated samples are similar to the actual data samples. In this work, Monte Carlo simulations are used to create a large number of samples with 23 individual sources each from a source catalog, and then the fraction of samples sharing

some predefined property with the original sample (e.g. at least n sources with a distance larger than x) is computed. This permits to investigate whether that predefined property is unique to the original sample or likely to arise haphazardly.

Chapter 6

Multi-wavelength data reduction and analysis

Initially, for each source a 1-month time-window around the highest γ-ray flux reported in an ATel was selected. In order to find the optimal time range for each source, a preliminary 1-month light curve was produced to see whether a longer time range was needed or a shorter span would be sufficient. The resulting optimal time ranges are centered at the time of the highest measured flux and range between 11 days and 2 months. For each source, the adjusted LAT time range and the ATel are listed in table 4.1.

In two cases, it was not possible to center the time range on the flare date. The sources PKS 0903−57 and PKS B1150−108 were in such low states before the onset of their respective flare that no flux could be calculated for time bins more than two days before the reported flare. Thus, in these cases the time range is not centered on the flare date but instead begins with the first time bin the source is significantly detected in.

6.1 *Fermi*-LAT gamma-ray data

For each source in the loner-flare sample, γ-rays with energies between 100 MeV and 300 GeV from a $15°$ region of interest centered around the source position are considered. Fig. 6.1 shows an example of a ROI to illustrate the high density of 4FGL sources. At the center is the source PKS B1150−108 (4FGL J1153.3−1104). As mentioned in Sec. 4.2, this source is flagged in 4FGL because of a nearby unresolved source. This is apparent in Fig. 6.1, where the source 4FGL J1155.2−1111 and PKS B1150−108 almost overlap.

A binned likelihood analysis is performed using the software package Fermi-Tools version 1.2.1[1] with *fermipy* 0.18.0[2] (Wood et al., 2017). This offers a convenient environment to write individual analysis scripts. To exclude data flagged as potentially inaccurate, the standard filter criterion was adopted[3]. In addition, data taken at a zenith angle $\theta_z \geq 90°$ were discarded in order to avoid contamination originating from the Earth limb. To mitigate the sun's influence, all data where the source had a distance of less than $15°$ to the sun's position were ignored as well. The instrument response function is continuously updated, and the latest version $P8R3\_SOURCE\_V2$ is used in this work. The most recent model files for the Galactic diffuse background ($gll\_iem\_v07.fits$) and for the isotropic diffuse background ($iso\_P8R3\_SOURCE\_V2\_v1.txt$) are employed.

---

[1] https://github.com/fermi-lat
[2] https://github.com/fermiPy/fermiPy
[3] $(DATA\_QUAL > 0)\&\&(LAT\_CONFIG == 1)$
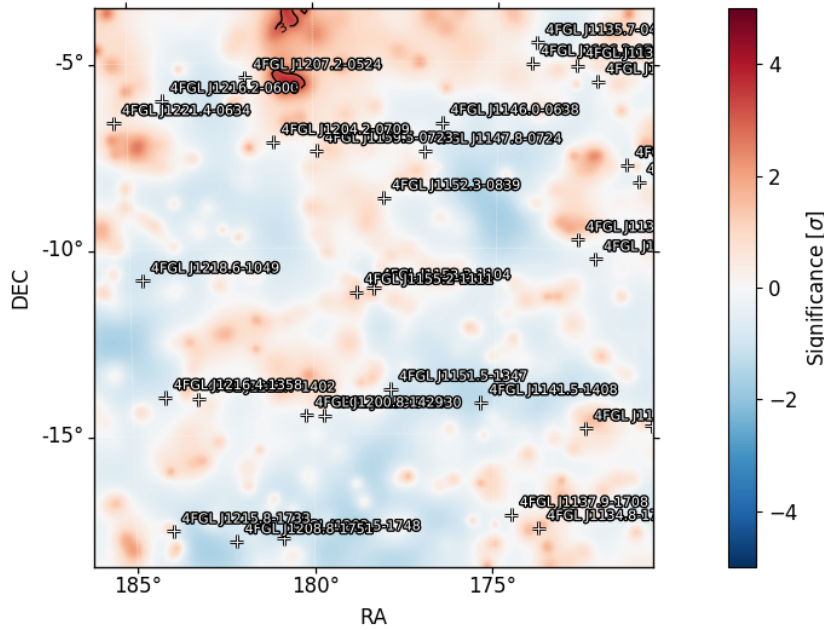
FIGURE 6.1: LAT residual map for the ROI of PKS B1150−108
(4FGL J1153.3−1104). Each white cross corresponds to a 4FGL source.
Note the source 4FGL J1155.2−1111 almost on top of PKS B1150−108.

The ROI is divided into spatial bins with $0.1°$ pixel^{-1}. Eight energy bins are created for each decade in the 100 MeV to 300 GeV range. In order to account for energy dispersion at the edges of the energy range, two extra bins are considered at each end of the spectrum by setting the *edisp_bins* option to -2. Furthermore, for sources at Galactic latitudes $|b| \leq 30°$, to account for the increased uncertainty closer to the Galactic disk, a weighted-likelihood approach is used. Using the *gteffbkg* and *gtwtsmap* tools [4], a weights map is created. The *gteffbkg* tool estimates the effective background count rate for each pixel. From these rates, likelihood weights are calculated, mimicking systematic uncertainties in the background modelling for each position and at different energies with *gtwtsmap*. The calculated weight for each pixel is then applied for all further likelihood calculations so that pixels with larger uncertainties are given less weight.

Other sources in the ROI are not necessarily stable during the studied time ranges. Thus, for sources close to the target ($\leq 5°$) and sources that are known to be variable (variability index $v_2 \geq 72.44$, see Sec. 3.1.3), the normalization in the source model is left as a free parameter. Furthermore, the model parameters for the Galactic- and isotropic diffuse emission are free to vary.
To make sure no sources that should have been modelled have been missed, an iterative search for new sources in the ROI is implemented. For each position in the ROI at least $0.5°$ from other sources, the likelihood is computed that a model including an additional point source at that position describes the data better than the current model. If an additional point source is found at TS≥ 25, it is added to the full model and accounted for in subsequent computations.

---

[4]https://fermi.gsfc.nasa.gov/ssc/data/analysis/scitools/weighted_like.pdf
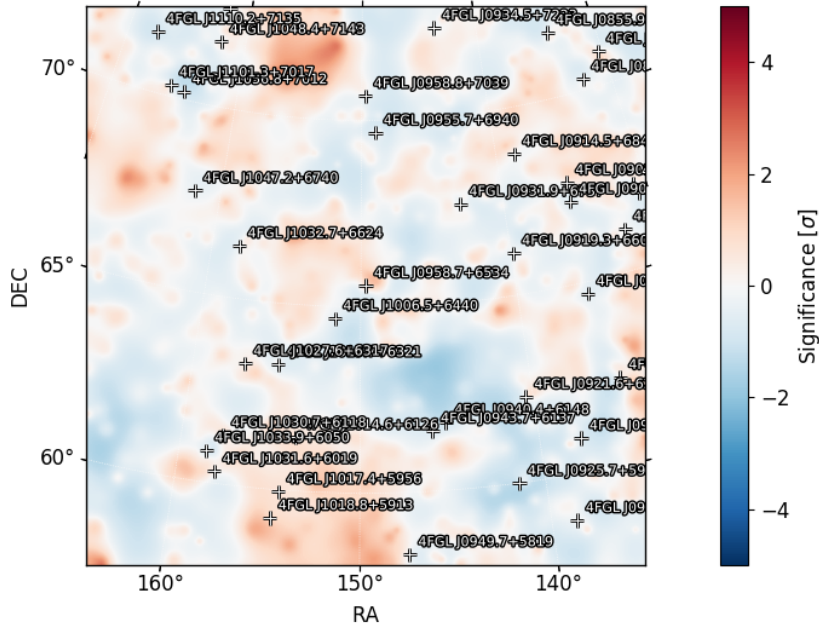
FIGURE 6.2: LAT residual map for the ROI of S4 0954+65 (4FGL J0958.7+6534). Each white cross corresponds to a 4FGL source. The color scale shows the significance at which an additional point source at any given position is compatible with the data.

An example of a modelled ROI is shown in Fig. 6.2, showing a LAT residual map for the ROI of S4 0954+65. For each position, the significance is given at which an additional point source at those coordinates is compatible with the data. The significance does not exceed $2\,\sigma$ for any given position, indicating that the chosen model describes the ROI sufficiently well and no prominent sources have been overlooked. As a contrast, Fig. 6.3 shows the same ROI but without including the target itself in the model. At the position of S4 0954+65, excess emission at more than $13\,\sigma$ significance is observed.

Light curves are created with time bins between 6 h and 2 d. The bin size is chosen individually for each source in order to best describe the flare and to obtain a useful time resolution, while keeping the number of statistically significant time bins high. While fitting the light curve, only the isotropic diffuse background and sources with $v_2 \geq 72.44$ that are detected at $TS \geq 16$ are freed, as well as the target itself. All other sources are fixed at the respective parameters obtained in the ROI fit. When creating a light curve, for each time bin the ROI is fit and a corresponding TS value is calculated. For bins where the target was in a low state, only a small number of photons can be detected, leading to a decreased TS value. To test whether the light curve fit is a good representation of reality, one can plot the flux in each time bin divided by its error ($F/(\Delta F)$) against the number of predicted counts in that bin divided by its square root ($n_{\mathrm{pred}}/\sqrt{n_{\mathrm{pred}}}$). If the model accurately describes the source, this distribution should approximately form a bisecting line. Fig. 6.4 shows one example of this sanity check for the source GB 1310+487, and the expected linear behavior is clearly visible.
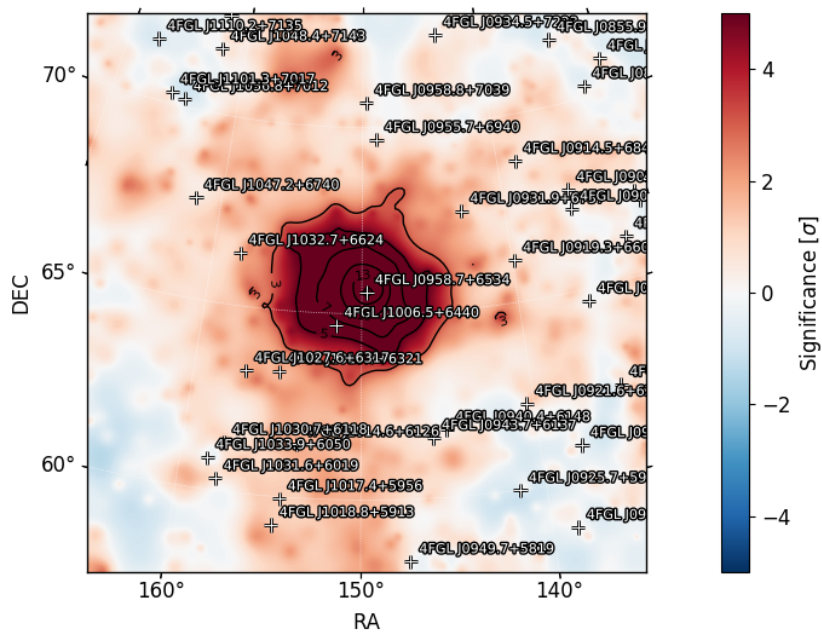
FIGURE 6.3: LAT residual map for the ROI of S4 0954+65 (4FGL J0958.7+6534) with the target not accounted for in the model. The intense excess at the source position shows the high emission state the source was in.
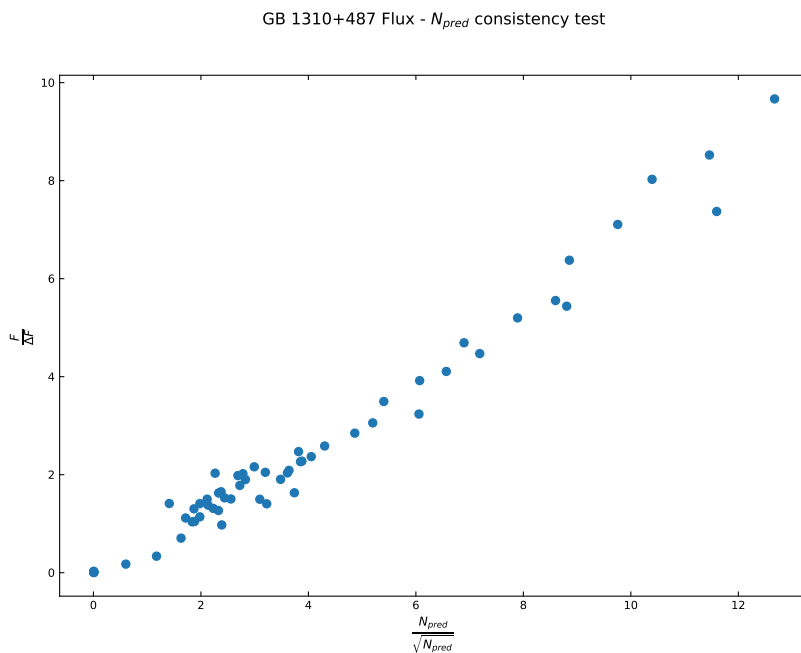
FIGURE 6.4: Sanity check for the light curve of GB 1310+487: $\frac{F}{\Delta F}$ should be directly correlated with $\frac{n_{\text{pred}}}{\sqrt{n_{\text{pred}}}}$, as is the case here.

A Bayesian Blocks algorithm (see Sec. 5.3) is then applied to each light curve in order to identify periods of statistically constant flux. The prior parameter p_0, which controls the rate for a false positive identification of an individual block, is set to 0.05. Using the *fermipy* SED tool, for each block a LAT spectral energy distribution is produced to study the spectral evolution during the flare. As some blocks are very short in duration and/or very faint, oftentimes the default energy binning leads to a large number of upper limits or poorly constrained energy bins. In order to increase the statistical significance of each bin, an algorithm was developed to adapt the binning in the following way: At first, the SED is fit with the original binning. Starting at $n = 1$, if the n th energy bin has a TS smaller than the threshold of 1, it is combined with the $n + 1$ st bin and the SED is refit with the new binning. This is repeated until the resulting bin reaches the TS threshold before the algorithm moves on to the next existing bin and starts over again. While this introduces a potential bias towards lower-energy data points, these low-energy LAT data points are crucial important for connecting LAT- and XRT-spectra reasonably.

6.2 *Swift*-XRT data

All *Swift*-XRT observations of the sample sources that were taken during the time range of the LAT light curve are taken into account. The XRT data extraction and processing was performed using standard procedures (xrtpipeline v0.13.5[5]). This creates cleaned event files by identifying bad pixels and performs event reconstruction. All XRT observations analysed in this research were taken in photon counting (PC) mode due to the low count rates (< 0.5 counts/s) throughout the complete sample. Events with grades 0-12 are used[6]. The grading allows to find and exclude events where multiple neighboring pixels recorded a higher-than-background rate which leads to a less reliable energy measurement. To account for point spread function corrections, ancillary response files are created for each data set, using the tool *xrtmkarf*[7].
Source photons were extracted from a circular 22 arcsec region around the target coordinates. As the spectrum extracted from the source region contains background counts as well, the background is modelled from an annular region around the source region with an outer radius of 60 arcsec. Fig. 6.5 shows an XRT counts map with source region and background region shown as circles and the source S4 0954+65 clearly visible.

A number of XRT data sets had exposures < 1 ks, with the resulting count rates approaching 0. An example of such a data set is provided in Fig. 6.6, showing a counts map and the extraction regions for observation 00010984004 of PKS B1150$-$108. In contrast to Fig. 6.5, the source was not detected during this observation due to the short exposure of ~ 17 s. Data sets like this one are excluded from the analysis.

Photons with energies between 0.5 and 10.0 keV are considered and the data are binned so that each energy bin contains at least 20 counts in order to justify the assumption that the photons follow a Poisson distribution.

---

[5] https://heasarc.gsfc.nasa.gov/ftools/caldb/help/xrtpipeline.html

[6] See https://www.swift.ac.uk/analysis/files/xrt_swguide_v1_2.pdf figure 2.2 for clarification.

[7] See https://heasarc.gsfc.nasa.gov/ftools/caldb/help/xrtmkarf.html for details.

FIGURE 6.5: XRT counts map for observation 00033530001 of S4 0954+65. The inner green circle contains the source region (22 arcsec radius) and the annulus between inner- and outer circle marks the background region (60 arcsec outer radius).

FIGURE 6.6: XRT counts map for observation 00010984004 of PKS B1150−108. The inner green circle contains the source region (22 arcsec radius) and the annulus between inner- and outer circle marks the background region (60 arcsec outer radius). However, due to the very short exposure in this observation, the target is not detected.

FIGURE 6.7: XRT counts light curve for OT 081. Vertical black lines indicate the edges of the Bayesian blocks. In block 4, four XRT observations were taken and the count rate in the first one is not compatible with the rates in the last two observations in this block.

6.3 Joint LAT & XRT analysis

The subsequent analysis is performed using the **I**nteractive **S**pectral **I**nterpretation **S**ystem for High Resolution X-Ray Spectroscopy (ISIS Houck and Denicola, 2000). The corresponding XRT observation IDs (ObsIDs) are given in Table C.1 in Appendix C.

For each block of statistically constant flux (see Sec. 6.1), XRT and LAT data are fit together. As some blocks contain more than one XRT observation, one needs to ensure that the source was in a similar state during these observations before combining them. This can be accomplished by comparing the count rates of the individual observations. For all blocks, the rates agree with one another within their uncertainties with the exception of one block in OT 081. This is shown in Fig. 6.7, where the XRT count rate light curve (averaged for each individual observation) for OT 081 is plotted, with the Bayesian block limits drawn in black. The error bounds of the first observation in block 4 do not overlap with the error bounds of the last two observations in the same block, however even in this case the absolute count-rate difference is small. Thus, the XRT data sets in each block are stacked to achieve better photon statistics.

For each block that contains at least one XRT observation, the spectrum is fit with a logarithmic parabola, accounting for absorption due to neutral hydrogen with *tbnew_simple* (see Sec. 5.1). The minimal value for the column density n_H is set to its Galactic value n_{H0} (Kalberla et al., 2005) for each source, respectively. The free parameters in this fit are the normalization, the spectral slope α, the curvature β, and n_H, which can vary between n_{H0} and $2 \times n_{H0}$. The pivot energy E_p is fixed at 1000 keV.

In blocks where no XRT data was available, an unabsorbed log-parabola is fit to the LAT data. In some cases, the number of LAT upper limits in the light curve is greater than or equal to the number of non-upper-limit points. In order to still allow for a reasonable fit, in these cases the spectral index α is fixed to its respective catalog value obtained from 4FGL. For data sets where fixing α is not sufficient to obtain a good fit, β was fixed to its catalog value as well. While a fit with fixed α and β parameters yields no information about the spectral shape at the time of the observation, the emission state can still be deduced as the normalization is a free parameter. This way, under the assumption that the spectrum does not significantly shift/harden/soften with respect to its average state, one can extract an energy flux value even with poor data coverage.

Chapter 7

Results

7.1 Sample properties

A sample of 23 LAT-detected sources was selected, where each source exhibited exactly one bright flare during the lifetime of the *Fermi*-mission. In the following, different properties of these loner-flare blazars are studied and then used to compare this sample to a larger population of blazar sources. Table 7.1 summarizes a number of key parameters from the sources in the loner-flare sample. There, source type, redshift and the synchrotron-peak position ν_p are shown as given in 4LAC (see Sec. 3.1.3). Furthermore, the mean luminosities over the last 8 years between 100 MeV and 100 GeV are computed from the 4LAC energy flux (see Sec. 5.4).

In order to learn about the sample source's distribution in coordinate space and redshift space, the 23 sources are compared to the 4LAC catalog. 4LAC is subdivided into a catalog of sources at high Galactic latitudes and low-latitude sources; four sources from the original sample are part of the low-latitude catalog. Thus, for better comparability, low- and high latitude catalogs are used together.

Out of the 2863 sources reported in 4LAC, 1421 have redshift information. All 23 sample sources are associated with a redshift in 4LAC. Figure 7.1 shows the redshift distribution of 4LAC and the original sample in a histogram. Initially, there appears to be an overrepresentation of high-redshift sources ($z \geq 2$) in the sample. Using Monte Carlo simulation with the 4LAC as a parent population yields that out of 10,000 samples with 23 sources each, 30.38 % have at least 2 sources with $z \geq 2$. Thus, the loner-flare sample's redshift distribution does not tend towards higher z value. In the same manner, the large number of FSRQs in the sample is investigated by computing the probability of selecting 16 FSRQs when randomly sampling 23 sources from 4LAC. Out of 100,000 samples with 23 random 4LAC sources, 1.367 percent contain at least 16 FSRQs sources. Thus, the large portion of FSRQs in the sample has a small probability of less than 2 % of being coincidental.

Similarly, the 4LAC catalog is used to compare the distribution of synchrotron peaks ν_{syn} and luminosities L in the original sample with the parent-population distribution. The synchrotron-peak distributions are shown in Fig. 7.2 and the luminosity distributions in Fig. 7.3. From Fig. 7.2, it is apparent that the sample is comprised of sources from the low end of that distribution, where generally more FSRQs are found. The sample's high fraction of FSRQs is qualitatively consistent with that assessment, but this can be further substantiated. 100,000 samples with 23 sources each are drawn from all 4LAC sources where both redshift- and ν_{syn} information is available ($\gtrsim 1400$ sources). This is repeated for different pre-defined sample selection criteria, and each time the fraction of samples containing only sources with $\nu_{\mathrm{syn}} < 10^{14}$ Hz is computed. The results are summarized in Table 7.2. These simulations show that a given sample of the same size is very unlikely to only contain

TABLE 7.1: Sample overview

4FGL name	Source name	Type	z	L [erg s^{-1}]	ν_{syn} [Hz]	A_{rel} [$\cdot 10^{-6}$ ph cm^{-2} s^{-1}]	A_{abs}
4FGL J0017.5−0514	PMN J0017−0512	FSRQ	0.227	$2.25\cdot10^{45}$	$8.49\cdot10^{12}$	85.4	2.28
4FGL J0221.1+3556	B2 0218+357	FSRQ	0.944	$5.09\cdot10^{47}$	$7.03\cdot10^{12}$	30.9	4.13
4FGL J0433.0+0522	3C 120	RDG	0.033	$3.64\cdot10^{43}$	$3.98\cdot10^{13}$	83.1	2.46
4FGL J0442.6−0017	PKS 0440−00	FSRQ	0.449	$4.51\cdot10^{46}$	$1.96\cdot10^{12}$	32.2	2.99
4FGL J0555.6+3947	B2 0552+39A	FSRQ	2.365	$1.81\cdot10^{48}$	$3.43\cdot10^{11}$	57.2	1.95
4FGL J0648.4−1743	TXS 0646−176	FSRQ	1.232	$2.39\cdot10^{47}$	$3.89\cdot10^{12}$	85.8	3.39
4FGL J0725.2+1425	4C +14.23	FSRQ	1.038	$3.58\cdot10^{47}$	$9.12\cdot10^{12}$	29.7	2.19
4FGL J0904.9−5734	PKS 0903−57	BCU	0.695	$1.00\cdot10^{47}$	$1.91\cdot10^{13}$	43.2	2.57
4FGL J0909.1+0121	PKS 0906+01	FSRQ	1.024	$2.65\cdot10^{47}$	$3.63\cdot10^{12}$	33.7	2.13
4FGL J0958.7+6534	S4 0954+65	BLL	0.367	$1.89\cdot10^{46}$	$1.17\cdot10^{13}$	38.3	1.86
4FGL J1153.3−1104	PKS B1150−108	BCU	0.269	$5.18\cdot10^{44}$	$6.18\cdot10^{12}$	$1.41\cdot10^{3}$	2.27
4FGL J1153.3−1104	4C +49.22	FSRQ	0.334	$8.18\cdot10^{45}$	$1.51\cdot10^{13}$	74.4	2.4
4FGL J1312.6+4828	GB 1310+487	BCU	0.501	$2.96\cdot10^{46}$	$8.55\cdot10^{12}$	66.6	2.21
4FGL J1457.4−3539	PKS 1454−354	FSRQ	1.424	$6.63\cdot10^{47}$	$1.01\cdot10^{13}$	42.9	2.49
4FGL J1506.1+3731	B2 1504+37	FSRQ	0.673	$7.56\cdot10^{46}$	$3.85\cdot10^{12}$	31.6	1.88
4FGL J1751.5+0938	OT 081	BLL	0.322	$1.79\cdot10^{46}$	$7.94\cdot10^{12}$	73.4	4.48
4FGL J1848.4+3217	B2 1846+32A	FSRQ	0.798	$9.00\cdot10^{46}$	$1.54\cdot10^{13}$	74.3	2.07
4FGL J1848.5+3243	B2 1846+32B	FSRQ	0.981	$2.10\cdot10^{47}$	$6.76\cdot10^{12}$	42.5	2.48
4FGL J1849.2+6705	S4 1849+67	FSRQ	0.657	$1.15\cdot10^{47}$	$1.39\cdot10^{13}$	29.5	2.21
4FGL J2151.8−3027	PKS 2149−306	FSRQ	2.345	$4.29\cdot10^{48}$	$1.70\cdot10^{12}$	31.8	2.87
4FGL J2201.5−8339	PKS 2155−83	FSRQ	1.865	$1.01\cdot10^{48}$	$7.94\cdot10^{12}$	44.5	2.25
4FGL J2201.8+5048	NRAO 676	FSRQ	1.899	$3.18\cdot10^{48}$	$2.83\cdot10^{12}$	34.9	4.55
4FGL J2236.5−1433	PKS 2233−148	BLL	0.325	$2.49\cdot10^{46}$	$1.13\cdot10^{13}$	39.6	3.06

Selected properties of the sample sources, including the redshift, their synchrotron peak and their luminosity obtained from 4LAC (The Fermi-LAT collaboration, 2019). Additionally, flare amplitudes are included in this table, calculated by dividing (A_{rel}) and subtracting(A_{abs}) the *Fermi* MSL daily peak flux by the 4FGL flux respectively.
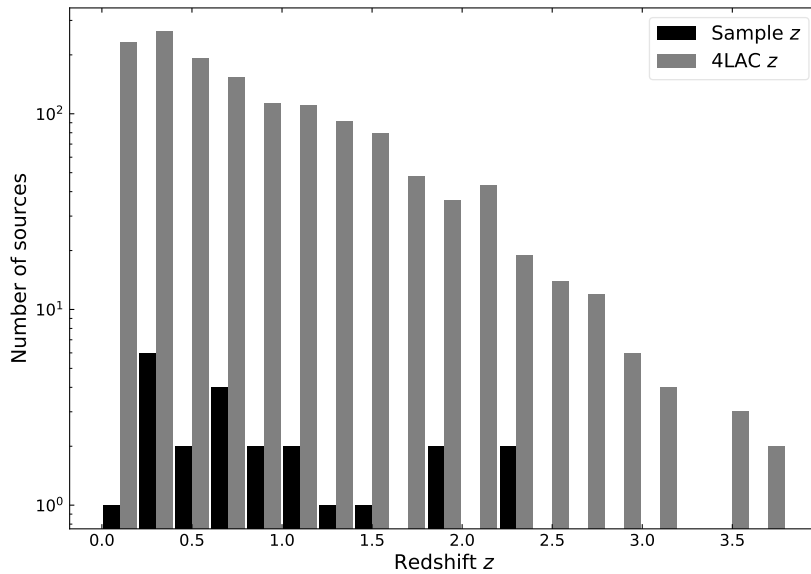
FIGURE 7.1: Redshift distribution of the loner-flare sample compared to all 4LAC sources with redshift information. The y-axis has a log-scale.
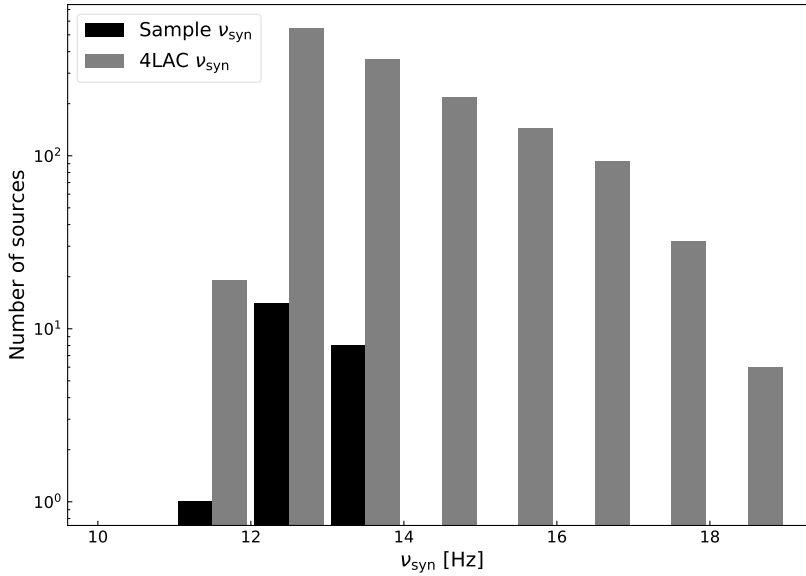
FIGURE 7.2: Synchrotron-peak distribution of the loner-flare sample compared to all 4LAC sources with ν_{syn} and redshift information.

sources with $\nu_{\text{syn}} < 10^{14}$ Hz - no approach yielded a fraction of samples consistent with the original larger than 1 %.

First, 23 sources are drawn without further constraining the selection. Here, out of 100,000 samples, 0.01 % consist of only sources with $\nu_{\text{syn}} < 10^{14}$ Hz. Then, the original sample's distribution of high- and low-latitude sources is recreated, drawing 100,000 samples consisting of 4 low latitude- and 19 high-latitude sources. 0.005 % fulfill the requirement. In the next step, different sample compositions depending on source type are tested, disregarding the Galactic latitude. First, the composition of the original sample (16 FSRQs, 3 BL Lac, 1 RDG, 3 BCU) is used. This increases the fraction of samples similar to the original to 0.286 %. As the vast majority of sources in the original sample are FSRQs, it is not unreasonable to assume that the remaining BCU might also be FSRQ. Thus, 100,000 samples with 3 BL Lac, 19 FSRQs and 1 RDG are created and yield that 0.94 % of those show only synchrotron peak positions below 10^{14} Hz.

The luminosity distribution depicted in Fig. 7.3 shows the inverse trend: The original sample contains mostly sources from the high end of the 4LAC luminosities. The same Monte Carlo method used for the synchrotron peaks is applied, simulating 4 times 100,000 samples and comparing their luminosity distribution to the original sample's. The results are also shown in Table 7.2. This time, the probability for at least 19 sources showing a luminosity $L \geq 10^{46}$ erg s^{-1} is tested. Depending on the sample composition, the following fractions of generated samples meet this requirement.

- Without additional conditions 0.2 % of the samples have at least 19 sources with $L \geq 10^{46}$ erg s^{-1}.

- Selecting 4 low-Galactic-latitude sources and 19 high-Galactic-latitude sources yields 0.344 %.
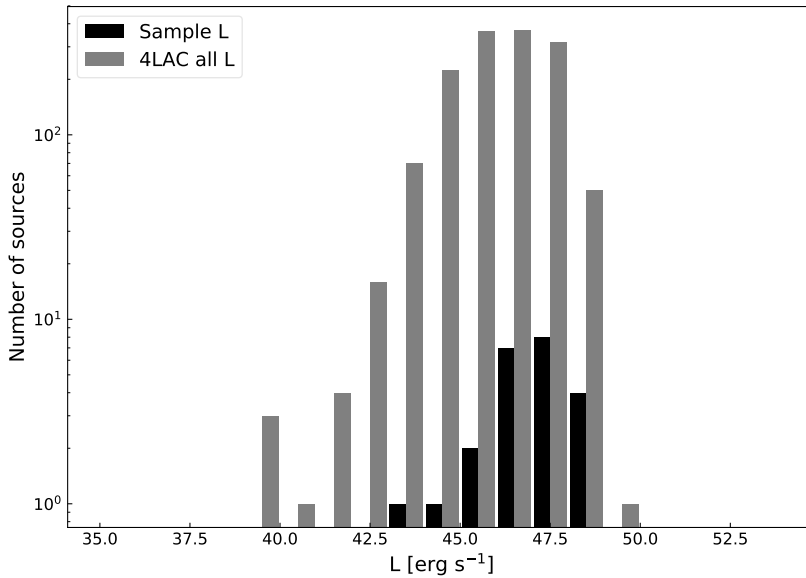
FIGURE 7.3: Luminosity distribution of the loner-flare sample compared to all 4LAC sources with ν_{syn} and redshift information.

- Recreating the original sample's source-type distribution yields 3.702 %

- Assuming the 3 BCUs are actually FSRQs, one obtains 16.527 %.

As an independent method of comparing the loner-flare sample's ν_{syn}- and L-distributions with the 4LAC population, a two-sample KS test is employed. For the ν_{syn} distribution, a p-value of 5.86×10^{-5} results, with a D-statistic of 0.31. The luminosity distributions are more compatible with one another, yielding $p = 0.02$ and $D = 0.45$. However, the KS-tests support the Monte Carlo results that the synchrotron peaks and luminosities among the loner-flare sources are distributed differently than among all 4LAC sources.

To further stress the extreme high-luminosity $-$ low-synchrotron-peak property of the sources in the sample, Fig. 7.4 shows the luminosity plotted against the synchrotron peak for all 4LAC sources, with the ones from the original sample marked

TABLE 7.2: Monte Carlo results summarized

Sample drawing constraints	fraction similar ν_{syn}	fraction similar L
None	0.01 %	0.2 %
4 low-lat. and 19 high-lat. sources	0.005 %	0.344 %
3 BL Lac, 16 FSRQs, 1 RDG, 3 BCU	0.286 %	3.702 %
3 BL Lac, 19 FSRQs, 1 RDG	0.94 %	16.527 %

Monte Carlo results comparing loner-flare-sample ν_{syn} and L with 4LAC respective distributions. For four different selection approaches, 100,000 samples are drawn. Each time, the fraction of samples satisfying the similarity criteria is computed. These criteria are: No sources with $\nu_{syn} > 10^{14}$ Hz; at least 19 sources with $L \geq 10^{46}$erg s^{-1}.
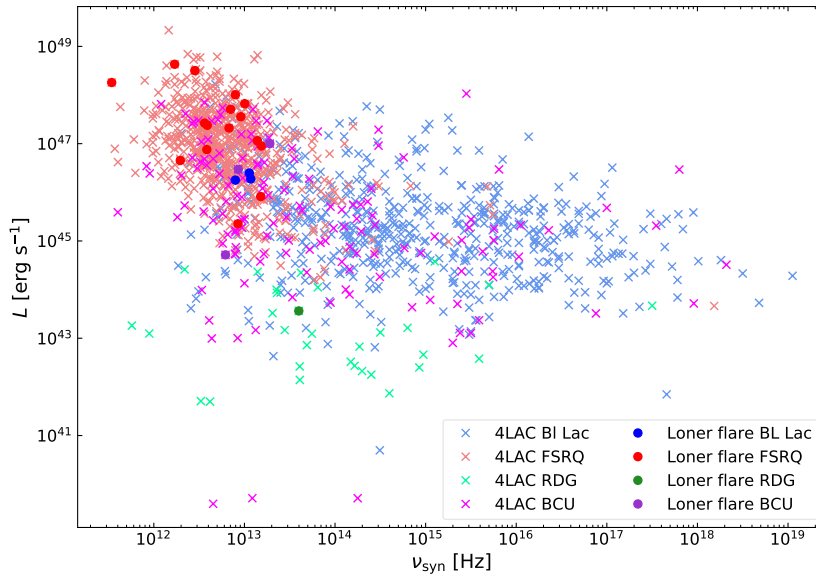
FIGURE 7.4: Luminosity against synchrotron peak position for all
4LAC sources with redshift- and ν_{syn} information. The sources from
the loner-flare sample are marked with larger dots.

with dots. It is apparent that the loner-flaring sources, except the radio galaxy
3C 120, are clustered in a very narrow region of this diagram. This begs the question
what a sample would look like if a lower flux threshold had been chosen and looser
constraints on overall activity had been applied in the sample selection. In order to
get a first impression on whether this trend extends to flares with lower peak fluxes,
all sources from the MSL that showed one flare with at least 1 F.U. peak flux and that
do not exceed 0.5 F.U. outside of that flare are selected. Comparing the resulting 25
source's characteristics with 4LAC paints a very similar picture as with the original
sample, albeit the distribution of ν_{syn} and L is not as narrow. Again, the largest frac-
tion of sources are classified as FSRQs. Figure 7.5 shows the same plot as Fig. 7.4,
but this time showing the extended sample's sources instead of the original ones.
Notably, the resulting distribution is very similar to the original one.

7.2 Flare amplitudes

In order to learn about the intensity of the flares, the flare amplitudes A are calcu-
lated as described in the following. As the sources in the sample have been selected
from the *Fermi* MSL, the available daily-binned data are used to compute the relative
and absolute flare amplitudes. For each sample source, the peak daily flux value is
divided by the catalogued 4FGL flux between 100 MeV and 300 GeV to obtain the
relative flare amplitude A_{rel}. To obtain the absolute flare amplitude A_{abs}, the 4FGL
flux is subtracted from the peak flux respectively. The results are shown in Table
7.1. The sample includes sources with relative flare amplitudes typically between 30
and 90, with one extreme value of $\sim$ 1400 (PKS B1150−108). The calculated flare
amplitudes are then compared to the full MSL. Fig. 7.6 shows the flare amplitude
distributions for both original sample and all monitored-sources-list AGN, includ-
ing only data up to the sample-selection date (2019-10-17, MJD 58763). The source
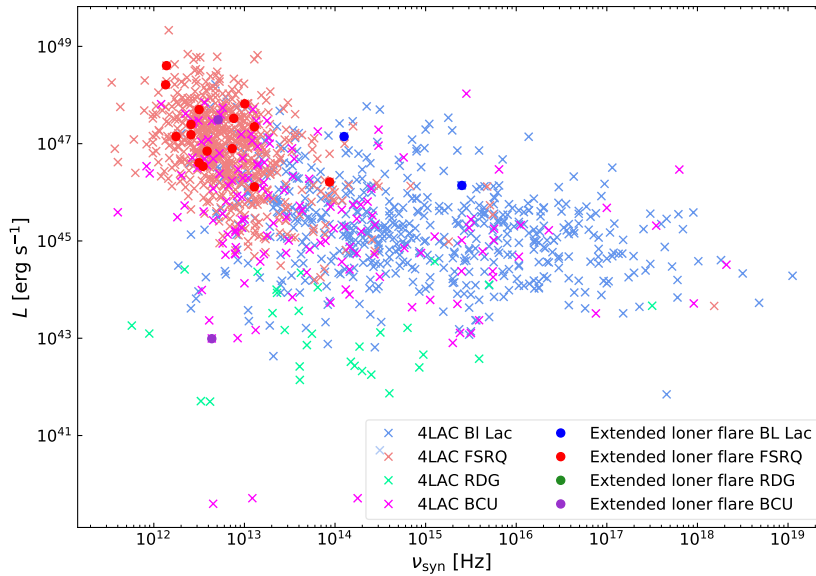
FIGURE 7.5: Luminosity against synchrotron-peak position for all 4LAC sources with redshift- and ν_{syn} information. Dots show sources from the extended loner-flare sample, created by applying a flux threshold of only 1 F.U. and excluding sources that exceed 0.5 F.U. during the remainder of the mission.

PKS B1150−108 is one of only two sources on the MSL that show $A_{rel} > 1000$, and exhibits the single largest flare amplitude on the whole list. Besides PKS B1150-108, there is no evidence that the original 23 sources tend to either extremely low or extremely high flare amplitudes. However, the sample amplitudes appear less spread out.

7.3 Light curves and spectral evolution

As described in Sec. 6.1, a LAT light curve is produced for each source in the sample. The corresponding plots can be found in the respective source section (figs. 7.8-7.30). Upper limits are show for data points with negative test statistic values, as the existence of the source can be assumed. This only excludes non-detections, where the reported fluxes are usually on the order of 10^{-13} ph cm^{-2} s^{-1}, which is below the detection limit. Vertical red lines in the light curves indicate *Swift* ToO observation times. The number of such observations per source varies between 0 and 9. The horizontal light blue line shows the 4FGL catalog value F_{4FGL} (catalog flux) for the flux in the 100 MeV to 300 GeV energy range for each source respectively. The solid black lines show the Bayesian blocks.

The resulting spectra are shown below the corresponding light curve. SED data points and the best fit for each block are shown, with the color changing from blue to red with elapsing time. Black triangles show the energy flux in up to 7 bands as reported in 4FGL. The fit parameters and reduced χ^2 values are summarized in Table C.2 in Appendix C. Parameters that were fixed during the fit are denoted with †. Fig. 7.7 shows the distribution of reduced χ^2. A large number of χ^2 values scatter
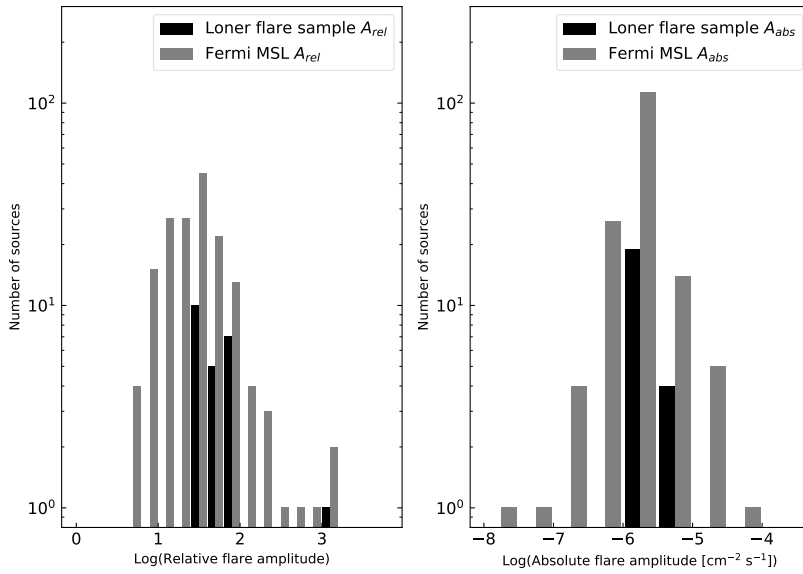
FIGURE 7.6: Left: Distribution of logarithms of relative flare ampli-
tudes for the full *Fermi* MSL and the loner–flare sample. Right: Dis-
tribution of logarithms of absolute flare amplitudes for the full *Fermi*
MSL and the loner-flare sample.

closely around 1 which indicates that the chosen model describes the SEDs well.
Especially in short-duration and low-flux blocks however, the fit quality drops with
χ^2 approaching 0 in some cases. In the following, the results for each source are
described individually.

7.3.1 PMN J0017−0512

The light curve is divided into three blocks, with the first and last ones containing a
number of upper limits. As the flux values in the first block vary around the catalog
value, this marks the very beginning of the flaring activity. The non-detections in
between the data points indicate a very variable flux during this time. Even though
the middle block lasts for more than 10 days, the peak flux is reached three days
into the block after a four-day rise. Within one day, the flux drops by almost an
order of magnitude, where it then stabilizes for a few days before dropping again
to a few times the catalog flux. Due to the low flux especially in the first block, the
corresponding SED provides little information. Notably, PMN J0017−0512 is not
significantly detected above 10^{23} Hz in this block. The second block's SED extends
to above 10^{24} Hz, indicating increased VHE activity. Generally, the energy flux tends
to larger values in the second block. With the third block, the high-energy cutoff
recedes again, and the energy flux declines.

7.3.2 B2 0218+357

B2 0218+357 is a well-known gravitationally-lensed blazar and has, among other
things, been used to calculate the Hubble constant (Biggs et al., 1999). In this work,
its gamma-ray flare between 2012-08-06 and 2012-10-06 is studied, which makes up
the most intense part of the source's prolonged period of activity. During this period,
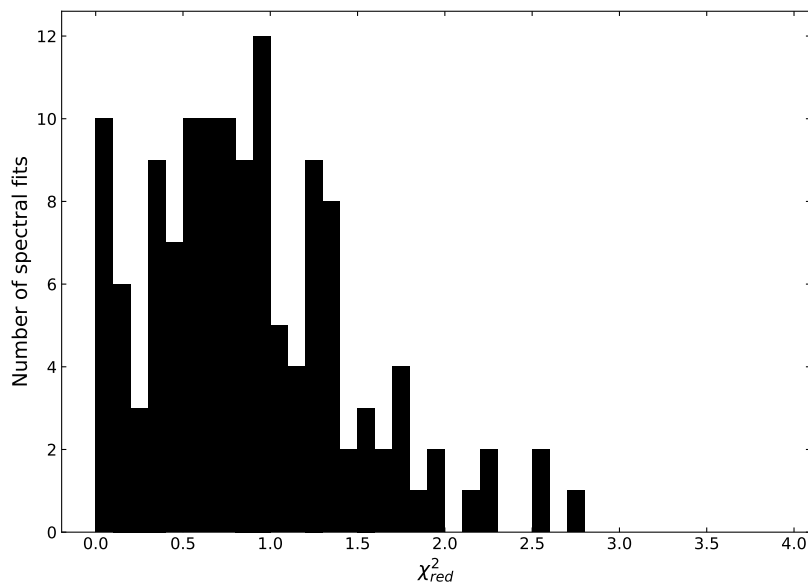
FIGURE 7.7: χ^2 distribution for the log-parabola fits in each Bayesian block.
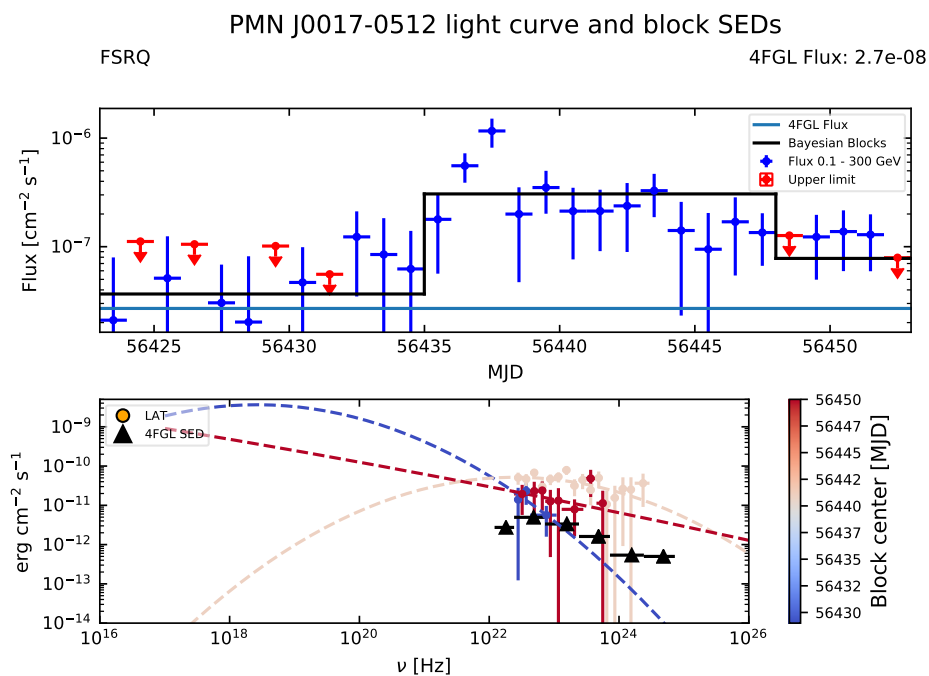
FIGURE 7.8: Top: Daily binned light curve of PMN J0017−0512. Bayesian blocks are shown in black. Bottom: SED of PMN J0017−0512 for each Bayesian block (color bar).
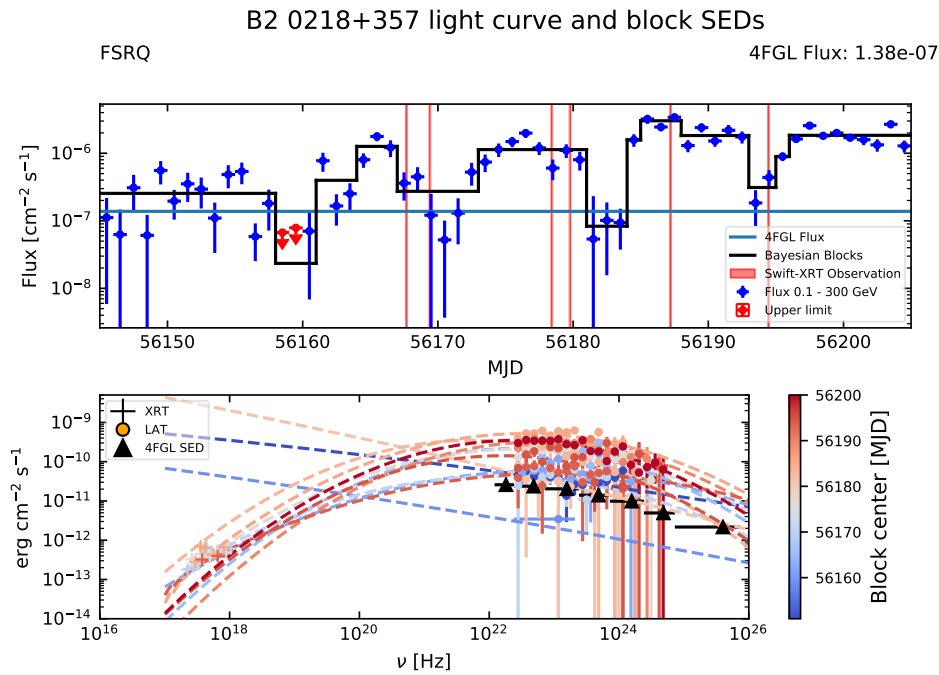
FIGURE 7.9: Top: Daily binned light curve of B2 0218+357. Bayesian blocks are shown in black and *Swift* observations are shown as red shaded regions. Bottom: SED of B2 0218+357 for each Bayesian block (color bar).

five *Swift* observations were taken. As this flare was the "first clear case of a γ-ray detected gravitational lens time delay for any astrophysical system" (Cheung et al., 2014), the source's gamma-ray emission has been extensively studied since (see e.g. Barnacka et al., 2016; Sitarek and Bednarek, 2016).

The created light curve shows high variability and a complex flaring pattern. Indeed, much of this can be attributed to the fact that this source is gravitationally lensed, which leads delayed mirage images. At the beginning of the interval, the flux oscillates around the catalog value before shortly becoming undetectable (block 2). After that, the flux erratically increases (blocks 3 & 4). In block 5 a short drop below the catalog value is seen before the flux increases steadily until the middle of block 6. Thereafter, the flux drops again (block 7) before rapidly increasing in brightness and then reaching its peak flux (blocks 8 and 9). With the exception of a brief but sharp decrease in flux, the source then maintains a flux level of more than 10 times its catalog value. At the end of the interval, the increased activity has not yet subsided as the flux remains in a high state, however the rapid variations from the middle of the interval are no longer visible in the final block. While the SED looks rather flat during the first block, the curvature starts to become apparent in block 3. The energy flux is strongly correlated to the flux, with brighter blocks showing elevated spectra. Higher fluxes and longer blocks come with more VHE information. No shift in the inverse Compton hump is observed, which consistently stays at around 10^{23} Hz. In order to obtain a converging fit for the SED in block 2, the fit parameter α is fixed to its catalog value.
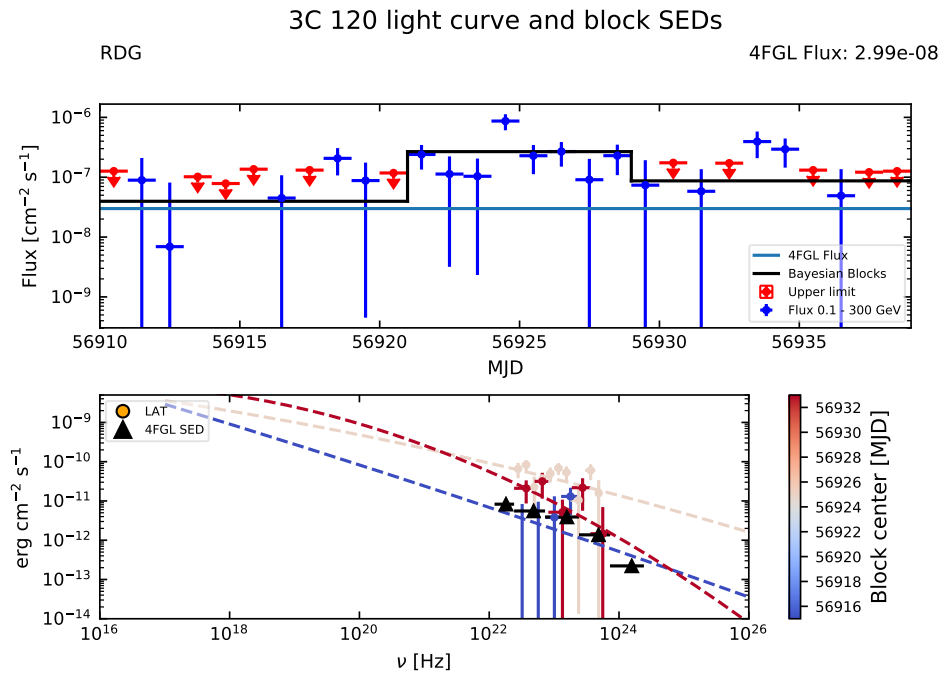
FIGURE 7.10: Top: Daily binned light curve of 3C 120. Bayesian blocks are shown in black. Bottom: SED of 3C 120 for each Bayesian block (color bar).

7.3.3   3C 120

3C 120 has been classified as various different types of AGN over the years, from Sy1 (e.g. Khachikian and Weedman, 1974, Baumgartner et al., 2013) and Sy1.5 (Véron-Cetty and Véron, 2006) to blazar of unknown type (Massaro et al., 2009). 4LAC lists 3C 120 as a radio galaxy. Multiple studies on this source have been carried out in the past (e.g. Tombesi et al., 2017, Rani and Stalin, 2018, Marscher et al., 2018).

According to Sahakyan, Zargaryan, and Baghmanyan (2015), 3C 120 transitioned to a long-term high-luminosity state in 2013 and remained there since, as opposed to the erratic flaring behavior known from blazars. Similar to PMN J0017−0512, 3C 120's light curve is well described with three Bayesian blocks. The light curve starts out at the catalog flux, and then varies between a few times that value and undetectability during the first block. In the second block, the peak flux is reached four days in. After stabilizing and then dropping in flux by a factor of 10 and then to undetectability, the flux increases again for two days at roughly half the peak flux. Finally, the flux decreases below the detection limit. Due to the low statistics during the first and last blocks, the spectral information obtained there is very limited. Thus, for these blocks the spectral index α was frozen to the catalog value taken from 4FGL.

7.3.4   PKS 0440−00

This source has previously been reported in a high state on 2009-05-16 (Ciprini, 2009), but from the LAT mission light curve (see Appendix B) it is evident that the flare studied in this work is much brighter. This FSRQ is a well known optical- and radio source and shows up in many population studies (see e.g. Ghirlanda et al., 2010, Richards et al., 2014). Enhanced gamma-ray emission from this source has
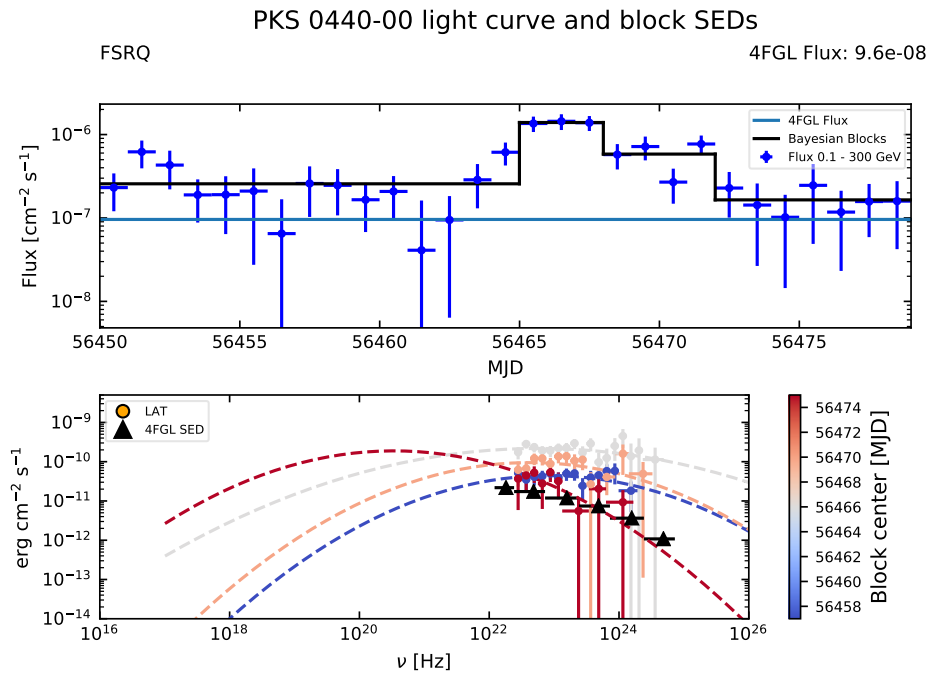
FIGURE 7.11:   Top: Daily binned light curve of PKS 0440−00.
Bayesian blocks are shown in black. Bottom: SED of PKS 0440−00
for each Bayesian block (color bar).

been detected and studied since the 1990s (McGlynn et al., 1997 and Yurchenko,
Marchenko-Jorstad, and Marscher, 2000).
The light curve starts out at an elevated flux level at roughly $2.5 \times F_{4FGL}$ and in-
creases by a factor of six on day two. After that, the flux level settles for the remain-
der of the first block, with a few one- or two-day drops, before it reaches its peak
in block 2. This level is maintained for three days after which the flux level decays
back to its starting point within another five days. Simultaneously, the SED shows
an increase and then drop of the energy flux of a factor of a few.

7.3.5   B2 0552+39A

Paliya et al. (2019) recently carried out a multiwavelength study on B2 0552+39A,
finding that its peak intrinsic jet luminosity is the highest recorded from a $z > 2$
blazar. Three *Swift* observations are available during the interval studied here.
The light curve starts out close to F_{4FGL} and then goes up by a factor of 10 in block 2.
After dropping in flux for one bin towards the end of the second block, the peak flux
is reached in block 3 at almost 100 times F_{4FGL}. In block 4, the light curve stabilizes
at a lower level with some variation similar to block 2 before becoming undetectable
for two days (block 5) and then finally returning to the flux level of block 4. The
spectral information gained from the first and last blocks does not constrain the SED
at all. Thus, 4FGL catalog values are used for both α and β to allow for the fit to
converge. Over blocks 2 through 4 one can see an order of magnitude increase and
then decrease in the energy flux. Even though the high flux during block 3 allows for
a well-constrained LAT SED, its divergence towards lower frequencies is obviously
unphysical. The XRT data available in block 4 constrain the parabola much better
and give a more reasonable estimate of the low-energy SED. Block SEDs where only
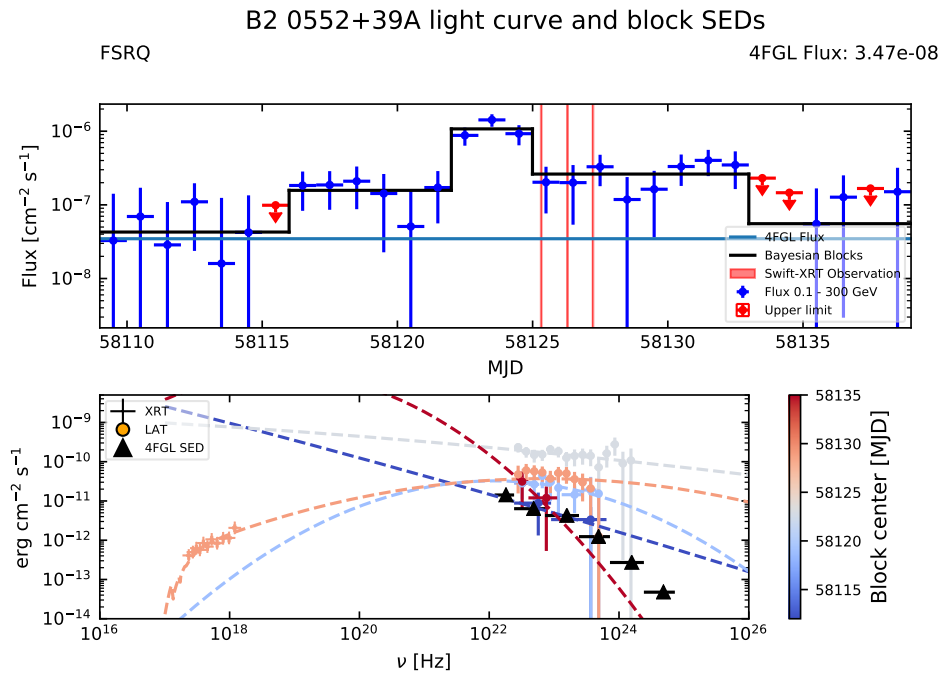
FIGURE 7.12: Top: Daily binned light curve of B2 0552+39A. Bayesian blocks are shown in black and *Swift* observations are shown as red shaded regions. Bottom: SED of B2 0552+39A for each Bayesian block (color bar).

LAT data is taken into account can not necessarily be extrapolated into the X-ray band, especially when the LAT SED is particularly flat.

The quick drop in energy flux within the XRT band can be understood when comparing the n_H column density with the respective values for other sources (see Table C.2 in Appendix C). The value for this source is about an order of magnitude larger than in many other sources.

7.3.6 TXS 0646−176

Besides this source's brightest flare during the period between 2018-12-08 and 2019-01-08, more minor flaring activity in the LAT band has been reported. Only this December 2018 flare, where 2 quasi-simultaneous *Swift* observations are available, is studied here, but this source had been in a high state 6 months prior to this flare (Angioni, 2018) and on November 29, 2018 (Ciprini, 2018). This might indicate an increased activity over an extended period, with multiple smaller flares culminating in one massive outbreak.

Additionally, in 2015 TXS 0646−176 was reported to be in an elevated state of ∼ 0.8 .F.U. by *Fermi* (Ciprini, 2015), which was then linked to an increase in NIR luminosity by Carrasco et al. (2015). No dedicated analysis has been published to date.

As the activity reported from before the flare suggests, the light curve begins at more than 10 times the catalog flux. There are indications for flux-doubling times shorter than the 12 h bins used. After strong fluctuations over the duration of block 2, the flux stabilizes in block 3, maintains its peak flux for one day in block 4 and returns to roughly block-3 flux for another 2.5 d. After this, TXS 0646−176 almost disappears for four days (block 6), then returns to approximately pre- and post-peak flux. After
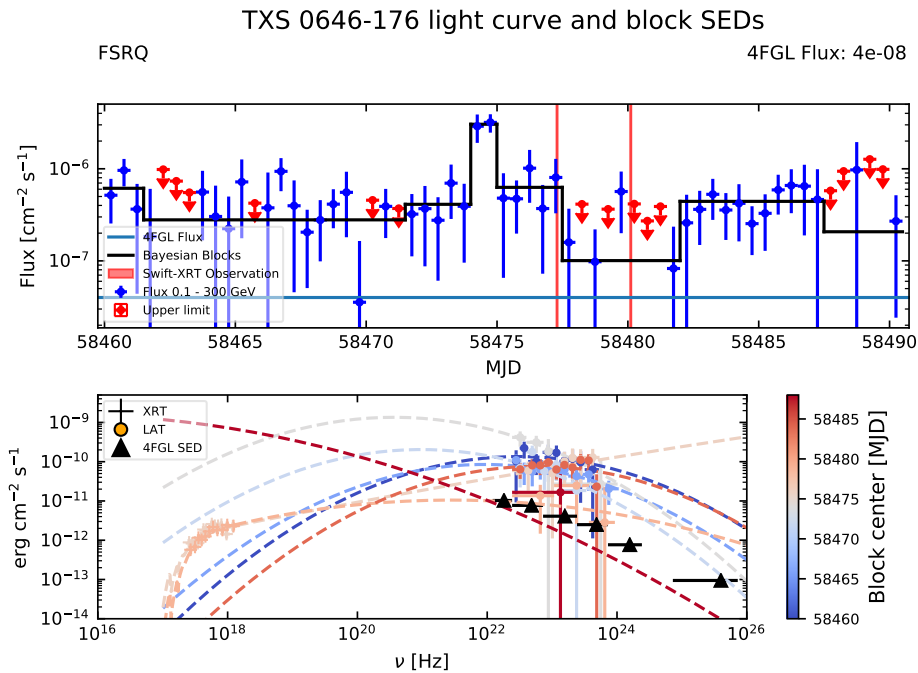
FIGURE 7.13: Top: Daily binned light curve of TXS 0646−176. Bayesian blocks are shown in black and *Swift* observations are shown as red shaded regions. Bottom: SED of TXS 0646−176 for each Bayesian block (color bar).

this, statistics deteriorate, with flux values in the last block consistent with F_{4FGL}. Even though no X-ray data can be used in the first four blocks, the high LAT flux and therefore highly significant detections allow studying the spectral evolution in great detail through the whole flare. Between blocks 1 and 2 the SED is seen dropping, which is consistent with the decrease in flux. Unfortunately, due to the short duration of the peak block, only few well-constrained SED data points are available here. Yet, these points point to a significant increase in energy flux.

Blocks 5 and 6 exhibit surprisingly different spectral shapes, with almost no curvature in block 5 and a strongly curved, quickly dropping spectrum in the subsequent block. In block 6, the number and quality of LAT data points is limited but the available XRT data constrains the SED well. During this block, above 10^{22} Hz, the SED is in good accordance with the information obtained from 4FGL. The quick drop in the XRT data points can again be attributed to the high n_H column density. Block 7 shows another increase in the SED, simultaneous with the rise in flux. In the final block, the large number of flux upper limits again decreases the reliability of the spectral fit. Hence, α is set to the catalog value for this block.

7.3.7   4C +14.23

The most striking feature in the light curve of 4C +14.23 is the second Bayesian block, which only consists of one upper limit. In order to calculate the Bayesian blocks, the actual flux values are considered and not the upper limits, which can explain the identification of this block. The algorithm also takes into account the uncertainties, which are often unrealistically small in low-TS points. Consequently, for this block no SED was computed. Also note the changing point at MJD 55130,
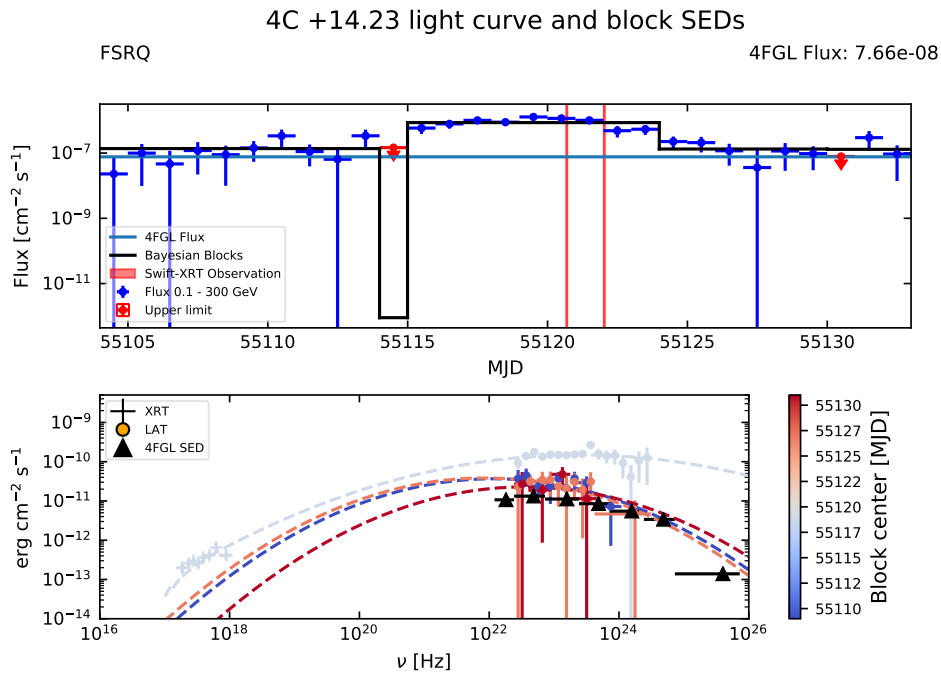
FIGURE 7.14: Top: Daily binned light curve of 4C +14.23. Bayesian blocks are shown in black and *Swift* observations are shown as red shaded regions. Bottom: SED of 4C +14.23 for each Bayesian block (color bar).

which is hardly visible due to the small difference in mean flux. This block could in part also result from the much lower flux for the upper-limit time bin.

This light curve's shape is characterized by flux levels varying slightly around F_{4FGL} during the first block. In the peak-flux block (number 3), fluxes from the blazar about one order of magnitude above the catalog flux are observed over six days with little variation. At the transition to the fourth block, a gradual dimming in two-day intervals is seen until approximately catalog level is reached in the middle of block 4. After that, the flux creeps back up to a higher state, but the non-detection in the previous bin and the drop back to F_{4FGL} afterwards offset this, leading to very similar mean fluxes in blocks 4 and 5. The SEDs at the limiting blocks are characterized by strong curvature and a quick drop in energy flux with increasing frequencies. This is to some degree due to the small number of high-energy data points, most notably in the final Bayesian block, but even here the resulting fit is consistent with the catalog SED from 4FGL. The XRT data in block 3 allows to really constrain the parabola's peak, which is located at higher photon energies than at the beginning of the interval or in the catalog.

7.3.8 PKS 0903−57

While the peak flux during the flare was reported on May 14 in the ATel, it was not possible to center the time range on this date. For a discussion on this, see Sec. 7.3. Notably, this source has recently returned to activity, warranting an ATel from the *Fermi*-LAT collaboration (Buson, 2020).
Due to the sub-optimal time range, PKS 0903−57's flux starts out at more than 10

PKS 0903-57 light curve and block SEDs
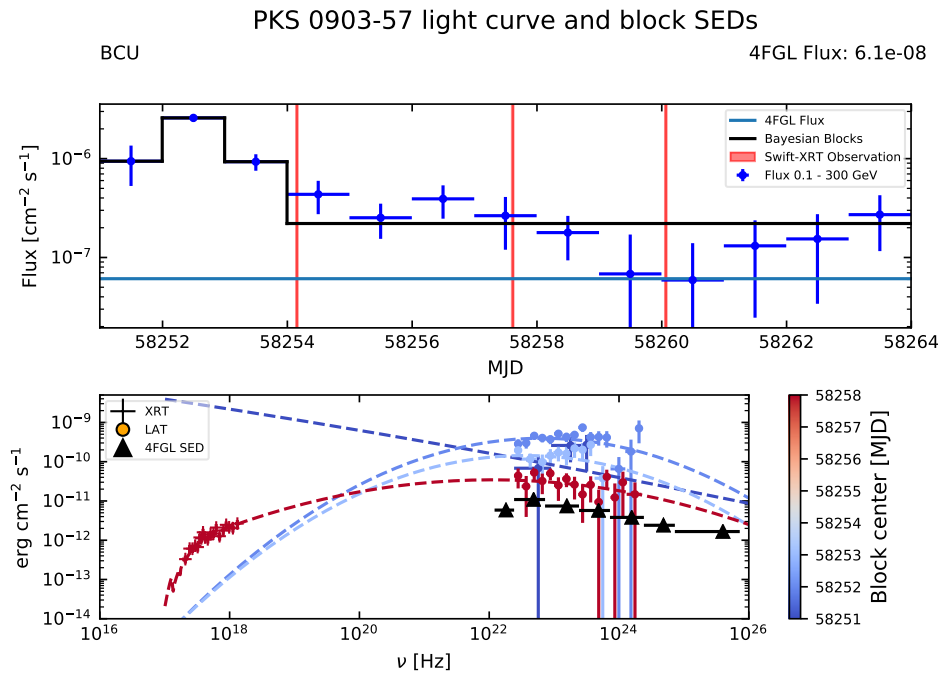
FIGURE 7.15: Top: Daily binned light curve of PKS 0903−57. Bayesian blocks are shown in black and *Swift* observations are shown as red shaded regions. Bottom: SED of PKS 0903−57 for each Bayesian block (color bar).

times F_{4FGL} and then more than doubles within one day to reach its peak flux (block 2). Afterwards, the flux declines to its starting point (block 3), to then meander around three times F_{4FGL} for four days. Towards the end of block 4, the flux drops to the catalog value and then recovers back to its previous level at $3 \times F_{4FGL}$. The first three blocks indicate a very symmetrical flare, but in order to confirm or falsify this claim, more data from before the flare are needed.

The most striking property of the source's SED evolution is the flat LAT spectrum during the first three blocks, i.e. the main part of the flare. Up to energies of 10^{24} Hz, no drop in energy flux during block 2 is observed, and in block 3, the LAT SED rises up to almost 10^{24} Hz. Even in the final block, where XRT data further constrain the SED, the spectrum is flatter in the LAT band than other sources and extends to higher energies.

7.3.9   PKS 0906+01

Like 4C +14.23, the light curve of PKS 0906+01 contains an artifact of the Bayesian blocks algorithm in block 4: This is most likely another misidentification, due to one low-TS data point being surrounded by well-constrained, high-flux, time bins. As the light curve's first block contains equal numbers of upper limits and data points, some of which have very large uncertainties, it is no surprise that the resulting SED for this block hardly constrains the spectrum at all. Blocks 2 and 3 provide more data points, but for $\nu \geq 10^{23}$ Hz, the errors become too large to make strong claims about the peak position. The last block's SED seems to show a much narrower inverse Compton hump with the peak at around 10^{23} Hz. A narrow peak like this would also be consistent with the large errors in the previous block's SEDs. In cases like this
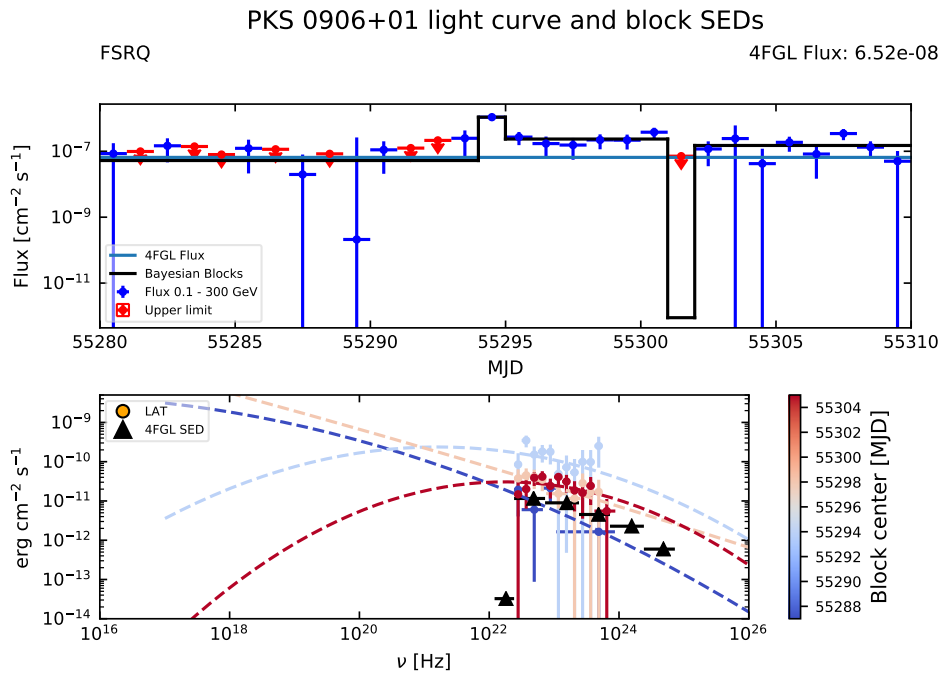
FIGURE 7.16: Top: Daily binned light curve of PKS 0906+01. Bayesian blocks are shown in black. Bottom: SED of PKS 0906+01 for each Bayesian block (color bar).

one, multiwavelength data from the low end of the IC hump is crucial to investigate the shape of the peak.

7.3.10 S4 0954+65

S4 0954+65 has been known as a gamma-ray source since the EGRET era (Mukherjee et al., 1995). This source is one of the better-studied blazars in the sample due to its frequent activity in other bands, where multiple flares have been reported in the past (see e.g. Morozova et al., 2014, Bachev, 2015, Kapanadze et al., 2018a). It is also known to exhibit intra-day variability (Wagner et al., 1993, Gabuzda et al., 2000). While the Bayesian blocks algorithm identifies the first 14 days of this light curve as one block, some features are visible in the shape of the first block's flux evolution. The mean flux in this block is almost identical with F_{4FGL}, but in bins 4 to 5 and 9 to 10, the flux drops by a factor of ~ 4 and then recovers within two days. As the last two bins in the first block are upper limits, the flux increases between the end of block 1 and the peak block (2) by at least a factor of 20. For one day, the flux then drops to an intermediate level before rising again to almost the peak flux for a duration of three more days. The first two data points in the last block show the flux decreasing again back to around its initial value, and afterwards similar behavior as in block 1 is seen. Finally, during the last four days of the flare interval, S4 0954+65's flux drops below the *Fermi*-LAT detection limit. The SED shapes in blocks 1, 2 and 4 are consistent with one another, with higher fluxes going hand in hand with higher energy fluxes and higher cutoff energies. Due to the small number of SED data points in block 3, no useful spectral information can be extracted from this block. Contrary to the pronounced curvature in the discussed blocks' SEDs, the final block shows a very flat spectrum. Because there are so many more XRT data points than
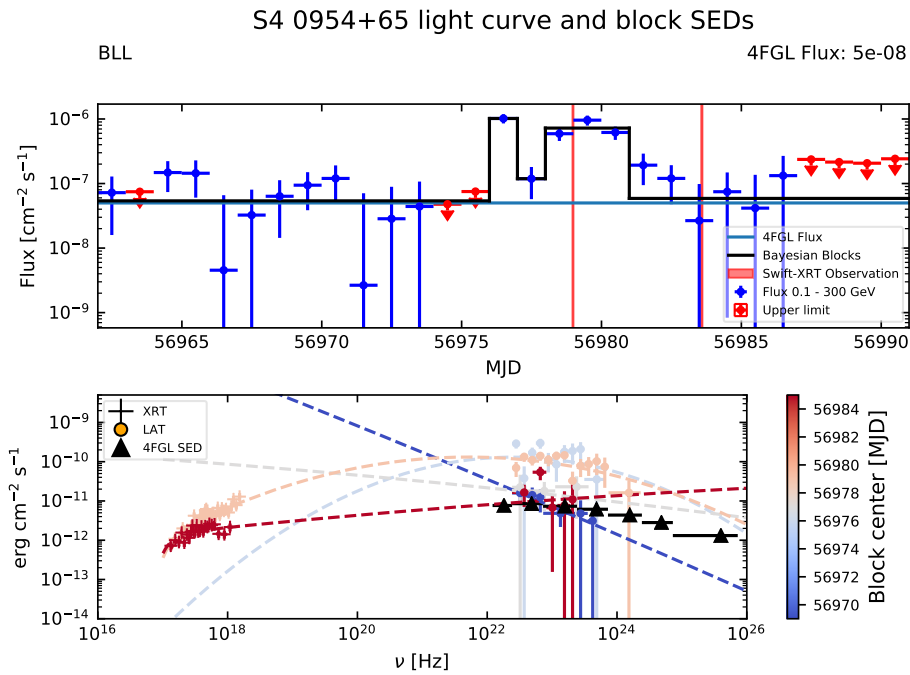
FIGURE 7.17: Top: Daily binned light curve of S4 0954+65. Bayesian blocks are shown in black and *Swift* observations are shown as red shaded regions. Bottom: SED of S4 0954+65 for each Bayesian block (color bar).

LAT data points, the curved shape of the latter is given less weight in the spectral fit, thus leading to this power-law-like SED at $\nu > 10^{18}$ Hz.

7.3.11 PKS B1150−108

The selected time range for this source was chosen in spite of the reported flare date on November 11. Similar to PKS 0903−57, due to effective non-detections in any time bins before the chosen range, the interval had to be adapted in order to obtain reliable data.

The light curve of PKS B1150−108 is divided into three blocks. In the first block, the flux increases over three days, starting out at a flux with a best value of $\sim 9 \times 10^{-2}$ F.U., which is consistent with F_{4FGL} within its uncertainties. In the central block, with a duration of three days, the blazar reaches its peak flux on day 2, almost 500 times brighter than F_{4FGL}, making it the source with the highest flare amplitude in the loner-flare sample. In block 3, there are fluctuations around the average flux level of block 1. While the source wasn't significantly detected before the flare, it maintains a high state for a prolonged time after the flare. The resulting SEDs are very ambiguous due to the small number of available data points. The only information that can be readily extracted is the increased energy flux when compared to the catalog level. Only two SED data points are available in the first two blocks. The last block, where two XRT data sets are taken into account yields some information on the SED, but even here, the total number of XRT counts is so small that they result in a single bin, and the errors on two of the LAT data points are very large. Three additional XRT observations were taken during the studied interval, but a number of them with exposures on the order of a few seconds and a resulting count rate of
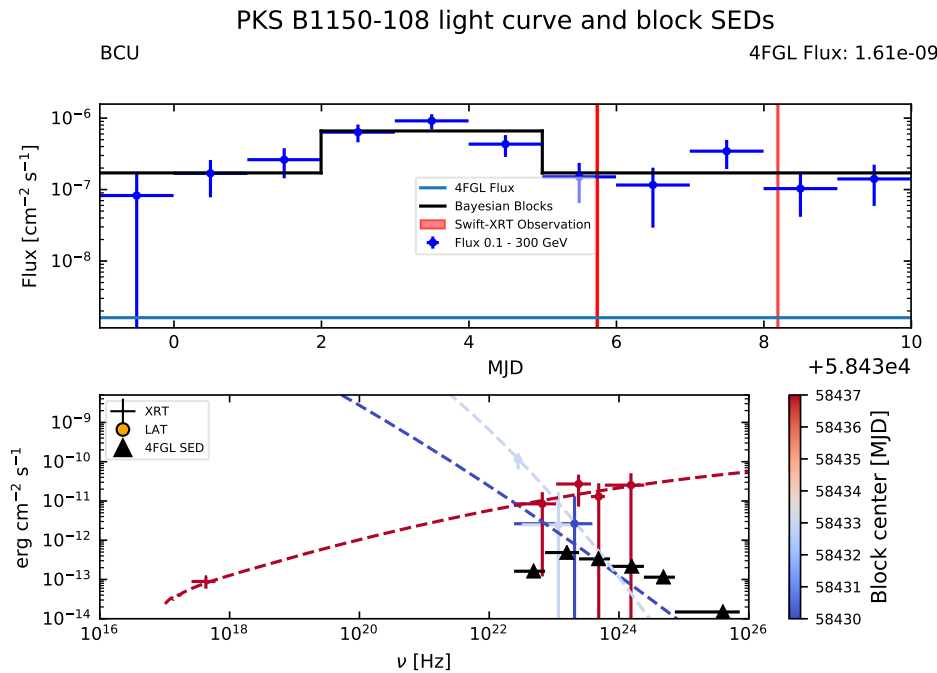
FIGURE 7.18: Top: Daily binned light curve of PKS B1150−108. Bayesian blocks are shown in black and *Swift* observations are shown as red shaded regions. Bottom: SED of PKS B1150−108 for each Bayesian block (color bar).

0. Observations 00010986001, 00010987001 and 00010984004 are thus excluded from the analysis. The difficulty constraining the SEDs from this source is possibly connected to the fact that this source is flagged in 4FGL (see Sec. 4.2), and thus not much weight can be put on the analysis of PKS B1150−108.

7.3.12 4C +49.22

4C +49.22 has been the target of a number of studies (see e.g. de Rosa et al., 2008, Cutini et al., 2014, Zhang et al., 2018) and has been observed with VLBI methods a few times over the last decades (e.g. Akujor and Garrington, 1991). Notably, this source has recently returned to a flaring state (Cutini, 2019), albeit only at about half the flux level of the flare studied in this work.

At the beginning of the interval, the LAT detects a flux about three times the 4FGL level. Over the duration of the first block, the flux fluctuates intensely, with flux-doubling times shorter than the bin size of one day. During block 2 and up to the highest-flux bin in block 3, the flux rises following a power-law shape, and then declines in a similar manner over the duration of three more days. After this decline, in the fourth block the flux stabilizes at a few times F_{4FGL}. Block 5 shows a two-day dip in the light curve, with the flux averaging out at the catalog level. Finally, the flux increases back to 10 times F_{4FGL} and then slowly decays during block 6. Over the first two blocks, the spectral index flips from a falling to a rising LAT spectrum. Blocks 3 and 4 contain *Swift*-ToO observations. The XRT data points in combination with the LAT spectrum again show a very flat spectrum, with XRT and LAT data both reaching higher energy fluxes in the peak block (3). Block 5 yields almost no spectral information, and even though the available data points are reasonably well
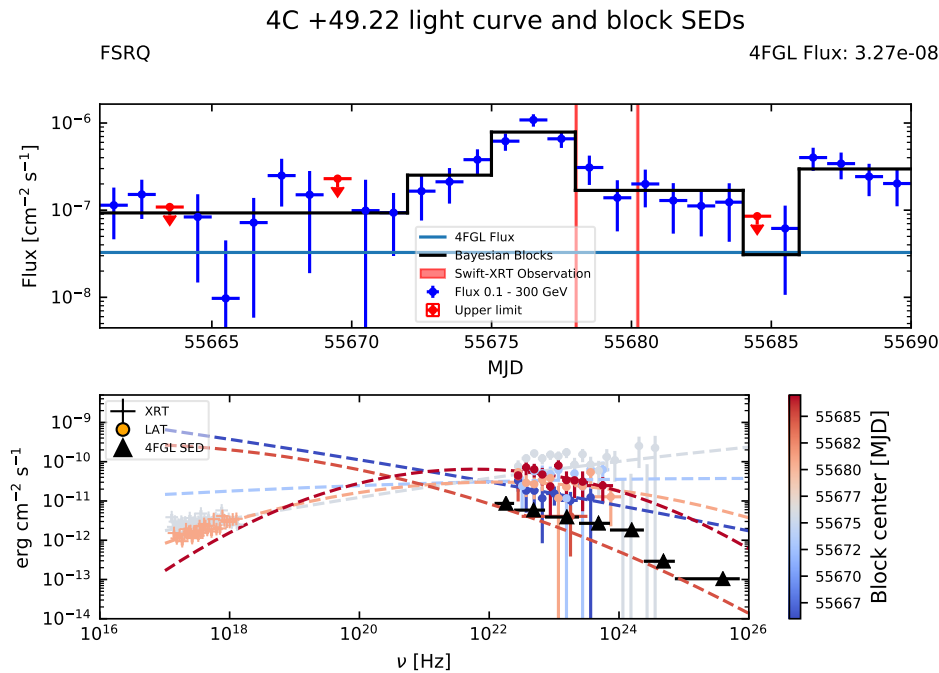
FIGURE 7.19: Top: Daily binned light curve of 4C +49.22. Bayesian blocks are shown in black and *Swift* observations are shown as red shaded regions. Bottom: SED of 4C +49.22 for each Bayesian block (color bar).

constrained, to obtain a converging fit α and β are fixed. This leads to a LAT SED consistent with the 4FGL SED. Block 6 produces the spectrum with the highest curvature. In 4FGL, this source's LAT SED is described with a power law. The chosen log-parabolic model reproduces this over the first three blocks, even when XRT data are included.

7.3.13 GB 1310+487

Because GB 1310+487 became one of the brightest GeV sources during this flare, it has been studied in detail by Sokolovsky et al. (2014). Further research include Kang (2017), who carried out a study on the size of the γ-ray-emitting region of 1310+487, and Yang and Zhou (2016), who investigated synchrotron self-Compton (SSC) + external Compton (EC) as radiation mechanisms.

The beginning of the light curve is best described as rapid fluctuations around a level slightly above F_{4FGL}. During the first block, the SED is falling for higher frequencies over the full LAT band. Then, over the next five days, which are divided into three separate blocks, the flux as well as the SED increase dramatically, with the SED reaching 10^{-9} erg cm^{-2} s^{-1} and extending up to 10^{25} Hz during the peak block. Simultaneously, the SED peak has shifted to higher energies, into the LAT band. After a short drop in block 5, flux and SED rise again, and due to the XRT coverage, the decay of the high-energy hump between blocks 6 and 7 can be seen. In blocks 8 and 9, the flux further decreases, and in block 9 the SED drops by almost an order of magnitude. In block 10, the flux sharply rises again and then wildly varies around 10% the peak flux. Due to the short duration and low flux of the last block, the SED is not well constrained here.
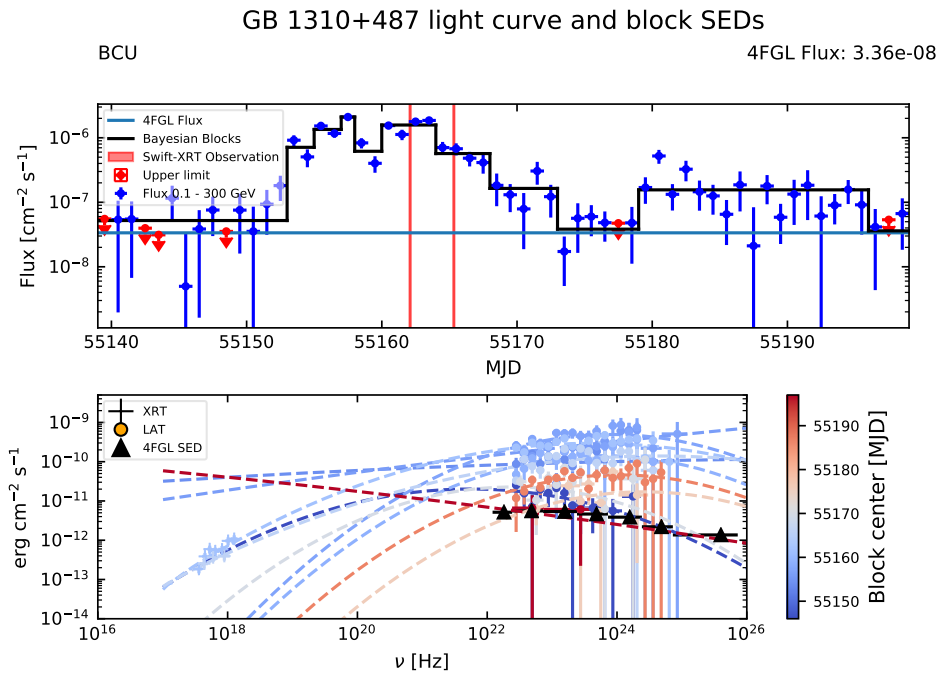
FIGURE 7.20: Top: Daily binned light curve of GB 1310+487. Bayesian blocks are shown in black and *Swift* observations are shown as red shaded regions. Bottom: SED of GB 1310+487 for each Bayesian block (color bar).

7.3.14 PKS 1454−354

The flare in question was the first time enhanced γ-ray emission had been detected from this source. Therefore, shortly afterwards, a paper on PKS 1454−354 was published by the LAT collaboration (Abdo et al., 2009).
The binning in this light curve is set to 6 hours. This leads to larger uncertainties in times of lower flux, but the gain in temporal resolution around the peak flux offsets this disadvantage. The first two Bayesian blocks are characterized by rapid variations around a few times F_{4FGL}. In block 3, the flux stabilizes for five bins at half the previous level. Some more fluctuations can be seen, but towards the end of block 3 the flux starts increasing systematically, well into block 4. During block 4, which comprises five time bins, the peak flux of more than 3 F.U. is measured. In block 5, the flux declines again, and in block 6 returns to rapid fluctuations at a similar level as before the peak. The final block exhibits a higher average flux, but the flux variations cover a similar range as in the previous block. The SEDs of the first three blocks are consistent with one another, even though the short duration of block 2 leads to fewer data points, especially at higher frequencies. During the peak flux, the energy flux increases as well, with the SED extending to higher energies. After the flux had dropped again, *Swift* took one observation in block 6. These additional data points dramatically alter the best fit for the SED, suggesting a much lower curvature than when only LAT data is considered. However, only two XRT data points are used for this fit.

PKS 1454-354 light curve and block SEDs
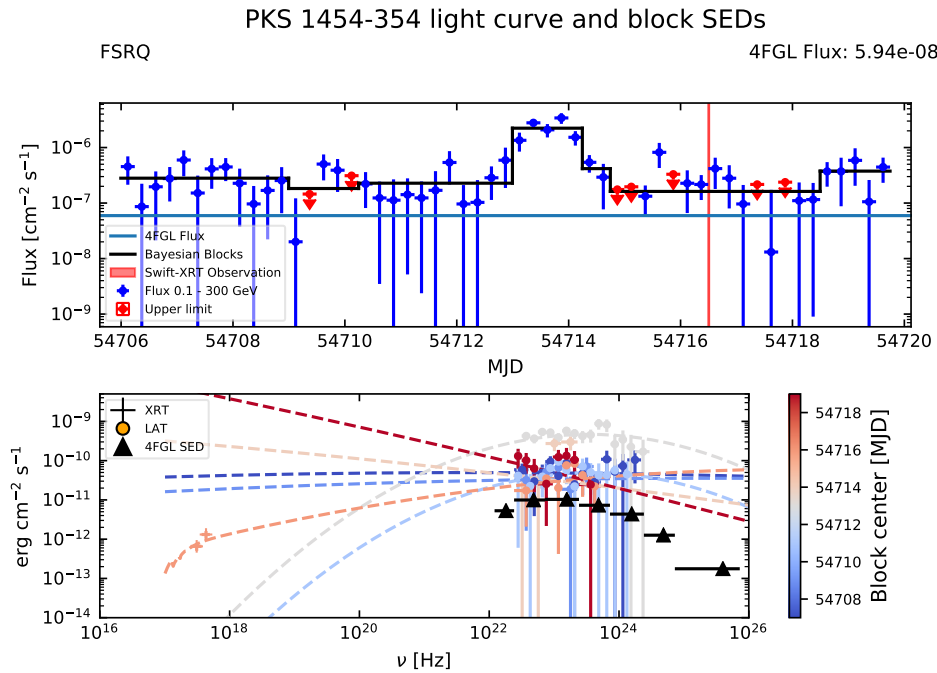
FIGURE 7.21: Top: Daily binned light curve of PKS 1454−354. Bayesian blocks are shown in black and *Swift* observations are shown as red shaded regions. Bottom: SED of PKS 1454−354 for each Bayesian block (color bar).

B2 1504+37 light curve and block SEDs
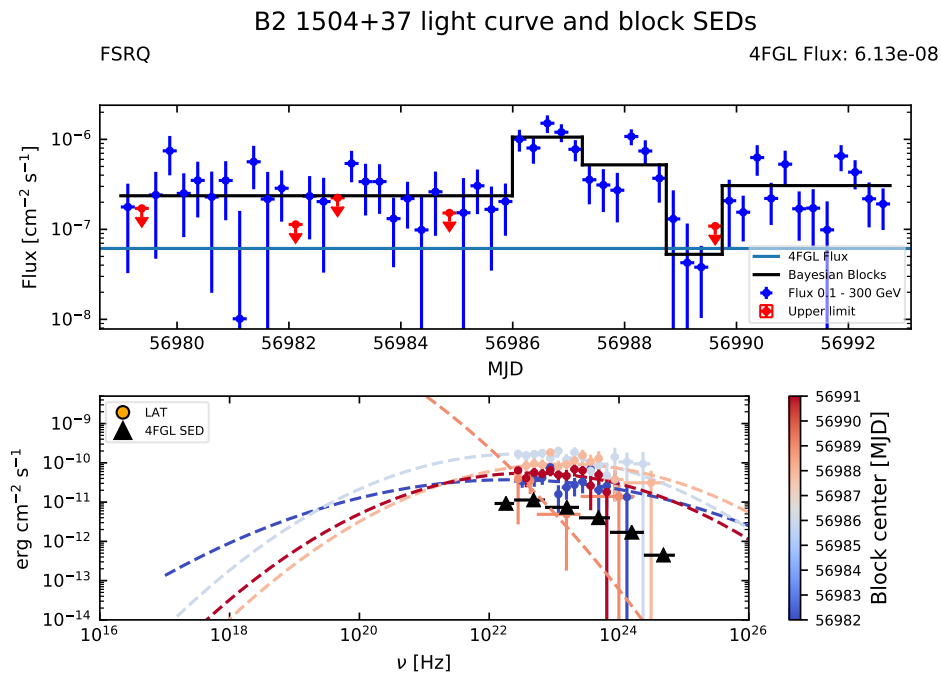
FIGURE 7.22: Top: Daily binned light curve of B2 1504+37. Bayesian blocks are shown in black. Bottom: SED of B2 1504+37 for each Bayesian block (color bar).
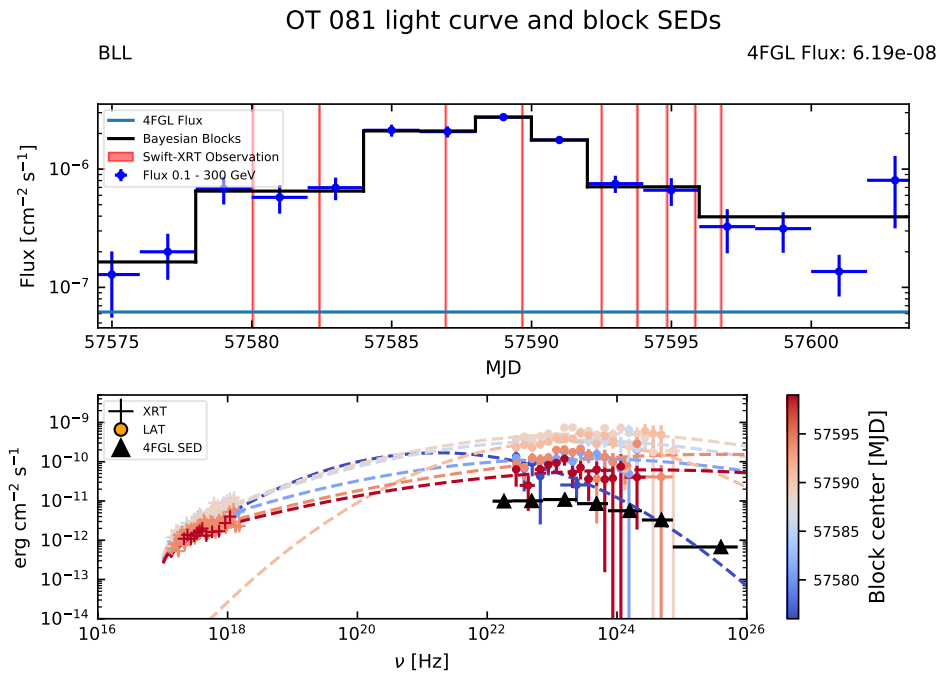
FIGURE 7.23: Top: Daily binned light curve of OT 081. Bayesian blocks are shown in black and *Swift* observations are shown as red shaded regions. Bottom: SED of OT 081 for each Bayesian block (color bar).

7.3.15 B2 1504+37

Before this study, Carilli et al., 1997 and Kanekar and Chengalur, 2008 have investigated radio-absorption features in the direction of B2 1504+37.

The light curve's first Bayesian block is characterized by fluctuations around a mean level of $\sim 4\,F_{4FGL}$, with a few upper limits and one flux point at $< 20\,\%F_{4FGL}$. Between the last time bin of block 1 and the first bin in block 2, the flux increases by a factor of five within six hours. The second block shows the overall highest flux in this light curve. Over the last three bins of block 2, the flux decreases, and this trend continues for another three bins in the subsequent block. Between the third and fourth bin in this block (3), another dramatic increase similar to the one between blocks 1 and 2 is observed, after which the flux drops quickly to below F_{4FGL} in block 4. Block 5 shows the flux stabilizing at a level similar to block 1, with rapid fluctuations around the average level.

The SED in the first block differs from the remaining ones, as the curvature is less pronounced. Blocks 2 and 3 show significant detections up to higher energies than the remaining intervals. Due to the short duration and low flux in block 4, the spectral information that can be extracted from this period is very limited. The shape of the SED in the final block is consistent with blocks 2 and 3, albeit at a lower energy flux.

7.3.16 OT 081

Kapanadze et al., 2018b studied the enhanced X-ray emission from OT 081 between October 2016 and April 2017, while Uemura et al., 2017 did optical polarization measurements. Additionally, Kim et al., 2018 performed a multiwavelength study on

this source, making it one of the better-studied source in the sample. During the chosen time range, OT 081 has more *Swift*-XRT observation than any other source in the sample.

At the beginning of the interval, the flux starts out at around twice $F_{4\text{FGL}}$ and slightly increases during the first Bayesian block. Block 2 shows a very stable flux level for three time bins, but between blocks 2 and 3, the flux more than doubles to 2 F.U., and maintains this level for the duration of block 3. Block 4 contains only the highest-flux bin. After the peak, the behavior from the onset of the flare is mirrored, with the flux dropping in large steps. In block 6, OT 081 maintains a flux level similar to the level in block 2 for two more time bins. Only in the final block do strong fluctuations arise, with the flux ranging from its starting value to a value similar to the ones obtained in blocks 2 and 6.

In this source, the first XRT observation in block 6 (between MJDs 57592 and 57596, ObsID 00036392031) shows a count rate outside of the error margins of the last two observations in the same block, ObsIDs 00036392033 and 00036392035 (see also Sec. 6.3 and Fig. 6.7). However, while the count rates do not fall within their respective 2σ errors, they lie within 3σ of each other. The absolute difference between the smaller count rate's upper bound and the larger rate's lower bound is less than 5% of the lower rate's value. Thus, these XRT observations are still combined in the same fashion as before, while pointing out this caveat.

As six out of the total eight blocks contain simultaneous *Swift* observations, the SED is generally well constrained. During the peak flux, the SED extends up to 10^{25} Hz, with an order-of-magnitude increase in energy flux compared to block 8. The blocks that do not have additional XRT data points show SEDs with overestimated curvatures, with the first block's SED showing the IC peak at a frequency almost three orders of magnitude lower than in the remaining SEDs.

7.3.17 B2 1846+32A

Shortly before the flare studied here, Kida et al., 2010 published a study on radio variability from B2 1846+32A.

The first and last light-curve bins show fluxes consistent with $F_{4\text{FGL}}$. The first block is characterized by intense flux variations, with indications of doubling times shorter than the bin size. In the second block, the flux rises steadily for the first three bins and then drops quickly, before dramatically increasing again into block 3, where it almost reaches its peak value. The second half of block 3 shows a flux decrease, with the flux recovering in block 4, where it reaches its peak in the final time bin. Between the peak flux and the following time bin, the flux drops by a factor of ~ 5 into the final block, where the light curve is once more characterizes by strong fluctuations.

From blocks 3 and 4, the most accurate spectral information can be extracted due to the additional XRT data points. These two SEDs suggest a flattening of the IC peak during the period of highest flux, which is also supported by the higher maximum frequency in block 3. However, this is not further investigated.

7.3.18 B2 1846+32B

Different from most other light curves in the sample, B2 1846+32B's flare is clearly divided into three parts: The pre- and post-flare phases (blocks 1 and 3), each characterized by strong fluctuations around an average level slightly above $F_{4\text{FGL}}$, and the peak-flux phase (block 2), with a much higher flux and no variations. During block
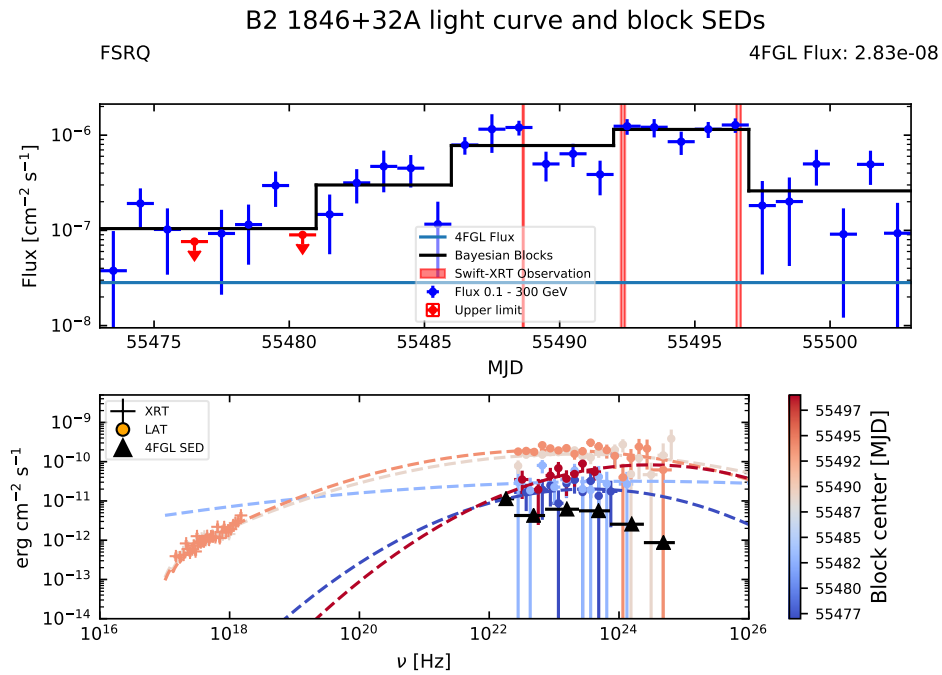
FIGURE 7.24: Top: Daily binned light curve of B2 1846+32A. Bayesian blocks are shown in black and *Swift* observations are shown as red shaded regions. Bottom: SED of B2 1846+32A for each Bayesian block (color bar).
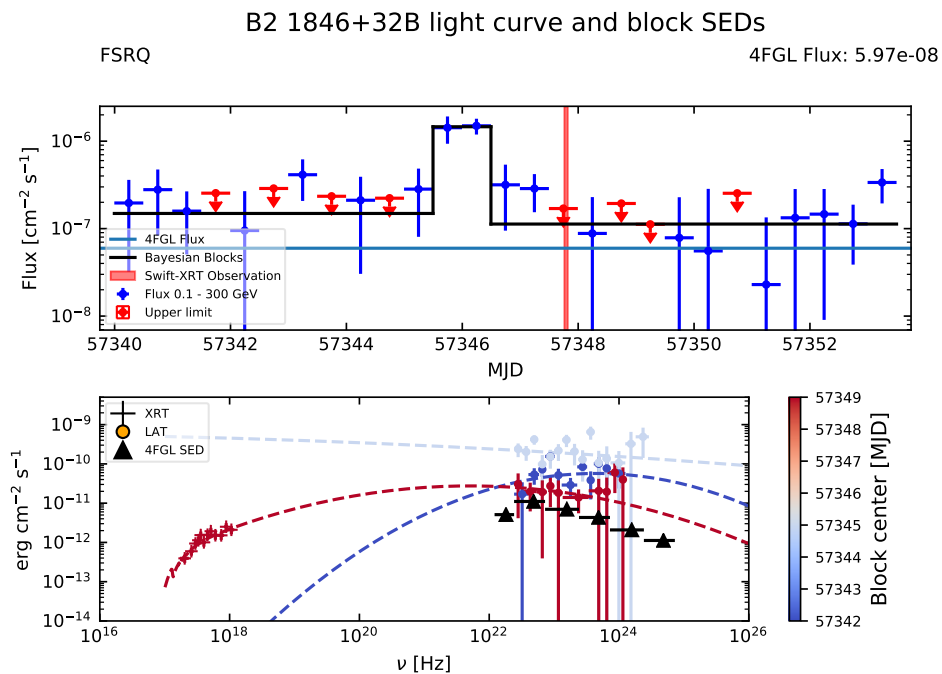
FIGURE 7.25: Top: Daily binned light curve of B2 1846+32B. Bayesian blocks are shown in black and *Swift* observations are shown as red shaded regions. Bottom: SED of B2 1846+32B for each Bayesian block (color bar).
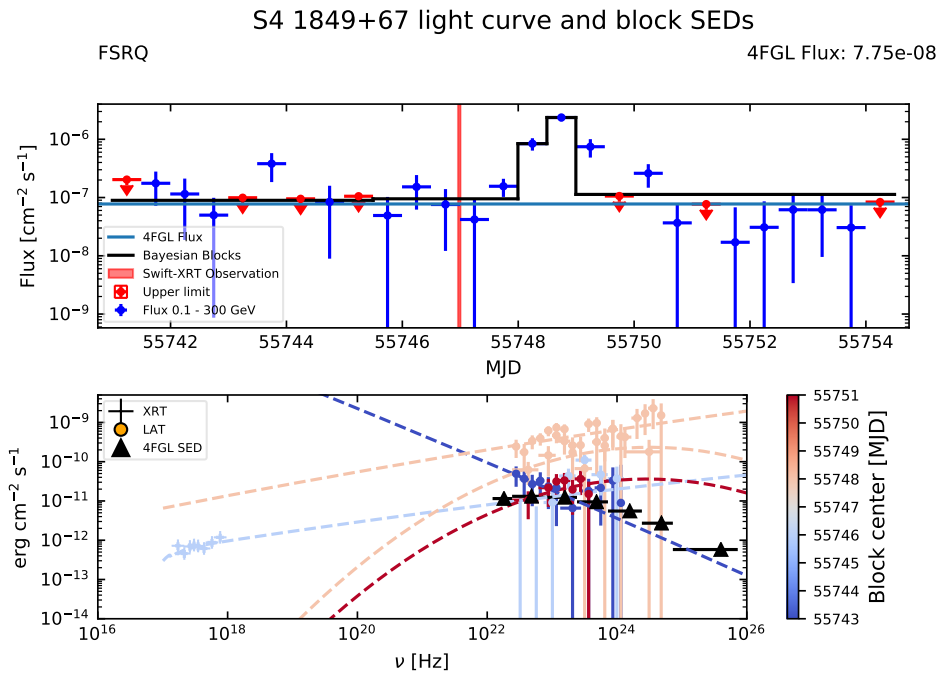
FIGURE 7.26: Top: Daily binned light curve of S4 1849+67. Bayesian blocks are shown in black and *Swift* observations are shown as red shaded regions. Bottom: SED of S4 1849+67 for each Bayesian block (color bar).

2, the SED extends to higher energies and shows higher energy fluxes while flattening significantly. The final block's SED contains XRT data points, thus constraining the SED much better than in block 1. Even without additional X-ray data, a higher energy flux is seen before the flare than afterwards, but still an order of magnitude below the highest-measured energy flux.

7.3.19 S4 1849+67

This light curve shows similar behavior to the one from B2 1846+32B, with clear pre- and post-flare phases, the main difference being that the period of peak flux and the pre-flare phase are subdivided into two blocks each. Blocks 1 and 2 show similar, intense variations around F_{4FGL}, with doubling times shorter than the bin size. Consequently, due to their similar mean flux, these blocks are not easily discernible in the corresponding figure. Block 3 exhibits an intermediate flux level, showing a steady rise towards the peak flux in the subsequent block (4). Afterwards, in block 5, the flux decreases rapidly, falling below F_{4FGL} before stabilizing at around the starting point.

During the peak, the observed SED shows energy fluxes two orders of magnitude above the starting point below $\nu = 10^{24}$ Hz together with an increased very-high-energy component. The X-ray data in block 2 indicates a flat spectrum, which is reproduced in block 4, and only blocks 3 and 5 show notable spectral curvature.
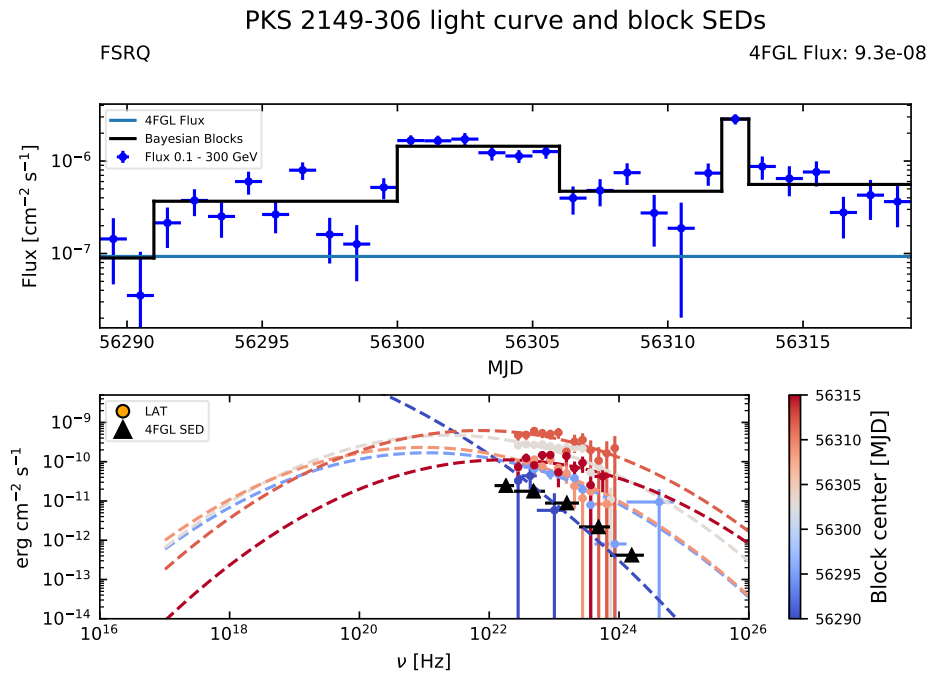
FIGURE 7.27: Top: Daily binned light curve of PKS 2149−306. Bayesian blocks are shown in black. Bottom: SED of PKS 2149−306 for each Bayesian block (color bar).

7.3.20 PKS 2149−306

This flare is also discussed in D'Ammando and Orienti, 2016, while Tagliaferri et al., 2015 study the multi-frequency properties of this high redshift blazar. In 2009, PKS 2149−306 was first studied by Bianchin et al., 2009, using the XMM-Newton, INTEGRAL, and *Swift* instruments.

The first Bayesian block shows fluxes consistent with F_{4FGL}, while block 2 exhibits an overall increased flux level with strong fluctuations between individual bins. Block 3 is characterized by a stable, high flux level, before the source resumes the fluctuating behavior from block 2 in block 4. Block 5 contains the highest-flux point, making it appear like the flare in question is actually divided into two sub flares (blocks 3 and 5), after which the flux again returns to fluctuating around a few times F_{4FGL}. The SED evolution paints the same picture as the light curve, with the highest energy fluxes also occurring in blocks 3 and 5, and the SEDs in blocks 2, 4 and 6 showing very similar behavior. Due to the low flux and short duration of the first block, the SED is not well constrained at all in this block.

7.3.21 PKS 2155−83

PKS 2155−83 is a FSRQ at redshift $z = 1.865$ that was first mentioned in a radio survey perfomed by Preston et al., 1985. The beginning of the light curve is characterized by a flux state below the 4FGL catalog level. During the first block, the flux increases and exceeds the catalog flux in the last time bin. In the second block, the peak flux is reached, with some fluctuations around the increased flux state. Block 3 shows similar fluctuations, albeit around a lower average flux level, with fluxes decreasing over time. During the last Bayesian block, the source exhibits a mean flux

PKS 2155-83 light curve and block SEDs
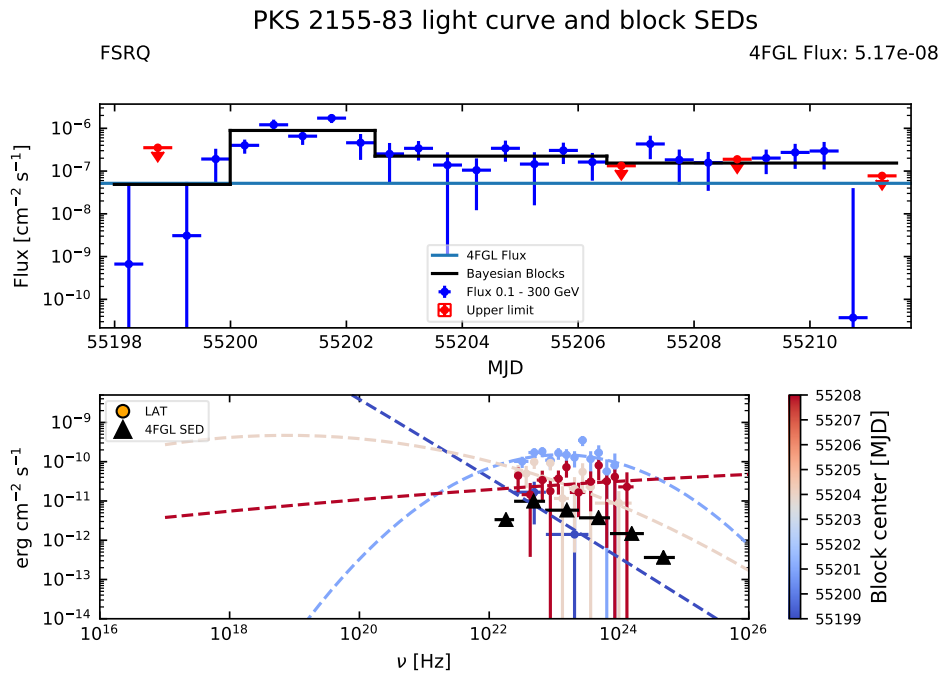
FIGURE 7.28: Top: Daily binned light curve of PKS 2155−83. Bayesian blocks are shown in black. Bottom: SED of PKS 2155−83 for each Bayesian block (color bar).

slightly below the mean in the previous block, which is mostly due to the very low flux towards the end of the interval and a number of low-significance points (upper limits).

While the first block contains almost no spectral information and the resulting fit is questionable at best, the SEDs in the subsequent blocks are much better constrained. During the period of highest flux (block 2), the SED peaks between 10^{23} Hz and 10^{24} Hz, with a very pronounced, log-parabolic shape. The uncertainties in the SED are larger in block 3, and the energy fluxes are generally found at lower values. As the final block is characterized by a number of low-statistics data points, the SED shows a different shape with almost no curvature in this block, but at same the time, the highest-energy bin is found in this block.

7.3.22 NRAO 676

After this flare, NRAO 676 was in an elevated state again later in 2012 (Cutini, 2012), but only reached less than half the peak flux reported for the flare studied here.

At the beginning of the studied interval, the flux is at a level consistent with F_{4FGL}, and during the first two Bayesian blocks, the source's behavior is dominated by strong fluctuations, with the flux changing by factors of > 10 between individual time bins. The peak interval, block 3, is still characterized by fluctuation with the flux dropping and declining rapidly. Conversely, block 4 shows a relatively stable flux, with one major leap near the block center. After the source nearly vanishes (block 5), a second high state occurs in block 6, reaching almost the peak value. Within one bin length, the flux then drops by an order of magnitude, before returning to its violent, fluctuating behavior.

Block 2 contains data points covering a broader spectral range than in the first block,
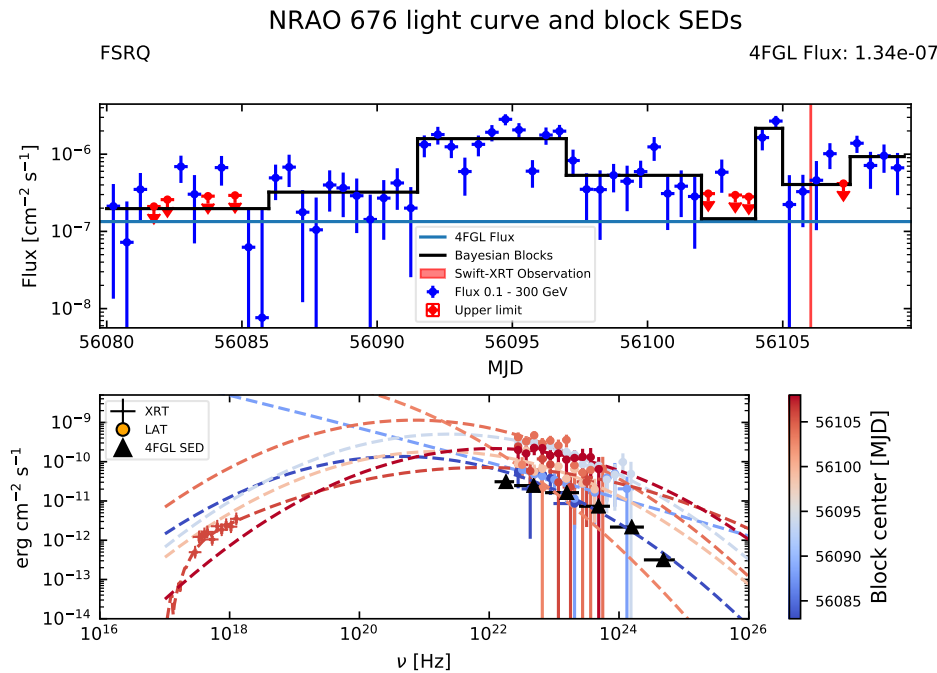
FIGURE 7.29: Top: Daily binned light curve of NRAO 676. Bayesian blocks are shown in black and *Swift* observations are shown as red shaded regions. Bottom: SED of NRAO 676 for each Bayesian block (color bar).

with the SED extending to frequencies up to 10^{24} Hz. The spectral shape in block 2 is best described by a power law, which is in disagreement with results from other blocks. For data sets with only LAT data, this is bound to occur in some cases, as no low-energy data points exist to constrain the lower end of the SED downwards. In block 3, the SED is well constrained over a broad frequency range, its shape consistent with the other well-covered blocks 5,7,8 and 9. The inclusion of XRT data in block 7 primarily influences the SED shape in the X-ray band, with absorption effects leading to a steeper decline.

7.3.23 PKS 2233−148

In Sokolovsky et al., 2010, a previous, dimmer flare from PKS 2233−148 is reported. Pushkarev et al., 2019 studied the radio- and γ-emissions from this blazar between 2009 and 2012, where they find maximum LAT-band fluxes of about 0.4 F.U..

The light curve begins at an elevated state a few times above F_{4FGL}. The flux is generally relatively stable, gently increases over blocks 1 and 2 with a brief drop at the center of block 2. Into block 3, the flux continues to increase slowly and then in blocks 4 and 5 drops rapidly down to its starting point. The flux jumps back up to a high value in block 6 before reaching its peak value in block 7 and declining back to a similar value as in block 6. The final block is characterized by the lowest average flux and some fluctuations a slightly above F_{4FGL}.

The first two blocks with XRT data points show a very consistent spectral behavior. During times of high flux, the SED extends to 10^{25} Hz, and during the peak block (7), the spectrum appears almost flat, with energy fluxes reaching more than two orders of magnitude above the 4FGL-catalog level. The final block also contains

PKS 2233-148 light curve and block SEDs
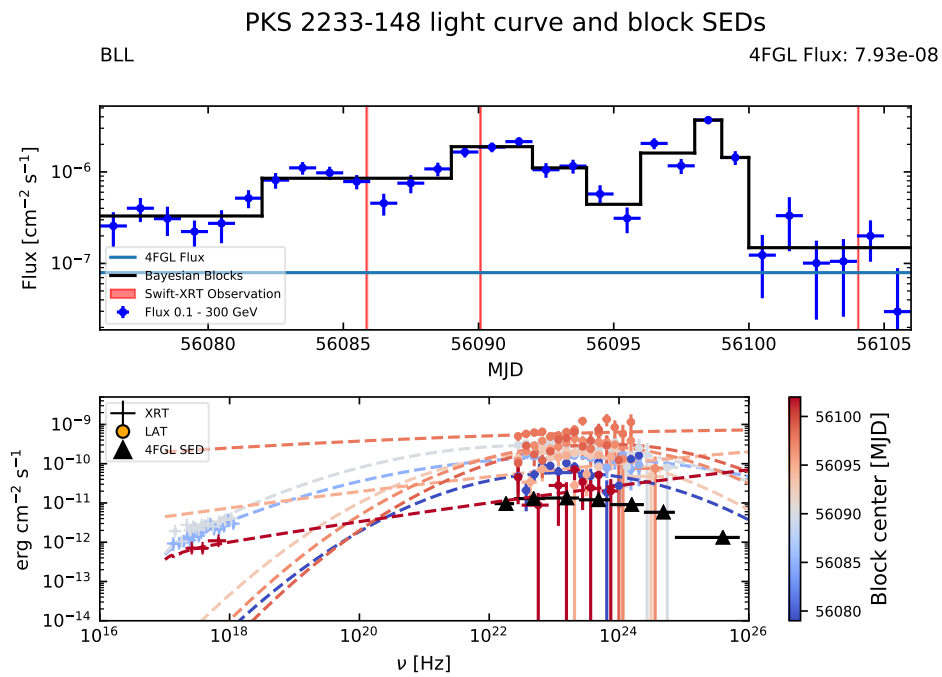
FIGURE 7.30: Top: Daily binned light curve of PKS 2233−148. Bayesian blocks are shown in black and *Swift* observations are shown as red shaded regions. Bottom: SED of PKS 2233−148 for each Bayesian block (color bar).

XRT data, albeit at very low energy flux and with only three spectral bins. The large uncertainties on the corresponding LAT data set do not permit to constrain the SED very well in this period.

Chapter 8

Discussion and Conclusion

8.1 Discussion

8.1.1 Sample selection

The sample of *Fermi*-LAT-detected blazars assembled and studied in this work is mostly comprised of a very particular type of source: Low-synchrotron-peaked − high-luminosity FSRQs. This is consistent with the blazar sequence, which connects high luminosities with low synchrotron peaks from empirical evidence. It's general validity is however disputed within the community (see e.g. Giommi et al., 2012). Using Monte Carlo simulations, it was shown in this work that a sample with such a high fraction of FSRQs, such low synchrotron peaks and such high luminosities is unlikely to be produced by randomly sampling from the 4LAC catalog. The resulting fractions for both distributions depend on how the simulated samples are generated, and increase when source types are taken into account. This shows that the low synchrotron peaks and more-so the high luminosities can to some degree be attributed to the large portion of FSRQs. On the other hand, even though FSRQs typically show lower ν_{syn} values, when assuming that the three BCU are also misidentified FSRQs, not even 1 % out of 100,000 generated samples show an equally extreme synchrotron-peak distribution. However, in contrast to the ν_{syn} distribution, where the applied cut in the MC simulations is obvious (no sources with $\nu_{\mathrm{syn}} > 10^{14}$ Hz), the luminosity distribution is more spread out. Consequently, the choice of the filter criterion (here 19 out of 23 sources with $L > 10^{46}$ erg s^{-1}) heavily impacts the Monte Carlo simulation. For example, the fraction of randomly selected samples where all sources show luminosities greater than 10^{43} erg s^{-1} turns out to be 67.32 %. The two sources with the lowest luminosities are 3C 120 and PKS B1150−108. The comparably low luminosity of the radio galaxy 3C 120 (see e.g. Fig. 7.4) together with the fact that PKS B1150−108 is flagged in 4FGL and the energy flux used to calculate L might thus be underestimated, can explain this difference. It is not the absence of low-luminosity sources in the sample that make the luminosity distribution unusual, but the large fraction of very luminous sources.

Notably, the non-FSRQ sources, with the exception of the radio galaxy 3C 120, are found in a region of the $L − \nu_{\mathrm{syn}}$ diagram dominated by FSRQs. The 3 BL Lac objects have very similar values for both L and ν_{syn}. It should be noted that the number of sources in the sample (original and extended) is relatively small, impacting the significance of the results.

Selecting a sample from *Fermi*-Monitored-Sources-List data comes with the caveat that these data were derived from preliminary analyses and should be interpreted with care. The selection criteria applied here seek to include all blazars with a single bright flare. The somewhat arbitrary flux threshold of 2 F.U. could lead to the exclusion of sources that also show loner-flare behavior, albeit at a lower flux level.

Further, the inclusion of 3C 120, which is not a blazar, shows that the criteria applied to the Monitored Sources List can lead to the inclusion of unexpected sources.

8.1.2 Flare amplitudes

The calculated flare amplitudes, ranging between ~ 30 and ~ 1400, are on average comparable to the full MSL amplitudes. The notable exception, PKS B1150−108, with the highest relative flare amplitude in the full MSL (~ 1400) should be considered with care. As mentioned before (Sec. 4.2), analysis on this source is flagged as potentially inaccurate, so its F_{4FGL} value might be underestimated, in which case the actual flare amplitude wouldn't be as large. The second most intense flare calculated from the Monitored Sources List ($A_{rel} = 1033$) was produced by PKS 0438-43, which is not part of the loner-flare sample. However, similar to PKS B1150-108, PKS 0438-43 is flagged in 4FGL due to its proximity to an unidentified source. This implies that these extreme amplitudes are probably overestimated. The average relative flare amplitude in the loner-flare sample is $A_{mean}^{sample} = 109.2$, whereas the average relative flare amplitude for the full Monitored Sources List is $A_{mean}^{MSL} = 58.0$. When excluding the exceedingly high amplitude of PKS B1150-180 from the sample-mean calculation, this becomes: $A_{mean_{corr}}^{sample} = 50.3$, with a standard deviation of 20.5. Also excluding all amplitudes > 1000 from the full MSL, the new mean becomes: $A_{mean_{corr}}^{MSL} = 43.7$ with a standard deviation of 72.2. While this average amplitude from the loner-flare sample is not significantly larger than that from the full MSL, the resulting standard deviations differ by a factor of more than 3. This could imply that loner flares tend to occupy a particular region in amplitude space, however the small number of data points does not allow a firm conclusion on this.

8.1.3 Light curves and spectral evolution

Analysis of the light curves and corresponding spectra has shown that even though loner flares come from similar types of objects, they still show different behavior during their flares. While most light curves begin and end at an elevated state at a few times the 4FGL flux, some start out at the catalog level. In some cases, like PMN J0017−0512, the beginning of the light curve is characterized by low-statistics data points with low fluxes and/or large errors. This behavior reflects that before the flare, PMN J0017−0512 never appeared on the Monitored Sources List because it had been in a low state. Some sources show violent variability on the shortest timescales, with doubling times shorter than the bin size (e.g. S4 1849+67, B2 1846+32A). The measured peak fluxes are all in the range between 0.87 F.U. (3C 120) and 3.7 F.U. (PKS 2233−148). 13 out of 23 sources do not reach the initial threshold of 2 F.U.. In addition to the preliminary nature of MSL data, the chosen binning plays a role in the flux calculation. The Monitored Sources List uses one-day bins by default, while in this work the bin size is chosen individually. The range of peak fluxes is quite narrow, and about an order of magnitude below the fluxes measured in the 40 brightest flares recorded (Nalewajko, 2013). The shapes of the resulting light curves vary from a very pronounced, single rise and fall (e.g. OT 081) to a more intricate behavior with multiple sub-flares (e.g. PKS 2233−148, GB 1310+487). This is most pronounced in B2 0218−357, but can in this case primarily be attributed to gravitational lensing. A way to compare such different flares to one another is to compare the number of Bayesian blocks in each light curve as a measure of smoothness. However, the bin size has an impact on the calculation of the block, as smaller time bins tend to lead

to larger error bars. The smallest number of blocks obtained is 3 (4 sources), while the largest is 13 (1 source).

Low statistics (and thus low flux) data points, can, in combination with Bayesian-block analysis lead to an unfavorable division of the light curve (e.g. 4C +14.23). As these low-TS data points often have unrealistically small errors, this can lead to falsely identified blocks. The occurrence of low-TS time bins can be mitigated to some degree by increasing the bin size from e.g. 12 h to 2 d, but at the same time this decreases time resolution, making it more likely that short-lived features are missed. Another way to tackle this problem could be to apply adaptive-binning methods, where instead of a fixed duration, bins are created so that each has a certain minimum test statistic.

The spectral evolution ties higher energy fluxes and higher cutoff energies to higher fluxes. During the peak flux, the SEDs shift upwards and tend to flatten. In a number of sources, a few of the resulting SEDs appear to disagree with the ones from the rest of the light curve, e.g. the first block in PMN J0017−0512. During this particular block, the large number of upper limits in the light curve and the resulting low average flux imply that the source is in a fluctuating low state. This makes it difficult to extract reliable spectral information.

Adapting the spectral binning by adding spectral bins until a TS threshold of 1 is reached increases the reliability of each resulting data point, at the cost of a smaller number of data points. Using available XRT data allows constraining the SED much better, but even the LAT-only data sets mostly support the log-parabolic model. However, a number of LAT-only blocks show an SED that diverges towards lower frequencies. This occurs mostly in short-duration or low-flux blocks where the small number of well-constrained data points doesn't allow for a reliable fit anyway. In contrast, for example the peak block in B2 0552+39A shows a diverging spectrum which is in strong disagreement with the X-ray data from the subsequent block, even though the LAT SED is fairly well constrained. As no information about the X-ray flux is included where no simultaneous XRT data exist, fits where only LAT data were used do not necessarily reflect the source's real X-ray behavior. Because this work is primarily focused on studying LAT-band data and no further computations are performed with the SED-fit results, this effect can be considered harmless and this thesis does not claim to produce LAT-band fits that can be reasonably extrapolated into the X-ray regime. In some cases, individual light curve blocks contain more upper limits than high-confidence data points. Where only LAT data were available, it proved useful to constrain the fit manually by fixing either only α or α and β to their respective 4FGL values. This allows obtaining an energy flux estimate to compare the results from other blocks to while making educated assumptions about the spectrum.

In many cases, *Swift* follow-up observations only happen days after the flux peak. However, these additional data are instrumental in constraining the spectrum. Studying LAT and XRT bands simultaneously allows to investigate how well-correlated X-ray and γ-ray emission states are. In the case of 4C +49.22, the source appears to be in different X-ray states during the two XRT observations, reflecting the behavior of the γ-ray band that change in the same way between the observation times. A similar behavior is seen in S4 0954+65, where higher γ-ray states are accompanied by high X-ray states. However, statistically constant flux in the LAT band does not necessarily imply the same behaviour in the XRT band, and when multiple *Swift* observations fall within the same Bayesian block, this could pose a problem. Comparing the XRT count rates from these single observations is a simple way to see whether individual observations are comparable. If these data sets are found to be

comparable according to a good metric, they can be readily combined, but for this, one needs to find a good metric first. In this work, it was investigated whether any two given count rates within a single Bayesian block are consistent within the measurement uncertainties. All but two pairs of observations pass this test. In the case of OT 081, where the count rate from one observation does not agree with two others, the discrepancy is still minuscule and the resulting spectral evolution is also consistent with X-ray and γ-states being correlated. Yet, small variations in the X-ray count rate could still be related to large differences in the spectrum. This is offset to some degree by the fact that the XRT covers a much smaller portion of the electromagnetic spectrum than the LAT. But a more robust way to compare XRT observations would include a comparison in the distribution of counts along the energy axis, for example by dividing into soft ($0.5 - 2$ keV) and hard (> 2 keV) counts.

8.2 Conclusion

By studying a sample of loner-flare blazars detected by the *Fermi*-LAT, strong indications that there are unifying characteristics tying together these sources arise. In this work, it was shown that loner flares are more likely to occur in FSRQ sources, and generally in sources with large intrinsic luminosities and low synchrotron peaks. Selecting a sample with a lower flux threshold produces a collection of sources with similar properties. This shows that the observed characteristics in the original sample are not purely a selection effect as they are independent of the flux threshold.

This, together with the computed flare amplitudes, indicates that loner flares are not so much defined by the flares themselves, but much rather by the source type they arise in. No indications are found that loner flares are more extreme than their well-studied counterparts, i.e. exhibiting larger-than-usual deviations from the catalogued flux value, besides the case of PKS B1150−108 where the reliability of the catalogued γ-ray flux can be disputed. Loner flares are characterized by their source's low duty-cycle, and a number of sources in the sample only showed up in *Fermi* catalogs after their flares. Thus, there could be a large number of blazars with low synchrotron peaks at possibly large redshifts that have never been observed in the gamma-rays because they haven't flared in the past 10 years. This is amplified by the short duration of the *Fermi* mission compared to conceivable duty cycles in such sources. While this work cannot present a set of trigger mechanisms responsible for such flares, it provides information on where to look for isolated flaring events in the future.

In order to study the spectral evolution of sources during a flare, availability of synchronous multiwavelength observations is beneficial. Where XRT data are available, this allows further constraining the shape of the inverse Compton hump in the SED. When multiple XRT observations were taken during one LAT light curve, the energy fluxes of the two bands appear correlated. For future research, including data sets from more instruments will prove to be conducive. In addition to XRT, the other instruments on-board the *Swift* satellite (i.e. UVOT and BAT) can be used, as *Swift* often performs follow-up observations on LAT detected gamma-ray flares. For sources at low-enough redshifts, VHE data taken by one or more of the various Imaging Air Cherenkov Telescopes (IACTs) could add valuable information to better constrain the declining flank of the inverse Compton hump. As these loner-flaring blazars tend to be low-synchrotron-peaked sources, most of the IC hump can be covered

by using instruments spanning the soft X-ray to soft TeV bands. Monitoring programs like that exist, but strongly favor more popular sources that show repeated activity. A number of questions remain open for future studies, among them the exact influence of the sample selection criteria on the properties of the final sample, the puzzling inclusion of 3C 120 and ways to avoid artifacts of the Bayesian blocks algorithm while keeping a decent time resolution.

Appendix A

Appendix A: ATel #13533

Fermi LAT Detection of the brightest gamma-ray flare from PKS 1156-221

ATel #13533; *J. Sinapius (Univ. of Wuerzburg) and R. Ojha (NASA/GSFC/UMBC) on behalf of the Fermi-LAT Collaboration*
on 28 Feb 2020; 23:10 UT
Credential Certification: Roopesh Ojha (Roopesh.Ojha@gmail.com)

Subjects: Gamma Ray, >GeV, AGN, Blazar, Quasar

The Large Area Telescope (LAT), one of the two instruments on the Fermi Gamma-ray Space Telescope, has observed a gamma-ray flare from a source positionally consistent with the quasar PKS 1156-221, associated with the gamma-ray source 4FGL J1159.2-2227 (The Fermi-LAT collaboration 2019, arXiv:1902.10045) at RA = 11h59m11.2672s, Dec = -22d28m36.902s (J2000, Beasley et al. 2002 ApJS, 141, 13). This source has a measured redshift of $z = 0.565$ (Wright et al. 1979, ApJ 229, 73).

Preliminary analysis indicates that on 2020 February 27, PKS 1156-221 reached a daily averaged gamma-ray flux (E>100MeV) of $(1.4+/-0.2) \times 10^{-6}$ photons cm^-2 s^-1 (statistical uncertainty only). This corresponds to a flux increase of a factor of about 80 relative to the average flux reported in the fourth Fermi-LAT catalog (4FGL). The corresponding photon index is 2.1+/-0.1, significantly smaller than the 4FGL value of 2.4+/-0.1.

Because Fermi normally operates in an all-sky scanning mode, regular gamma-ray monitoring of this source will continue and the daily and weekly automated flux values will be added to the Monitored Source List, https://fermi.gsfc.nasa.gov/ssc/data/access/lat/msl_lc/. We encourage multifrequency observations of this source. For this source, the Fermi-LAT contact person is Jonas Sinapius (jonas.sinapius@stud-mail.uni-wuerzburg.de).

The Fermi-LAT is a pair conversion telescope designed to cover the energy band from 20 MeV to greater than 300 GeV. It is the product of an international collaboration between NASA and DOE in the U.S. and many scientific institutions across France, Italy, Japan and Sweden.

Appendix B

Appendix B: Daily *Fermi*-MSL light curves for all sample sources
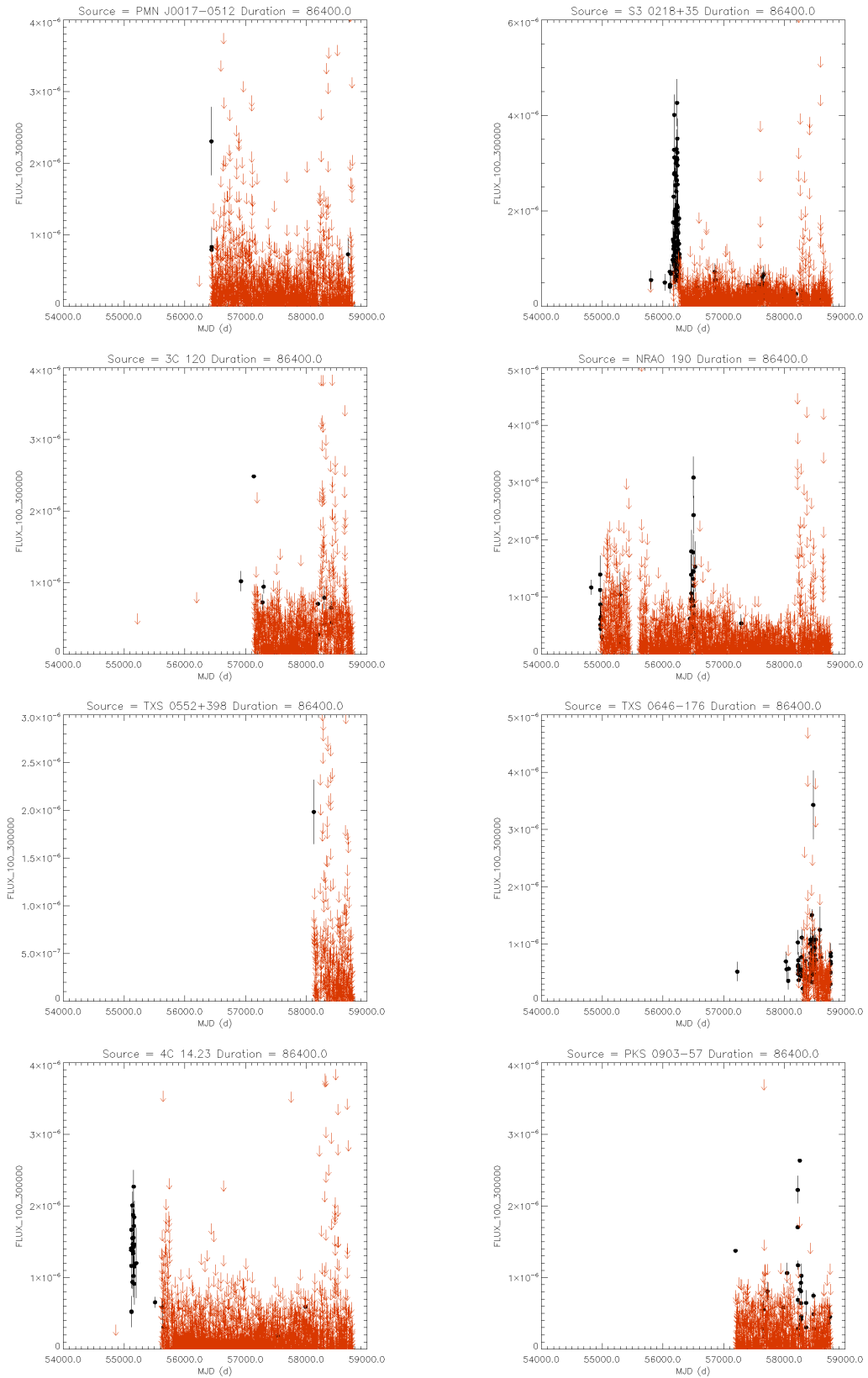
FIGURE B.1: *Fermi*-MSL daily-binned light curves for all sample sources, retrieved Oct. 7, 2019. The y-axis shows the flux between 100 MeV and 300 GeV in photons $cm^{-2} s^{-1}$. Upper limits are shown in red.

FIGURE B.1: (cont.) *Fermi*-MSL daily-binned light curves for all sample sources, retrieved Oct. 7, 2019. The y-axis shows the flux between 100 MeV and 300 GeV in photons cm^{-2} s^{-1}. Upper limits are shown in red.
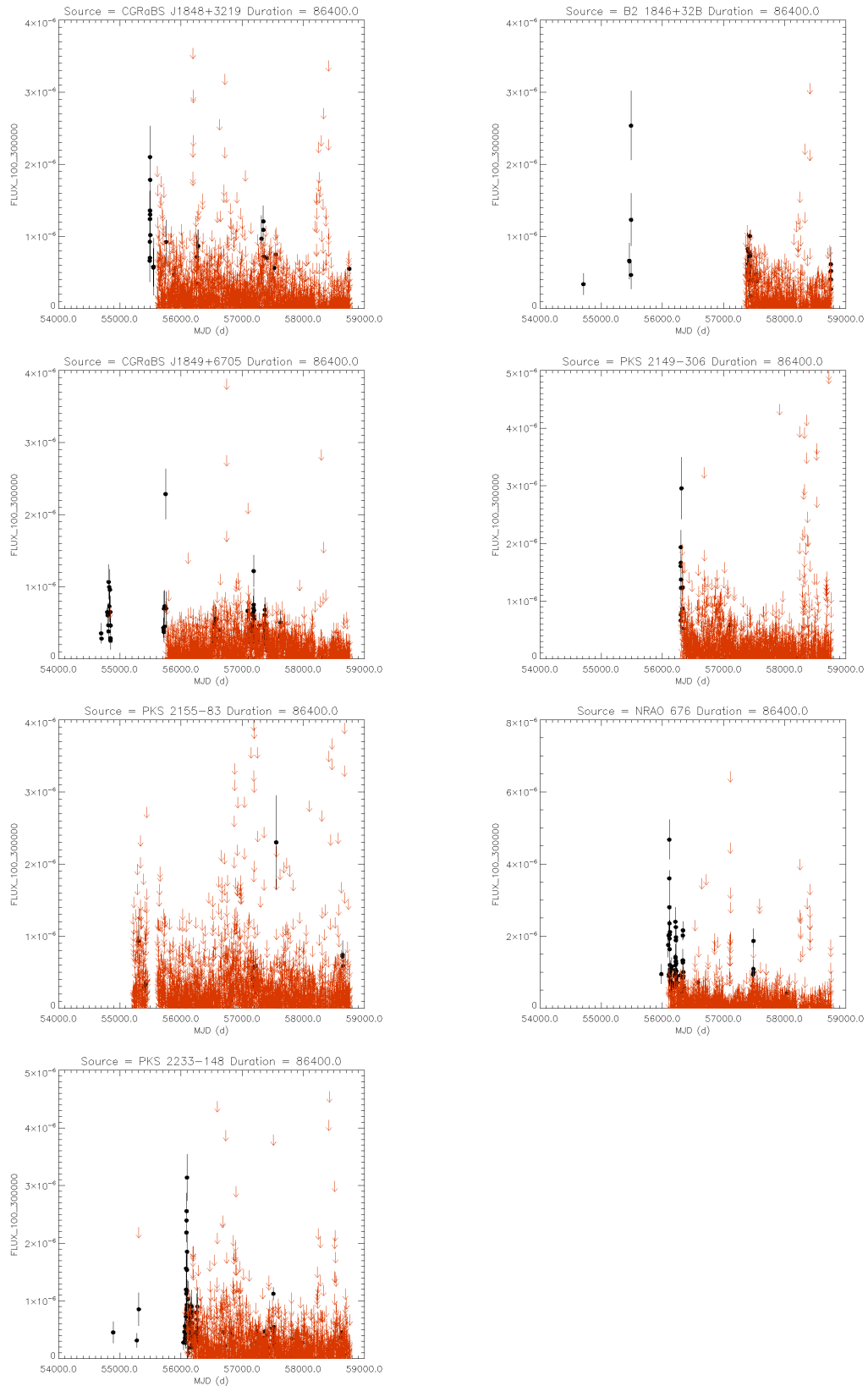
FIGURE B.1: (cont.) *Fermi*-MSL daily-binned light curves for all sample sources, retrieved Oct. 7, 2019. The y-axis shows the flux between 100 MeV and 300 GeV in photons $cm^{-2} s^{-1}$. Upper limits are shown in red.

Appendix C

Appendix C: Observations and fit parameters

Source Name	Block limits [MJD]	χ^2_{red}	DOF	α	β	Normalization	n_H [$10^{20}[cm]^{-2}$]
PMN J0017-0512	56423..56435	0.7	1	$2.6^{\dagger}$	$0.141^{0.11}_{0.046}$	$\left(0.65^{42.0}_{0.61}\right) \times 10^{-6}$	-
PMN J0017-0512	56448..56452	0.4	5	$2.31^{0.86}_{1.6}$	$\left(5000.0^{140000.0}_{0.12}\right) \times 10^{-6}$	$\left(0.06^{5.6}_{0.06}\right) \times 10^{-6}$	-
PMN J0017-0512	56435..56448	0.9	13	$1.4^{0.94}_{0.17}$	$\left(149.82^{0.18}_{140.0}\right) \times 10^{-3}$	$\left(0.008^{0.21}_{0.0052}\right) \times 10^{-6}$	-
B2 0218+357	56196..56204	2.0	16	$1.388^{0.15}_{0.045}$	$\left(150000.0^{0.17}_{26000.0}\right) \times 10^{-6}$	$\left(0.052^{0.033}_{0.012}\right) \times 10^{-6}$	-
B2 0218+357	56193..56195	0.5	11	$1.597^{0.037}_{0.034}$	$0.077^{0.06}_{0.055}$	$\left(0.0093^{0.38}_{0.0036}\right) \times 10^{-6}$	$\left(64000.0^{64000.0}_{0.2}\right) \times 10^{-6}$
B2 0218+357	56188..56193	0.7	14	$1.285^{0.38}_{0.081}$	$\left(149.99^{0.014}_{67.0}\right) \times 10^{-3}$	$\left(0.028^{0.068}_{0.011}\right) \times 10^{-6}$	-
B2 0218+357	56185..56188	2.0	16	$1.439^{0.016}_{0.018}$	$0.13^{0.014}_{0.013}$	$\left(0.081^{0.021}_{0.016}\right) \times 10^{-6}$	$\left(64.0^{64.0}_{0.009}\right) \times 10^{-3}$
B2 0218+357	56195..56196	2.0	11	$1.46^{0.9}_{0.19}$	$\left(150.0^{0.0015}_{140.0}\right) \times 10^{-3}$	$\left(0.028^{0.55}_{0.02}\right) \times 10^{-6}$	-
B2 0218+357	56161..56164	0.8	9	$1.57^{0.75}_{0.65}$	$0.087^{0.063}_{0.082}$	$\left(0.011^{0.25}_{0.01}\right) \times 10^{-6}$	-
B2 0218+357	56164..56167	1.0	12	$1.39^{0.92}_{0.15}$	$\left(149.82^{0.18}_{140.0}\right) \times 10^{-3}$	$\left(0.032^{0.73}_{0.019}\right) \times 10^{-6}$	-
B2 0218+357	56184..56185	0.4	9	$1.6^{1.1}_{0.28}$	$\left(150000.0^{0.013}_{140000.0}\right) \times 10^{-6}$	$\left(0.12^{6.3}_{0.096}\right) \times 10^{-6}$	-
B2 0218+357	56167..56173	1.0	16	$1.643^{0.032}_{0.023}$	$0.103^{0.037}_{0.048}$	$\left(0.013^{0.011}_{0.0065}\right) \times 10^{-6}$	$\left(63800.0^{64000.0}_{0.75}\right) \times 10^{-6}$
B2 0218+357	56181..56184	0.4	6	$2.36^{0.67}_{1.3}$	$\left(5.0^{140.0}_{0.0012}\right) \times 10^{-3}$	$\left(0.18^{6.6}_{0.18}\right) \times 10^{-6}$	-
B2 0218+357	56158..56161	1e-32	-1	$2.3^{\dagger}$	$0.005^{0.14}_{0.0}$	$\left(0.0066^{0.43}_{0.0066}\right) \times 10^{-6}$	-
B2 0218+357	56145..56158	0.6	11	$2.2^{0.28}_{0.97}$	$\left(5000.0^{140000.0}_{0.065}\right) \times 10^{-6}$	$\left(0.08^{0.34}_{0.077}\right) \times 10^{-6}$	-
B2 0218+357	56173..56181	2.0	20	$1.505^{0.014}_{0.016}$	$0.122^{0.015}_{0.014}$	$\left(0.04^{0.011}_{0.0087}\right) \times 10^{-6}$	$\left(63.83^{64.0}_{0.035}\right) \times 10^{-3}$
3C 120	56910..56921	1.0	2	$2.5^{\dagger}$	$0.005^{0.14}_{0.0}$	$\left(0.032^{0.84}_{0.032}\right) \times 10^{-6}$	-
3C 120	56929..56938	0.8	3	$2.5^{\dagger}$	$0.059^{0.09}_{0.037}$	$\left(0.37^{1.3}_{0.31}\right) \times 10^{-6}$	-
3C 120	56921..56929	2.0	7	$2.34^{0.44}_{1.1}$	$0.0135^{0.14}_{0.0085}$	$\left(0.22^{2.0}_{0.22}\right) \times 10^{-6}$	-
PKS 0440-00	56472..56478	0.7	6	$1.96^{1.3}_{0.53}$	$0.1487^{0.0013}_{0.14}$	$\left(0.12^{21.0}_{0.11}\right) \times 10^{-6}$	-
PKS 0440-00	56450..56465	0.4	11	$1.24^{1.0}_{0.19}$	$\left(150.0^{0.0017}_{140.0}\right) \times 10^{-3}$	$\left(0.0029^{0.12}_{0.0021}\right) \times 10^{-6}$	-
PKS 0440-00	56465..56468	0.6	14	$1.61^{0.58}_{0.53}$	$0.083^{0.067}_{0.078}$	$\left(0.046^{0.38}_{0.041}\right) \times 10^{-6}$	-
PKS 0440-00	56468..56472	0.9	10	$1.33^{0.94}_{0.2}$	$\left(150000.0^{0.86}_{140000.0}\right) \times 10^{-6}$	$\left(0.01^{0.26}_{0.0076}\right) \times 10^{-6}$	-
B2 0552+39A	58133..58138	0.05	1	$2.6^{\dagger}$	$0.2^{\dagger}$	$\left(0.0034^{0.0035}_{0.0034}\right) \times 10^{-3}$	-
B2 0552+39A	58125..58133	0.8	18	$1.705^{0.032}_{0.025}$	$0.06^{0.039}_{0.04}$	$\left(0.01^{0.38}_{0.0033}\right) \times 10^{-6}$	$\left(269000.0^{77000.0}_{0.0087}\right) \times 10^{-6}$
B2 0552+39A	58122..58125	0.4	12	$2.13^{0.2}_{0.95}$	$\left(5.59^{140.0}_{0.59}\right) \times 10^{-3}$	$\left(0.25^{0.52}_{0.24}\right) \times 10^{-6}$	-
B2 0552+39A	58116..58122	0.2	5	$1.49^{1.3}_{0.55}$	$\left(150.0^{0.0022}_{140.0}\right) \times 10^{-3}$	$\left(0.0075^{1.7}_{0.0073}\right) \times 10^{-6}$	-
B2 0552+39A	58109..58116	4e-09	-1	$2.5^{1.5}_{2.0}$	$\left(5.09^{140.0}_{0.093}\right) \times 10^{-3}$	$\left(0.052^{1100.0}_{0.052}\right) \times 10^{-6}$	-
TXS 0646-176	58482..58487	0.7	7	$1.29^{0.99}_{0.26}$	$\left(149.97^{0.031}_{140.0}\right) \times 10^{-3}$	$\left(0.0067^{0.23}_{0.0055}\right) \times 10^{-6}$	-
TXS 0646-176	58474..58475	0.1	1	$1.9^{2.1}_{1.4}$	$0.1413^{0.0087}_{0.14}$	$\left(0.83^{20000.0}_{0.83}\right) \times 10^{-6}$	-
TXS 0646-176	58477..58482	0.4	10	$1.88^{0.62}_{0.075}$	$0.056^{0.094}_{0.051}$	$\left(5700.0^{370000.0}_{5e-06}\right) \times 10^{-12}$	$\left(474000.0^{0.45}_{240000.0}\right) \times 10^{-6}$
TXS 0646-176	58471..58474	1.0	2	$1.82^{1.5}_{0.68}$	$\left(150.0^{0.0011}_{140.0}\right) \times 10^{-3}$	$\left(0.11^{50.0}_{0.11}\right) \times 10^{-6}$	-
TXS 0646-176	58461..58471	0.2	7	$1.53^{1.1}_{0.28}$	$\left(149.06^{0.94}_{140.0}\right) \times 10^{-3}$	$\left(0.023^{1.3}_{0.019}\right) \times 10^{-6}$	-
TXS 0646-176	58475..58477	1.0	16	$1.696^{0.067}_{0.04}$	$\left(5.0^{39.0}_{0.0032}\right) \times 10^{-3}$	$\left(0.0076^{0.0056}_{0.0024}\right) \times 10^{-6}$	$0.33^{0.15}_{0.09}$
TXS 0646-176	58460..58461	0.3	6	$1.37^{1.2}_{0.44}$	$\left(150000.0^{0.99}_{140000.0}\right) \times 10^{-6}$	$\left(0.018^{2.3}_{0.017}\right) \times 10^{-6}$	-
TXS 0646-176	58487..58490	0.0	-1	$2.5^{\dagger}$	$0.05^{0.45}_{0.055}$	$\left(0.056^{32.0}_{0.056}\right) \times 10^{-6}$	-
4C +14.23	55124..55130	0.2	7	$1.54^{1.2}_{0.34}$	$\left(150000.0^{0.085}_{140000.0}\right) \times 10^{-6}$	$\left(0.011^{0.91}_{0.0095}\right) \times 10^{-6}$	-
4C +14.23	55130..55132	1.0	1	$1.35^{2.3}_{0.85}$	$\left(150.0^{0.0011}_{140.0}\right) \times 10^{-3}$	$\left(0.0028^{71.0}_{0.0028}\right) \times 10^{-6}$	-
4C +14.23	55104..55114	0.6	6	$1.5^{1.1}_{0.32}$	$\left(150.0^{0.006}_{140.0}\right) \times 10^{-3}$	$\left(0.0086^{0.72}_{0.0076}\right) \times 10^{-6}$	-
4C +14.23	55114..55115	0.0	0				
4C +14.23	55115..55124	1.0	21	$1.524^{0.015}_{0.016}$	$0.079^{0.015}_{0.014}$	$\left(0.018^{0.0052}_{0.0041}\right) \times 10^{-6}$	$\left(72.91^{46.0}_{0.0083}\right) \times 10^{-3}$
PKS 0903-57	58253..58254	1.0	7	$1.35^{1.1}_{0.26}$	$\left(149.87^{0.13}_{140.0}\right) \times 10^{-3}$	$\left(0.018^{0.9}_{0.014}\right) \times 10^{-6}$	-
PKS 0903-57	58251..58252	3.0	1	$2.3^{\dagger}$	$0.005^{0.49}_{0.0}$	$\left(0.31^{88.0}_{0.31}\right) \times 10^{-6}$	-
PKS 0903-57	58252..58253	2.0	12	$1.27^{0.39}_{0.11}$	$\left(150000.0^{0.011}_{67000.0}\right) \times 10^{-6}$	$\left(0.032^{0.085}_{0.016}\right) \times 10^{-6}$	-
PKS 0903-57	58254..58263	0.6	30	$1.758^{0.027}_{0.02}$	$0.073^{0.026}_{0.032}$	$\left(0.014^{0.0077}_{0.0042}\right) \times 10^{-6}$	$\left(260000.0^{120000.0}_{0.69}\right) \times 10^{-6}$
PKS 0906+01	55302..55309	0.7	8	$1.44^{0.99}_{0.26}$	$\left(150.0^{0.0016}_{140.0}\right) \times 10^{-3}$	$\left(0.0058^{0.2}_{0.0048}\right) \times 10^{-6}$	-

PKS 0906+01	55301..55302	0.0	0				
PKS 0906+01	55294..55295	0.9	8	$1.83^{1.0}_{0.76}$	$0.103^{0.047}_{0.098}$	$\left(0.13^{7.9}_{0.12}\right) \times 10^{-6}$	-
PKS 0906+01	55280..55294	1.0	2	$2.5^{\dagger}$	$0.045^{0.1}_{0.04}$	$\left(0.14^{0.77}_{0.12}\right) \times 10^{-6}$	-
PKS 0906+01	55295..55301	0.3	6	$2.48^{0.68}_{1.3}$	$\left(5.0^{140.0}_{0.0021}\right) \times 10^{-3}$	$\left(0.28^{10.0}_{0.27}\right) \times 10^{-6}$	-
S4 0954+65	56976..56977	3.0	7	$1.4^{1.1}_{0.29}$	$\left(150000.0^{0.18}_{140000.0}\right) \times 10^{-6}$	$\left(0.02^{1.2}_{0.017}\right) \times 10^{-6}$	-
S4 0954+65	56981..56990	1.0	25	$1.859^{0.089}_{0.045}$	$\left(5000.0^{23000.0}_{0.8}\right) \times 10^{-6}$	$\left(0.0031^{0.0015}_{0.0012}\right) \times 10^{-6}$	$\left(93600.0^{0.99}_{38000.0}\right) \times 10^{-6}$
S4 0954+65	56978..56981	1.0	42	$1.751^{0.017}_{0.016}$	$0.094^{0.024}_{0.017}$	$\left(0.056^{0.024}_{0.014}\right) \times 10^{-6}$	$\left(93.5^{0.099}_{47.0}\right) \times 10^{-3}$
S4 0954+65	56962..56976	0.2	3	$2.67^{0.81}_{1.3}$	$\left(5.32^{140.0}_{0.32}\right) \times 10^{-3}$	$\left(0.28^{18.0}_{0.28}\right) \times 10^{-6}$	-
S4 0954+65	56977..56978	0.3	1	$2.2^{\dagger}$	$\left(5.14^{130.0}_{0.14}\right) \times 10^{-3}$	$\left(0.025^{9.9}_{0.02}\right) \times 10^{-6}$	-
PKS B1150-108	58432..58435	1e-07	-1	$3.12^{0.88}_{2.6}$	$0.1453^{0.0047}_{0.14}$	$\left(0.062^{7.1}_{0.062}\right) \times 10^{-3}$	-
PKS B1150-108	58435..58439	0.5	1	$1.603^{0.14}_{0.082}$	$0.021^{0.13}_{0.016}$	$\left(0.92^{380.0}_{0.64}\right) \times 10^{-9}$	$0.04^{0.013}_{0.013}$
PKS B1150-108	58429..58432	5e-08	-2	$3.0^{1.0}_{2.5}$	$0.029^{0.12}_{0.024}$	$\left(0.72^{2900.0}_{0.72}\right) \times 10^{-6}$	-
4C +49.22	55678..55684	0.8	39	$1.794^{0.029}_{0.022}$	$0.06^{0.021}_{0.021}$	$\left(0.013^{0.0057}_{0.0041}\right) \times 10^{-6}$	-
4C +49.22	55675..55678	2.0	58	$1.746^{0.018}_{0.025}$	$0.0077^{0.021}_{0.01}$	$\left(0.0097^{0.006}_{0.0021}\right) \times 10^{-6}$	-
4C +49.22	55686..55689	0.5	7	$1.68^{0.93}_{0.52}$	$0.114^{0.036}_{0.11}$	$\left(0.024^{0.91}_{0.023}\right) \times 10^{-6}$	-
4C +49.22	55672..55675	0.9	7	$1.94^{0.51}_{1.4}$	$\left(5.0^{140.0}_{0.001}\right) \times 10^{-3}$	$\left(0.016^{0.28}_{0.016}\right) \times 10^{-6}$	-
4C +49.22	55684..55686	1.0	1	$2.4^{\dagger}$	$0.044^{\dagger}$	$\left(0.028^{0.037}_{0.028}\right) \times 10^{-6}$	-
4C +49.22	55661..55672	0.3	5	$2.28^{0.76}_{1.4}$	$\left(5.03^{140.0}_{0.025}\right) \times 10^{-3}$	$\left(0.055^{3.2}_{0.055}\right) \times 10^{-6}$	-
GB 1310+487	55179..55196	0.8	16	$0.91^{0.93}_{0.13}$	$\left(149.85^{0.15}_{140.0}\right) \times 10^{-3}$	$\left(0.3^{7.9}_{0.18}\right) \times 10^{-9}$	-
GB 1310+487	55173..55179	0.9	4	$0.79^{1.2}_{0.29}$	$\left(150000.0^{0.21}_{140000.0}\right) \times 10^{-6}$	$\left(0.039^{4.9}_{0.036}\right) \times 10^{-9}$	-
GB 1310+487	55153..55155	2.0	9	$1.93^{0.38}_{1.0}$	$\left(5.01^{140.0}_{0.0061}\right) \times 10^{-3}$	$\left(0.04^{0.31}_{0.039}\right) \times 10^{-6}$	-
GB 1310+487	55139..55153	0.5	9	$1.7^{0.95}_{0.55}$	$0.111^{0.039}_{0.11}$	$\left(0.0078^{0.37}_{0.0074}\right) \times 10^{-6}$	-
GB 1310+487	55155..55157	0.8	13	$1.79^{0.15}_{0.84}$	$\left(5.0^{140.0}_{0.0019}\right) \times 10^{-3}$	$\left(0.041^{0.063}_{0.038}\right) \times 10^{-6}$	-
GB 1310+487	55158..55160	0.7	14	$0.99^{0.94}_{0.17}$	$\left(149.98^{0.019}_{140.0}\right) \times 10^{-3}$	$\left(0.0017^{0.044}_{0.0012}\right) \times 10^{-6}$	-
GB 1310+487	55157..55158	0.7	15	$0.94^{0.77}_{0.11}$	$\left(150.0^{0.0044}_{130.0}\right) \times 10^{-3}$	$\left(0.0043^{0.054}_{0.0023}\right) \times 10^{-6}$	-
GB 1310+487	55160..55164	1.0	22	$1.464^{0.014}_{0.015}$	$0.083^{0.013}_{0.012}$	$\left(0.025^{0.0061}_{0.0047}\right) \times 10^{-6}$	$\left(19.23^{0.0072}_{9.6}\right) \times 10^{-3}$
GB 1310+487	55196..55198	0.001	-1	$2.2^{1.8}_{1.7}$	$\left(5.0^{140.0}_{0.0032}\right) \times 10^{-3}$	$\left(0.0092^{800.0}_{0.0092}\right) \times 10^{-6}$	-
GB 1310+487	55168..55173	2.0	7	$1.4^{1.3}_{0.38}$	$\left(150000.0^{0.11}_{140000.0}\right) \times 10^{-6}$	$\left(0.0035^{0.51}_{0.0032}\right) \times 10^{-6}$	-
GB 1310+487	55164..55168	1.0	16	$1.522^{0.023}_{0.025}$	$0.056^{0.021}_{0.019}$	$\left(0.0084^{0.0035}_{0.0025}\right) \times 10^{-6}$	$\left(9.63^{9.6}_{0.012}\right) \times 10^{-3}$
PKS 1454-354	54714..54715	4.0	1	$\left(500000.0^{560000.0}_{0.66}\right) \times 10^{-6}$	$\left(5.02^{110.0}_{0.017}\right) \times 10^{-3}$	$\left(0.01^{0.25}_{0.0053}\right) \times 10^{-9}$	-
PKS 1454-354	54710..54713	0.4	10	$1.04^{1.2}_{0.38}$	$\left(150000.0^{0.43}_{140000.0}\right) \times 10^{-6}$	$\left(0.92^{96.0}_{0.86}\right) \times 10^{-9}$	-
PKS 1454-354	54709..54710	0.9	2	$2.0^{1.2}_{1.5}$	$\left(5.0^{140.0}_{0.0013}\right) \times 10^{-3}$	$\left(0.017^{8.9}_{0.017}\right) \times 10^{-6}$	-
PKS 1454-354	54713..54714	1.0	13	$1.05^{0.36}_{0.1}$	$\left(150.0^{0.0037}_{62.0}\right) \times 10^{-3}$	$\left(0.0094^{0.023}_{0.0046}\right) \times 10^{-6}$	-
PKS 1454-354	54706..54709	0.6	10	$1.99^{0.36}_{1.1}$	$\left(5.16^{140.0}_{0.16}\right) \times 10^{-3}$	$\left(0.03^{0.22}_{0.03}\right) \times 10^{-6}$	-
PKS 1454-354	54718..54720	1.0	5	$2.4^{1.5}_{1.5}$	$\left(5000.0^{140000.0}_{0.99}\right) \times 10^{-6}$	$\left(0.32^{820.0}_{0.32}\right) \times 10^{-6}$	-
PKS 1454-354	54715..54718	1.0	5	$1.73^{0.05}_{0.04}$	$0.021^{0.081}_{0.016}$	$\left(0.005^{0.0044}_{0.0022}\right) \times 10^{-6}$	$\left(117.99^{0.012}_{59.0}\right) \times 10^{-3}$
B2 1504+37	56990..56993	0.5	9	$1.32^{0.97}_{0.21}$	$\left(150000.0^{0.095}_{140000.0}\right) \times 10^{-6}$	$\left(0.0059^{0.18}_{0.0043}\right) \times 10^{-6}$	-
B2 1504+37	56989..56990	1.0	1	$3.02^{0.98}_{2.5}$	$\left(150000.0^{0.0018}_{140000.0}\right) \times 10^{-6}$	$\left(0.0163^{3.5}_{0.016}\right) \times 10^{-3}$	-
B2 1504+37	56987..56989	0.9	10	$1.18^{0.83}_{0.16}$	$\left(150000.0^{0.24}_{140000.0}\right) \times 10^{-6}$	$\left(0.0043^{0.06}_{0.0028}\right) \times 10^{-6}$	-
B2 1504+37	56979..56986	1.0	10	$1.67^{0.67}_{0.57}$	$0.086^{0.064}_{0.081}$	$\left(0.011^{0.15}_{0.01}\right) \times 10^{-6}$	-
B2 1504+37	56986..56987	0.4	12	$1.38^{0.94}_{0.17}$	$\left(150.0^{0.0012}_{140.0}\right) \times 10^{-3}$	$\left(0.024^{0.62}_{0.016}\right) \times 10^{-6}$	-
OT 081	57588..57590	1.0	47	$1.6193^{0.008}_{0.0079}$	$0.0584^{0.008}_{0.0083}$	$\left(0.077^{0.013}_{0.011}\right) \times 10^{-6}$	$\left(99.91^{33.0}_{0.0077}\right) \times 10^{-3}$
OT 081	57596..57603	0.9	22	$1.728^{0.026}_{0.021}$	$0.033^{0.03}_{0.028}$	$\left(0.011^{0.0072}_{0.0035}\right) \times 10^{-6}$	$\left(99900.0^{76000.0}_{0.41}\right) \times 10^{-6}$
OT 081	57592..57596	2.0	76	$1.689^{0.017}_{0.014}$	$0.03^{0.011}_{0.013}$	$\left(0.015^{0.0038}_{0.0035}\right) \times 10^{-6}$	$\left(99.91^{32.0}_{0.0062}\right) \times 10^{-3}$
OT 081	57575..57578	0.7	4	$1.74^{1.4}_{0.58}$	$\left(150000.0^{0.073}_{140000.0}\right) \times 10^{-6}$	$\left(0.082^{26.0}_{0.079}\right) \times 10^{-6}$	-
OT 081	57590..57592	2.0	15	$1.15^{0.26}_{0.075}$	$\left(150.0^{0.0024}_{43.0}\right) \times 10^{-3}$	$\left(0.013^{0.018}_{0.0049}\right) \times 10^{-6}$	-
OT 081	57578..57584	0.7	52	$1.705^{0.015}_{0.012}$	$0.049^{0.015}_{0.019}$	$\left(0.027^{0.0083}_{0.0075}\right) \times 10^{-6}$	$0.1063^{0.063}_{0.0064}$
OT 081	57584..57588	0.9	40	$1.6413^{0.012}_{0.0099}$	$0.061^{0.014}_{0.015}$	$\left(0.065^{0.018}_{0.015}\right) \times 10^{-6}$	$0.1054^{0.061}_{0.0055}$
B2 1846+32A	55473..55481	0.4	7	$1.1^{1.3}_{0.5}$	$\left(150.0^{0.0029}_{140.0}\right) \times 10^{-3}$	$\left(0.47^{8.0}_{0.39}\right) \times 10^{-9}$	-
B2 1846+32A	55492..55497	0.9	46	$1.589^{0.011}_{0.01}$	$0.08^{0.013}_{0.012}$	$\left(0.037^{0.0094}_{0.0066}\right) \times 10^{-6}$	$\left(92.01^{23.0}_{0.0069}\right) \times 10^{-3}$
B2 1846+32A	55486..55492	0.9	28	$1.609^{0.012}_{0.012}$	$0.066^{0.013}_{0.013}$	$\left(0.026^{0.0069}_{0.0055}\right) \times 10^{-6}$	$\left(92000.0^{60000.0}_{0.91}\right) \times 10^{-6}$
B2 1846+32A	55497..55502	0.5	5	$0.79^{1.2}_{0.29}$	$0.1485^{0.0015}_{0.14}$	$\left(0.17^{22.0}_{0.16}\right) \times 10^{-9}$	-
B2 1846+32A	55481..55486	0.8	9	$1.87^{0.48}_{1.2}$	$0.017^{0.13}_{0.012}$	$\left(0.011^{0.16}_{0.011}\right) \times 10^{-6}$	-
B2 1846+32B	57340..57345	2.0	8	$1.02^{1.0}_{0.28}$	$\left(150.0^{0.005}_{140.0}\right) \times 10^{-3}$	$\left(0.91^{43.0}_{0.77}\right) \times 10^{-9}$	-
B2 1846+32B	57345..57346	1.0	12	$2.07^{0.27}_{1.0}$	$\left(5.0^{140.0}_{0.0026}\right) \times 10^{-3}$	$\left(0.2^{0.74}_{0.2}\right) \times 10^{-6}$	-
B2 1846+32B	57346..57353	0.6	18	$1.789^{0.055}_{0.033}$	$0.08^{0.044}_{0.037}$	$\left(0.012^{0.012}_{0.0059}\right) \times 10^{-6}$	$\left(156.0^{0.01}_{78.0}\right) \times 10^{-3}$
S4 1849+67	55749..55754	0.5	4	$0.78^{1.2}_{0.28}$	$\left(150000.0^{0.04}_{140000.0}\right) \times 10^{-6}$	$\left(0.074^{9.4}_{0.069}\right) \times 10^{-9}$	-
S4 1849+67	55748..55748	2.0	8	$0.76^{1.2}_{0.26}$	$\left(150.0^{0.0019}_{140.0}\right) \times 10^{-3}$	$\left(0.41^{47.0}_{0.37}\right) \times 10^{-9}$	-
S4 1849+67	55745..55748	2.0	11	$1.774^{0.11}_{0.046}$	$\left(5000.0^{47000.0}_{0.0085}\right) \times 10^{-6}$	$\left(0.0022^{0.0021}_{0.0011}\right) \times 10^{-6}$	$\left(48.65^{49.0}_{0.047}\right) \times 10^{-3}$
S4 1849+67	55741..55745	0.3	8	$2.68^{0.88}_{1.4}$	$\left(5.1^{140.0}_{0.09}\right) \times 10^{-3}$	$\left(0.77^{68.0}_{0.77}\right) \times 10^{-6}$	-
S4 1849+67	55748..55749	0.9	15	$1.71^{0.18}_{0.99}$	$\left(5.61^{140.0}_{0.61}\right) \times 10^{-3}$	$\left(0.044^{0.087}_{0.043}\right) \times 10^{-6}$	-
PKS 2149-306	56300..56306	4.0	9	$1.704^{0.19}_{0.076}$	$\left(150000.0^{0.19}_{32000.0}\right) \times 10^{-6}$	$\left(0.21^{0.18}_{0.074}\right) \times 10^{-6}$	-
PKS 2149-306	56291..56300	0.7	9	$1.8^{0.84}_{0.17}$	$\left(150.0^{0.0038}_{140.0}\right) \times 10^{-3}$	$\left(0.09^{1.2}_{0.056}\right) \times 10^{-6}$	-
PKS 2149-306	56312..56313	0.6	10	$1.56^{0.92}_{0.19}$	$\left(150000.0^{0.92}_{140000.0}\right) \times 10^{-6}$	$\left(0.18^{3.9}_{0.12}\right) \times 10^{-6}$	-

Source	MJD range	red. χ^2	DOF	α	β	N	n_H
PKS 2149-306	56313..56318	1.0	8	$1.45^{0.93}_{0.21}$	$\left(150.0^{0.0045}_{140.0}\right) \times 10^{-3}$	$\left(0.021^{0.51}_{0.016}\right) \times 10^{-6}$	-
PKS 2149-306	56306..56312	1.0	8	$1.82^{0.89}_{0.2}$	$\left(149.99^{0.0052}_{140.0}\right) \times 10^{-3}$	$\left(0.13^{2.3}_{0.09}\right) \times 10^{-6}$	-
PKS 2149-306	56289..56291	0.6	1	$2.8^{\dagger}$	$0.112^{0.39}_{0.053}$	$\left(0.0033^{0.29}_{0.0031}\right) \times 10^{-3}$	-
PKS 2155-83	55202..55206	1.0	7	$2.2^{0.83}_{0.84}$	$0.068^{0.082}_{0.063}$	$\left(0.21^{7.4}_{0.2}\right) \times 10^{-6}$	-
PKS 2155-83	55206..55211	0.6	9	$1.87^{0.44}_{1.3}$	$\left(5.0^{140.0}_{0.0028}\right) \times 10^{-3}$	$\left(0.0076^{0.097}_{0.0076}\right) \times 10^{-6}$	-
PKS 2155-83	55198..55200	0.001	-1	$3.0^{1.0}_{2.5}$	$\left(5.0^{140.0}_{0.0034}\right) \times 10^{-3}$	$\left(0.001^{1.6}_{0.001}\right) \times 10^{-3}$	-
PKS 2155-83	55200..55202	0.9	9	$\left(500.0^{1600.0}_{0.0012}\right) \times 10^{-3}$	$0.28^{0.04}_{0.27}$	$\left(0.85^{110.0}_{0.41}\right) \times 10^{-9}$	-
NRAO 676	56091..56097	0.5	12	$1.7^{0.66}_{0.11}$	$\left(150000.0^{0.013}_{120000.0}\right) \times 10^{-6}$	$\left(0.22^{1.5}_{0.11}\right) \times 10^{-6}$	-
NRAO 676	56097..56102	1.0	7	$1.7^{1.1}_{0.3}$	$\left(150000.0^{0.54}_{140000.0}\right) \times 10^{-6}$	$\left(0.088^{4.4}_{0.074}\right) \times 10^{-6}$	-
NRAO 676	56102..56104	0.1	1	$2.6^{\dagger}$	$0.14^{\dagger}$	$\left(0.0027^{0.0023}_{0.0023}\right) \times 10^{-3}$	-
NRAO 676	56104..56105	0.8	8	$1.86^{0.97}_{0.25}$	$\left(150000.0^{0.18}_{140000.0}\right) \times 10^{-6}$	$\left(0.66^{19.0}_{0.51}\right) \times 10^{-6}$	-
NRAO 676	56105..56107	1.0	14	$1.714^{0.055}_{0.034}$	$0.093^{0.047}_{0.074}$	$\left(27000.0^{2.7e-05}_{9000.0}\right) \times 10^{-12}$	$\left(389.01^{350.0}_{0.015}\right) \times 10^{-3}$
NRAO 676	56107..56109	0.2	8	$1.5^{1.0}_{0.3}$	$\left(149.75^{0.25}_{140.0}\right) \times 10^{-3}$	$\left(0.051^{2.4}_{0.043}\right) \times 10^{-6}$	-
NRAO 676	56086..56091	0.4	8	$2.4^{0.5}_{1.2}$	$\left(5.0^{140.0}_{0.0019}\right) \times 10^{-3}$	$\left(0.31^{4.6}_{0.3}\right) \times 10^{-6}$	-
NRAO 676	56080..56086	1.0	2	$1.93^{1.9}_{0.89}$	$\left(150.0^{0.0022}_{140.0}\right) \times 10^{-3}$	$\left(0.083^{220.0}_{0.083}\right) \times 10^{-6}$	-
PKS 2233-148	56099..56100	1.0	10	$0.97^{0.95}_{0.19}$	$\left(150.0^{0.0018}_{140.0}\right) \times 10^{-3}$	$\left(0.0033^{0.09}_{0.0024}\right) \times 10^{-6}$	-
PKS 2233-148	56094..56096	3.0	7	$1.8^{0.36}_{1.1}$	$\left(5.0^{140.0}_{0.0035}\right) \times 10^{-3}$	$\left(0.015^{0.14}_{0.014}\right) \times 10^{-6}$	-
PKS 2233-148	56092..56094	0.5	12	$1.25^{0.92}_{0.15}$	$\left(150000.0^{0.058}_{140000.0}\right) \times 10^{-6}$	$\left(0.013^{0.3}_{0.0079}\right) \times 10^{-6}$	-
PKS 2233-148	56089..56092	1.0	27	$1.633^{0.012}_{0.012}$	$0.081^{0.014}_{0.013}$	$\left(0.07^{0.019}_{0.015}\right) \times 10^{-6}$	$\left(32.5^{22.0}_{0.0045}\right) \times 10^{-3}$
PKS 2233-148	56100..56105	0.7	8	$1.754^{0.068}_{0.039}$	$\left(5.0^{62.0}_{0.0037}\right) \times 10^{-3}$	$\left(2.6^{4.3}_{0.89}\right) \times 10^{-9}$	$\left(32.62^{32.0}_{0.12}\right) \times 10^{-3}$
PKS 2233-148	56096..56098	0.9	13	$1.08^{0.46}_{0.11}$	$\left(150000.0^{0.089}_{76000.0}\right) \times 10^{-6}$	$\left(0.0071^{0.027}_{0.0037}\right) \times 10^{-6}$	-
PKS 2233-148	56098..56099	1.0	12	$1.93^{0.15}_{0.9}$	$\left(5.0^{140.0}_{0.0023}\right) \times 10^{-3}$	$\left(0.25^{0.35}_{0.24}\right) \times 10^{-6}$	-
PKS 2233-148	56082..56089	1.0	31	$1.6623^{0.01}_{0.0099}$	$0.061^{0.013}_{0.012}$	$\left(0.03^{0.0074}_{0.006}\right) \times 10^{-6}$	$\left(32500.0^{32000.0}_{0.71}\right) \times 10^{-6}$
PKS 2233-148	56076..56082	2.0	12	$1.17^{0.75}_{0.14}$	$\left(150000.0^{0.11}_{130000.0}\right) \times 10^{-6}$	$\left(0.0026^{0.025}_{0.0016}\right) \times 10^{-6}$	-

TABLE C.2: For each Bayesian block, the following parameters are given: Source name, block time range (MJD), reduced χ^2, degrees of freedom (DOF), log-parabola index α, curvature β, normalization N and n_H column density where XRT data sets were used. Values denoted with † have been fixed to their respective 4FGL catalog value.

Source Name	*Swift*-XRT ObsIDs
B2 0218+357	00032533002, 00032551001, 00032551002, 00032533001, 00032551003, 00032551004
B2 0552+39A	00036315010, 00036315009, 00036315011
TXS 0646-176	00011005004, 00011005003
4C +14.23	00039140002, 00039140003
PKS 0903-57	00033856008, 00033856007, 00033856006
S4 0954+65	00033530002, 00033530001
PKS B1150-108	00010991002, 00010986001[†], 00010987001[†], 00010988001, 00010985001, 00010984004[†]
4C +49.22	00031975002, 00031975001
GB 1310+487	00031547001, 00031547002
PKS 1454-354	00036799003
OT 081	00036392033, 00036392032, 00036392035, 00036392027, 00036392034, 00036392031, 00036392030, 00036392029, 00036392028
B2 1846+32A	00038420002, 00038420004, 00038420003, 00038420005, 00038420006
B2 1846+32B	00046547004
S4 1849+67	00036218010
NRAO 676	00032510001
PKS 2233-148	00032488001, 00032488002, 00039210007

TABLE C.1: *Swift*-XRT Observation IDs (ObsIDs) for all sources that have simultaneous XRT observations. Observations with [†] were not used due to the short (< 1 ks) exposures.

Bibliography

Abbott, B. P. et al. (2016). In: Phys. Rev. Lett. 116 (6), p. 061102.

Abdo, A. A. et al. (May 2009). In: ApJ 697.1, pp. 934–941.

Abdo, A. A. et al. (2010). In: ApJS 188.2, pp. 405–436.

Abdo, A. A. et al. (Oct. 2010a). In: ApJ 722.1, pp. 520–542.

Abdo, A. A. et al. (June 2010b). In: ApJ 716.1, pp. 30–70.

Abdollahi, S. et al. (Mar. 2020). In: ApJS 247.1, 33, p. 33.

Akujor, Chidi E. and Simon T. Garrington (June 1991). In: MNRAS 250, p. 644.

Angioni, R. (June 2018). In: *The Astronomer's Telegram* 11706, p. 1.

Antonucci, Robert (1993). In: ARA&A 31, pp. 473–521.

Arsioli, B. and Y. L. Chang (Feb. 2017). In: A&A 598, A134, A134.

Atwood, W. B. et al. (June 2009). In: ApJ 697.2, pp. 1071–1102.

Bachev, R. (July 2015). In: MNRAS 451, pp. L21–L24.

Ballet, J. (Mar. 1, 1999). In: A&AS 135, pp. 371–381.

Barnacka, Anna et al. (2016). In: ApJ 821.1, p. 58.

Barthelmy, Scott D. et al. (Oct. 2005). In: Space Sci. Rev. 120.3-4, pp. 143–164.

Baumgartner, W. H. et al. (Aug. 2013). In: ApJS 207.2, 19, p. 19.

Bianchin, V. et al. (Mar. 2009). In: A&A 496.2, pp. 423–428.

Biggs, A. D. et al. (Apr. 1999). In: MNRAS 304.2, pp. 349–358.

Buson, Sara (Apr. 2020). In: *The Astronomer's Telegram* 13604, p. 1.

Carilli, C. L. et al. (Jan. 1997). In: ApJ 474.2, pp. L89–L93.

Carrasco, L. et al. (Nov. 2015). In: *The Astronomer's Telegram* 8330, p. 1.

Cheung, C. C. et al. (Feb. 2014). In: ApJ 782.2, L14, p. L14.

Ciprini, S. (May 2009). In: *The Astronomer's Telegram* 2049, p. 1.

Ciprini, Stefano (July 2015). In: *The Astronomer's Telegram* 7833, p. 1.

Ciprini, Stefano (Nov. 2018). In: *The Astronomer's Telegram* 12252, p. 1.

Cutini, S. et al. (Dec. 2014). In: MNRAS 445.4, pp. 4316–4334.

Cutini, Sara (Oct. 2012). In: *The Astronomer's Telegram* 4486, p. 1.

Cutini, Sara (Nov. 2019). In: *The Astronomer's Telegram* 13254, p. 1.

D'Ammando, F. and M. Orienti (Jan. 2016). In: MNRAS 455.2, pp. 1881–1891.

de Rosa, A. et al. (July 2008). In: MNRAS 388.1, pp. L54–L58.

Deng, Can-Min et al. (Mar. 2016). In: ApJ 820.1, 66, p. 66.

Donato, D. et al. (Sept. 1, 2001). In: A&A 375.3, pp. 739–751.

Falcke, Heino et al. (Oct. 2000). In: ApJ 542.1, pp. 197–200.

Fan, Xiaohui (Nov. 2006). English (US). In: New A Rev. 50.9-10, pp. 665–671.

Fan, Xu-Liang and Qingwen Wu (Dec. 2018). In: ApJ 869.2, 133, p. 133.

Fanaroff, B. L. and J. M. Riley (May 1974). In: MNRAS 167, 31P–36P.

Fossati, G. et al. (Sept. 1998). In: MNRAS 299.2, pp. 433–448.

Gabuzda, D. C. et al. (June 2000). In: MNRAS 315.2, pp. 229–240.

Gehrels, N. et al. (Aug. 2004). In: ApJ 611.2, pp. 1005–1020.

Ghirlanda, G. et al. (Sept. 2010). In: MNRAS 407.2, pp. 791–803.

Ghirlanda, G. et al. (May 2011). In: MNRAS 413.2, pp. 852–862.

Ghisellini, G. et al. (July 2017). In: MNRAS 469.1, pp. 255–266.

Ghisellini, Gabriele (2013). Vol. 873.

Giommi, P. et al. (Mar. 2012). In: MNRAS 420.4, pp. 2899–2911.

Hartman, R. C. et al. (July 1999). In: ApJS 123.1, pp. 79–202.

Houck, J. C. and L. A. Denicola (2000). In: *Astronomical Data Analysis Software and Systems IX*. Ed. by Nadine Manset, Christian Veillet, and Dennis Crabtree. Vol. 216. Astronomical Society of the Pacific Conference Series, p. 591.

IceCube Collaboration et al. (July 2018). In: *Science* 361.6398, eaat1378, eaat1378.

Kalberla, P. M. W. et al. (Sept. 2005). In: A&A 440.2, pp. 775–782.

Kanekar, Nissim and Jayaram N. Chengalur (Feb. 2008). In: MNRAS 384.1, pp. L6–L10.

Kang, Shi-Ju (Mar. 2017). In: ApJ 837.1, 38, p. 38.

Kapanadze, B. et al. (Oct. 2018a). In: MNRAS 480.1, pp. 407–430.

Kapanadze, B. et al. (Oct. 2018b). In: MNRAS 480.1, pp. 407–430.

Kellermann, K. I. et al. (Oct. 1989). In: AJ 98, p. 1195.

Khachikian, E. Y. and D. W. Weedman (Sept. 1974). In: ApJ 192, pp. 581–589.

Kida, S. et al. (May 2010). In: ApJ 714.1, pp. L36–L40.

Kim, Dae-Won et al. (Oct. 2018). In: MNRAS 480.2, pp. 2324–2333.

Komossa, S. (Sept. 2015). In: *Journal of High Energy Astrophysics* 7, pp. 148–157.

Lobanov, Andrei (Oct. 2010). In: *arXiv e-prints*, arXiv:1010.2856, arXiv:1010.2856.

Marscher, Alan P. et al. (Nov. 2018). In: ApJ 867.2, 128, p. 128.

Massaro, E. et al. (Feb. 2009). In: A&A 495.2, pp. 691–696.

Mattox, J. R. et al. (Apr. 1996). In: ApJ 461, p. 396.

McGlynn, Thomas A. et al. (May 1997). In: ApJ 481.2, pp. 625–632.

Miller, M. Coleman and Nicolás Yunes (Apr. 2019). In: Nature 568.7753, pp. 469–476.

Moraitis, Christina D. and D. J. Thompson (Jan. 2019). In: *arXiv e-prints*, arXiv:1901.09810, arXiv:1901.09810.

Morozova, D. A. et al. (Sept. 2014). In: AJ 148.3, 42, p. 42.

Mukherjee, R. et al. (May 1995). In: ApJ 445, p. 189.

Nalewajko, Krzysztof (Jan. 2013). In: MNRAS 430.2, pp. 1324–1333.

Omodei, Nicola et al. (Sept. 2018). In: ApJ 865.1, L7, p. L7.

Paliya, Vaidehi S. et al. (Feb. 2019). In: ApJ 871.2, 211, p. 211.

Planck Collaboration et al. (Sept. 2020). In: A&A 641, A6, A6.

Preston, R. A. et al. (Sept. 1985). In: AJ 90, pp. 1599–1603.

Pushkarev, A. B., Y. Y. Kovalev, and M. L. Lister (Oct. 2010). In: ApJ 722.1, pp. L7–L11.

Pushkarev, A. B. et al. (Jan. 2019). In: MNRAS 482.2, pp. 2336–2353.

Rani, Priyanka and C. S. Stalin (Apr. 2018). In: ApJ 856.2, 120, p. 120.

Remillard, Ronald A. and Jeffrey E. McClintock (2006). In: ARA&A 44.1, pp. 49–92.

Richards, J. L. et al. (Mar. 2014). In: MNRAS 438.4, pp. 3058–3069.

Romano, P. et al. (Sept. 2006). In: A&A 456.3, pp. 917–927.

Roming, Peter W. A. et al. (Oct. 1, 2005). In: Space Sci. Rev. 120, pp. 95–142.

Rowan-Robinson, M. (May 1, 1977). In: ApJ 213, pp. 635–647.

Sahakyan, N., D. Zargaryan, and V. Baghmanyan (Feb. 2015). In: A&A 574, A88, A88.

Scargle, Jeffrey D. et al. (Feb. 2013). In: ApJ 764.2, 167, p. 167.

Seyfert, Carl K. (Jan. 1, 1943). In: ApJ 97, p. 28.

Sinapius, J. and R. Ojha (Feb. 2020). In: *The Astronomer's Telegram* 13533, p. 1.

Sitarek, J. and W. Bednarek (June 2016). In: MNRAS 459.2, pp. 1959–1967.

Sokolovsky, K. V. et al. (Apr. 2010). In: *The Astronomer's Telegram* 2589, p. 1.

Sokolovsky, K. V. et al. (May 2014). In: A&A 565, A26, A26.

Tagliaferri, G. et al. (July 2015). In: ApJ 807.2, 167, p. 167.

Tanaka, Yasuyuki T., Sara Buson, and Daniel Kocevski (Sept. 2017). In: *The Astronomer's Telegram* 10791, p. 1.

The Fermi-LAT collaboration (May 2019). In: *arXiv e-prints*, arXiv:1905.10771, arXiv:1905.10771.

In: Space Sci. Rev. 120.3 (), pp. 165–195.

Thompson, David (Nov. 2018). In: *Galaxies* 6.4, p. 117.

Tombesi, F. et al. (Mar. 2017). In: ApJ 838.1, 16, p. 16.

Uemura, Makoto et al. (Dec. 2017). In: PASJ 69.6, 96, p. 96.

Ulvestad, James S. and Luis C. Ho (Dec. 2001). In: ApJ 562.2, pp. L133–L136.

Ulvestad, James S. et al. (Sept. 2005). In: AJ 130.3, pp. 936–944.

Urry, C. Megan and Paolo Padovani (Sept. 1995). In: PASP 107, p. 803.

Verner, D. A. et al. (July 1, 1996). In: ApJ 465, p. 487.

Véron-Cetty, M. P. and P. Véron (Sept. 2001). In: A&A 375, pp. 791–796.

Véron-Cetty, M. P. and P. Véron (Aug. 2006). In: A&A 455.2, pp. 773–777.

Vestergaard, Marianne and Bradley M. Peterson (2006). In: ApJ 641.2, p. 689.

Wagner, S. J. et al. (Apr. 1993). In: A&A 271, pp. 344–347.

Wang, Gege et al. (Feb. 2020). In: PASJ 72.1, 9, p. 9.

Wilms, J., A. Allen, and R. McCray (Oct. 2000). In: ApJ 542, pp. 914–924.

Wood, M. et al. (Jan. 2017). In: *35th International Cosmic Ray Conference (ICRC2017)*. Vol. 301. International Cosmic Ray Conference, p. 824.

Yang, Jianping and Bing Zhou (Apr. 2016). In: PASP 128.962, p. 044101.

Yurchenko, A. V., S. G. Marchenko-Jorstad, and A. P. Marscher (June 2000). In: A&A 358, pp. 428–432.

Zhang, Jin et al. (Oct. 2018). In: ApJ 865.2, 100, p. 100.

Zhang, Li, Jui-Hui Fan, and Kwong-Sang Cheng (Apr. 2002). In: PASJ 54.2, pp. 159–169.